Dissertation

submitted to the
Combined Faculties of the Natural Sciences and Mathematics
of the Ruperto-Carola-University of Heidelberg, Germany,
for the degree of
Doctor of Natural Sciences

Put forward by

Ilya Sergeevich Khrykin
born in: Rostov-on-Don, Russian Federation

Oral examination: 20 April, 2016

Understanding The Sources of He II Reionization

Ilya Sergeevich Khrykin

Max Planck Institute für Astronomie

Scientific advisor: Dr. Joseph F. Hennawi

Referees: Dr. Joseph F. Hennawi
Prof. Dr. Volker Springel

"The only way of discovering the limits of the possible is to venture a little way past them into the impossible."
- Arthur Clarke's Second Law

To my parents, my sister,
and my wife Alina

ABSTRACT

The lifetime of quasars is a fundamental parameter for understanding the physical processes governing the growth of supermassive black holes, their co-evolution with galaxies, and the reionization history of the intergalactic helium. However, despite cosmological importance, current estimates of quasar lifetime are uncertain by at least two orders of magnitude, preventing significant progress in our understanding of the above questions. This thesis presents theoretical progress toward constraining quasar lifetimes and properties of helium reionization. A combination of cosmological hydrodynamical simulations and 1D radiative transfer algorithm is used to investigate the structure and evolution of the He II Lyα proximity zones around quasars at redshift $z \simeq 3-4$ and draw the following conclusions.

In the first part of this thesis I show that the time evolution of the proximity zones can be described by a simple analytical model for the approach of the fraction of singly ionized helium (He II fraction) to ionization equilibrium, and use this picture to illustrate how the transmission profile depends on the quasar lifetime, quasar luminosity, and the the average He II fraction (or equivalently the metagalactic He II ionizing background). Due to density fluctuations I advocate stacking existing He II quasar spectra at $z \sim 3$, and show that the shape of this average proximity zone profile is sensitive to lifetimes as long as ~ 30 Myr. I find that at higher redshift $z \sim 4$ where the He II fraction is poorly constrained, degeneracies will make it challenging to determine these parameters independently.

In the second part of this thesis I describe the method to constrain the quasar lifetime and the He II fraction (redshifts of the He II reionization) at $z \gtrsim 4$ using the thermal state of the intergalactic medium around quasars. I show how the temperature of intergalactic gas increases due to quasar activity, producing thermal proximity effect in the Lyα absorption spectra. I investigate how the amplitude and the extent of thermal proximity effect depend on the amount of singly ionized helium in the IGM prior to quasar activity and on quasar lifetime by measuring the power spectrum of the H I Lyα absorption spectra. I propose to use Markov Chain Monte Carlo algorithm to estimate the accuracy of the power spectrum measurement, and illustrate how with the mock sample of 50 high-resolution quasar spectra the He II fraction and quasar lifetime can be estimated with $\simeq 5-10\%$ and $0.03-0.1$ dex precision, respectively.

Finally, I briefly discuss the outlook for the future progress in this area of research.

ZUSAMMENFASSUNG

Die Kenntnis von der Lebensdauer von Quasaren ist unerlässlich für das Verständnis der physikalischen Vorgänge beim Wachsen supermassereicher schwarzer Löcher, deren gemeinsamer Entwicklung mit ihren Heimatgalaxien sowie dem Verlauf der Reionisierung des intergalaktischen Heliums. Jedoch schwanken Schätzungen ihres numerischen Werts um mindestens zwei Größenordnungen was nennenswerte Fortschritte in der Beantwortung der obigen Fragen erschwert. Die vorliegende Arbeit behandelt theoretische Methoden, die zu einer genaueren Bestimmung der Quasarlebensdauern und damit zu einem besseren Verständnis der Heliumionisierung führen sollen. Mithilfe kosmologischer hydrodynamischer Simulationen in Verbindung mit einem eindimensionalen Strahlungstransportalgorithmus wurden Struktur und Entwicklung der Regionen um Quasare mit Rotverschiebungen $z \approx 3-4$, in denen Helium vollständig ionisiert vorliegt, untersucht.

Im ersten Teil der Arbeit präsentiere ich ein einfaches analytisches Modell, mit dem die zeitliche Entwicklung dieser ionisierenten Quasarumgebungen beschrieben werden kann. Es beschreibt, wie der relative Anteil einfach ionisierten Heliums (He II Anteil) ins Ionisationsgleichgewicht kommt. Anhand dieses Modells kann ermittelt werden, wie das Transmissionsprofil von der Lebensdauer und der Leuchtkraft von Quasaren sowie vom He II Anteil abhängt. Aufgrund von Dichteschwankungen müssen mehrere He II Quasarspektren mit $z \approx 3$ addiert werden. Mit dieser Methode können nur Quasarlebensdauern bestimmt werden, sofern diese nicht über ≈ 30 Myr liegen. Bei höheren Rotverschiegungen ($z \approx 4$) ist der He II Anteil schwer einzugrenzen und damit die Bestimmung der einzelnen Parameter sehr schwer.

Im zweiten Teil der Arbeit stelle ich eine Methode vor, mit der die Lebensdauer von Quasaren und der He II Anteil (beziehungsweise die Rotverschiebung bei der He II reionisiert wird) bei ($z \gtrsim 4$) anhand der thermischen Eigenschaften des intergalaktischen Mediums, das die Quasare umgibt, bestimmt werden kann. Ich beschreibe, wie die Temperatur dieses Gases durch die Quasaraktivität steigt und wie sich dadurch die Lyα Absorptionsspektra verändern. Ich untersuche, wie die Amplitude und der Einflussbereich dieses Effekts von der Quasarlebensdauer und vom He II Vorkommen vor Einsetzen der Quasaraktivität abhängt. Dazu wird das Leistungsspektrum der H I Lyα Absorptionsspektra gemessen. Um die Genauigkeit dieser Messung zu bestimmen, wird ein Monte Carlo Markov Chain Algorithmus vorgeschlagen. Ich zeige, wie mithilfe von 50 hochaufgelösten künstlichen Quasaspektren, der He II Anteil auf $\approx 5-10\%$ und die Quasarlebensdauer auf $0.03-0.1$ dex genau bestimmt werden können.

Abschließend gebe ich einen Ausblick zukünftige Fortschritte in diesem Forschungsgebiet.

CONTENTS

1 Introduction **1**

1.1 The beginning of the Universe. Formation of structure and galaxies . 2

1.2 Quasars. Galaxy evolution continues 5

1.3 Intergalactic medium. Reionization of hydrogen and helium 7

1.4 The lifetime of quasars 11

1.5 Outlook of the Thesis 15

2 Numerical model **17**

2.1 Hydrodynamical simulations 17

2.2 1D radiative transfer algorithm 18

2.2.1 Model of the ionizing sources 18

2.2.2 The evolution of He II fraction 20

2.2.3 Implementation of Heating and Cooling 22

2.2.4 Finite Speed of Light 23

2.2.5 Recombinations 23

2.2.6 An example radiative transfer output 24

3 A new way of thinking about the proximity zones 27

3.1 Observational constraints on the He IIionizing background $\Gamma_{\rm HeII}^{\rm bkg}$ . . . 28

3.2 Time-evolution of the He II fraction 30

3.3 Degeneracy between the He II background and the lifetime of quasars 34

3.4 Summary 37

4 Properties of the stacked transmission profiles 39

4.1 The dependence on quasar lifetime 42

4.2 The dependence on He II ionizing background 46

4.3 The dependence on quasar photon production rate 47

4.4 Distribution of quasar lifetimes and He II backgrounds 48

4.5 Prospects at $z \simeq 4$ 52

4.5.1 Stacked transmission profiles at $z \simeq 4$ 52

4.5.2 Distribution of the Proximity Zone Sizes 54

4.6 Summary 56

5 Thermal Proximity Effect 57

5.1 Temperature evolution 59

5.2 Line-of-sight power spectrum statistics 64

5.2.1 Sensitivity to quasar lifetime 66

5.2.2 Sensitivity to initial He II fraction 68

5.3 MCMC analysis: likelihood estimation 70

5.4 MCMC analysis: results 71

5.5 MCMC analysis: accuracy 75

5.6 Summary 76

6 Conclusions and Future Work **77**

6.1 Main results of the thesis 78

6.2 Outlook 79

6.2.1 Comparison to HST/COS data 80

6.2.2 Constraints on quasar lifetime from H I proximity zones at $z \sim 6$ 81

6.2.3 Thermal proximity effect 81

A Light Travel Effects **83**

B The Impact of Lyman-Limit Systems **85**

C He II ionizing radiation from recombinations **91**

D Generating He II Lyα absorption spectra **95**

LIST OF FIGURES **97**

Acronyms **99**

BIBLIOGRAPHY **101**

Acknowledgements **109**

CHAPTER 1

INTRODUCTION

"In the beginning the Universe was created.
This has made a lot of people very angry
and been widely regarded as a bad move."
Douglas Adams
(The Restaurant at the End of the Universe)

Recent advances in observational astronomy have led to the discovery of supermassive black holes in the centers of all massive, bulge-dominated galaxies. These dormant giants are believed to be the relics of a once active phase in the evolution of galaxies, which is often referred to as the *quasar phase*. During this epoch, the super-massive black holes simultaneously increased their mass through accretion of gas and dust, emitting tremendous amounts of energy across the electromagnetic spectrum. Galaxies in this phase are referred to as quasars - the most luminous, powerful and energetic phenomenon known to exist.

The goal of this theoretical work is to develop a method to constrain the quasar lifetime - the timescale of the individual episodes of accretion on to the super-massive black hole. We shall use deductive reasoning to understand the importance of this timescale in a broad cosmological context. The first part of this introduction presents an overview of the history of the Universe, focusing on the formation of structure and galaxies. Then, we shall explain the importance of quasars in a cosmological framework, their role in the evolution of galaxies and the intergalactic medium (IGM). Further, we discuss the current observational and theoretical methods for constraining the quasar lifetime, as well as their respective strengths and limitations. We conclude with a brief outline of the thesis chapters that follow.

1.1 THE BEGINNING OF THE UNIVERSE. FORMATION OF STRUCTURE AND GALAXIES

One of the most important problems of modern cosmology is to understand how the observed population of galaxies and galaxy clusters formed from the initial conditions of the very hot, dense and nearly homogeneous primordial plasma. Today, the standard cosmological theory that best describes the Big Bang and subsequent formation of structure, supported by direct observations, is the ΛCDM[1] model. We shall describe the most salient aspects of this model in what follows.

According to the ΛCDM paradigm the history of the Universe began ∼ 13.8 Gyr ago with the event known as the *Big Bang*, when the fabric of space-time itself emerged from the initial phase of singularity[2]. In fractions of a second after the Big Bang ($\sim 10^{-35}$s), *cosmic inflation* (Guth 1981; Linde 1982; Albrecht & Steinhardt 1982), driven by the cosmological constant Λ (Lahav et al. 1991), caused the Universe to grow exponentially in size. This process is believed to be responsible not only for solving the main problems of the classical hot Big Bang model[3] (a dominant cosmological theory before ΛCDM), but it also introduced the initial irregularities into the Universe, which led later to the formation of structure. According to Heisenberg's uncertainty principle (Heisenberg 1927), each point in space experiences so-called *quantum fluctuations*, fluctuations in the amount of energy caused by virtual particles being continually born and destroyed. These fluctuations were "frozen" into the rapidly expanding space-time and consequently stretched to macroscopic scales, producing near scale invariant, Gaussian perturbations in the cosmic energy density (Starobinsky 1982). Under the gravitational force these fluctuations became the sights of structure formation at later epochs.

Shortly after cosmic inflation finished and the temperature of the Universe decreased adiabatically, baryons were formed from the primordial, nearly homogeneous quark-gluon plasma. However, the temperature of the Universe was still very high and the baryonic particles, moving at relativistic velocities, were coupled to the photons in

[1] ΛCDM stands for Λ-Cold-Dark-Matter, the model in which the Universe consists of dark energy, described by the cosmological constant Λ, cold dark matter and normal baryonic matter. According to the most recent measurements the mass-energy composition of the Universe consists of only ∼ 5% baryonic matter, while dark matter and dark energy contribute ∼ 26% and ∼ 69%, respectively (Planck Collaboration et al. 2015).

[2] The very nature of this singularity postulates that all laws of physics known to humankind will break down. It might be hard to imagine, but as Lev Landau once said: "Perhaps the greatest triumph of human genius is that people can understand things that they can no longer imagine".

[3] These problems include: the flatness problem, the horizon problem, baryon asymmetry and magnetic monopoles. However, we shall not discuss them in detail in the framework of this thesis.

one hot thermally equilibrated photon-baryon plasma.

Thereafter, the Universe continued expanding and cooling down. At the age of approximately 380,000 yr (or redshift[4] $z \sim 1100$) the temperature of the Universe dropped to $\sim$ 3000 K. At this time the Universe experienced the next phase transition, which was misnamed as the *Recombination Era*, when radiation decoupled from baryonic particles. Baryons combined and formed neutral atoms (mostly hydrogen and helium) and radiation, which after experiencing the last scattering, propagated freely into the cosmos. With time this redshifted radiation has cooled down, and can now be observed as the *Cosmic Microwave Background* or, simply, CMB (Alpher & Herman 1949; Gamow 1952; Dicke et al. 1965; Penzias & Wilson 1965; Planck Collaboration et al. 2015).The detailed studies of this radiation with space-based experiments COBE (Boggess et al. 1992), RELIKT-1 (Strukov et al. 1992), WMAP (Bennett et al. 2003) and Planck (Tauber et al. 2010) have detected small $\Delta T/T \sim 10^{-5}$ primary anisotropies[5] in the temperature of the CMB (Bennett et al. 1996). These results indicate that the CMB is very close to isotropic, reflecting the conditions in the very early Universe where anisotropies were induced by the primordial fluctuations during cosmic inflation. However, observations of the nearby Universe have shown us the wealth of various structure, therefore suggesting the evolution of the initial energy density perturbations that grew during cosmic inflation.

The force of gravity provides a necessary mechanism to describe how these structures evolved with time. However, gravitational forces must exceed the gas pressure in order to collapse the normal baryonic matter. Jeans (1902) illustrated that the gravitational collapse of baryonic gas occurs only on the scales greater than the so-called *Jeans scale* $\lambda_{\rm J} = \sqrt{\pi c_{\rm s}^2/G\rho}$, where $c_{\rm s}$ is the speed of sound in the gas with density ρ, and G is the gravitational constant. Lifshitz (1946) showed that under this assumption the time needed to grow structure as complex as a galaxy in the expanding Friedmann Universe is more then the Hubble time[6]. In addition, with the discovery and intensive

[4]The light emitted at some location in space experiences cosmological redshifting, or an increase in the wavelength of radiation, while traveling through the expanding Universe. The *redshift* z is also related to the cosmic scale factor (and look back time) and defined as

$$z = \frac{\lambda_{\rm obs}}{\lambda_{\rm em}} - 1 = \frac{1}{a\,(t_{\rm em})}, \tag{1.1}$$

where $\lambda_{\rm em}$ and $\lambda_{\rm obs}$ are the emitted and observed wavelengths of radiation, and $a\,(t_{\rm em})$ is the cosmic scale factor at time $t_{\rm em}$ when light was emitted.

[5]Secondary anisotropies in the CMB are generated during the travel of the photons through the Universe.

[6]The Hubble time defines the age of the Universe and equals to the inverse of the Hubble parameter

$$t_{\rm H} = 1/H_0 \approx 13.8\ {\rm Gyr}. \tag{1.2}$$

studies of the CMB radiation it has also been realized that the observed temperature anisotropies are simply too small to be produced by the primordial baryonic matter. Therefore, the pure baryonic structure formation model failed to reproduce the observed Universe. However, the solution to this problem was already suggested in the early 1930s. Studies of the stellar motions in the Galactic plane (Oort 1932; a method first suggested in Kapteyn 1922), galaxy clusters (Zwicky 1933), and, later, the rotational curves of spiral galaxies (Rubin & Ford 1970) showed that a significant amount of mass is not visible (*missing*), suggesting the existence of *hidden* or *dark matter*. This matter is believed to be made of non-baryonic particles that interact with normal matter only by gravitational forces, and do not emit or absorb electromagnetic radiation. In 1980s the *Cold Dark Matter, (CDM)* was introduced (Peebles 1982; Blumenthal et al. 1984; Bond & Efstathiou 1984; Primack & Blumenthal 1984) and it was theorized to consist of *weakly interacting (collisionless) massive particles* (WIMPs)[7]. The introduction of CDM into the structure formation models became a key solution to the problem described by Lifshitz (1946): as CDM is collisionless, its gravitational collapse is not opposed by radiation pressure, hence, collapse can proceed much faster than in the case of normal baryonic matter.

Finally, the theory of CDM and, later, observations of the CMB led to the creation of the hierarchical structure formation theory (Press & Schechter 1974; Lacey & Cole 1993), which is now the leading cosmological model of structure formation incorporated into the ΛCDM formalism. In this model everything starts in the *linear* regime, characterized by the merging of dark matter on the distortions created by the cosmic inflation. With time, these small density perturbations ($\delta\rho/\rho << 1$) produced progressively denser and denser dark matter systems. Then, after density perturbations grew sufficiently and became substantially denser than the mean density of the Universe ($\delta\rho/\delta \gtrsim 1$), structure formation entered the *nonlinear* regime, during which the clumps of dark matter experienced gravitational collapse and produced a filamentary structure (halos and voids). After the radiation decoupled from baryonic matter, the latter started to mimic the evolution of the non-baryonic dark matter. Attracted by the gravitational forces of the dark matter halos, baryons sank into these potential wells and, when their density was sufficient, collapsed under gravitational force. Because baryons can lose their energy through collisional processes, they collapse to the center of the systems, while collisionless dark matter continues to orbit the halo. Because of angular momentum conservation, the baryons evolve to a rotationally supported configuration. As a result, the gas is distributed in a rotating disk system.

[7]Initial models described a *hot* dark matter consisting of neutrinos with very small mass, since they almost do not interact with other matter. However, this theory predicted that the clusters of galaxies must have been formed first and then somehow fragmented into separate galaxies; a picture which is in conflict with high-redshift observations.

As the gas in these *protogalaxies* cools down and becomes denser, the process of star formation is triggered and the first stars are born. At later times these structures evolve via internal and external processes such as gas accretion or various types of merging[8]. Finally, the gravitational force arranged galaxies in groups and clusters, forming a top order structure, which is called the *cosmic web* (White & Rees 1978; Efstathiou & Silk 1983; Bond et al. 1996; Springel et al. 2006; Scannapieco et al. 2009).

1.2 QUASARS. GALAXY EVOLUTION CONTINUES

The success of the hierarchical structure formation model has led to the understanding of how the galaxies and galaxy clusters were formed in the Universe. Shortly after these complex systems equilibrated in the potential wells of dark matter haloes, the evolution of galaxies proceeded by recycling the gas reservoir, with clumps of the sufficiently fragmented, dense, and cool gas collapsing gravitationally and forming stars. However, it is believed that most of the galaxies have experienced another *active phase* in their evolution, characterized by the increased energetic emission from their central (nuclear) regions and named the *quasar phase*.

The discovery of quasars,[9] with initial observations of object 3C 273 (Hazard et al. 1963; Schmidt 1963; Oke 1963), has revolutionized our understanding of galaxy evolution. Its observed spectrum contained broad emission lines, several of which were identified as hydrogen Balmer emission lines (Balmer 1885), but having a redshift of $z \simeq 0.16$, strikingly suggesting a clear extragalactic origin of this highly energetic phenomenon. After more than 50 years of research we now know that quasars are the extremely luminous and compact nuclei of distant galaxies[10], whose radiation is generated by entirely different physical mechanisms than the ones that power stars.

In contrast to the thermal radiation of typical galaxies that can be approximately described by the blackbody spectrum (or a collection of blackbody spectra of all stars in galaxy), the spectrum of quasars is dominated by non-thermal radiation. It is believed

[8] Described processes lead to the formation of all three major morphological types of observed galaxies: spiral, elliptical and irregular (Hubble 1926).

[9] Orignially, the name *quasi-stellar radio sources* (*quasars*) was used to explain the star-like extragalactic sources that are bright in optical and radio bands. However, later it was found (Ryle & Sandage 1964; Sandage 1965) that other objects of the same properties do not have strong radio emission, hence the name *quasi-stellar object* (QSO) was introduced. Now we know that these are, essentially, the same class of objects, therefore the names quasar and QSO are interchangeably used in literature and throughout this thesis.

[10] An explanation first suggested by M.Schmidt in his original paper on the discovery of quasars

that the central engine of quasar activity is the Supermassive Black Hole (SMBH) lying in the sub-parsec sized center of galaxy. Its enormous gravitational pull brings the gas close to the event horizon. However, in order to fall onto the SMBH, gas needs to lose its angular momentum first. The necessary mechanism is provided by the accretion disk (Salpeter 1964; Zel'dovich & Novikov 1964; Lynden-Bell 1969; Shakura & Sunyaev 1973), in which gravity forces the gas to spiral towards the event horizon along the tendex line, while intense frictional forces heat the gas to extreme temperatures. Consequently, the gravitational energy of the gas is converted into the photons that are emitted mostly at UV and X-ray wavelengths. The total luminosity of quasars produced via accretion of gas onto the SMBH is typically $L \simeq 10^{46}$erg s^{-1}, which is ≈ 100 times more than the combined energy emitted by all stars in a typical galaxy. Considering a spherically symmetric configuration this luminosity corresponds to a SMBH with mass $M_\bullet \simeq 10^8 M_\odot$ [11]. It would take at least $t_{\rm grow} \simeq 5 \times 10^7$ yr to grow a SMBH of such mass (assuming Eddington luminosity and 10% mass-to-luminosity conversion efficiency). It is unlikely that such temporary extended process could take place without influencing the host galaxy.

Indeed, one of the major achievements of the previous decades is the discovery of dormant SMBHs in the centers of all spheroidal galaxies (Soltan 1982; Kormendy & Richstone 1995; Magorrian et al. 1998; Yu & Tremaine 2002). Moreover, there appears to be a tight correlation between the mass of the central SMBHs ($M_\bullet$) and parameters of the host galaxies, such as mass of the host galaxy bulges ($M_{\rm bulge}$) and bulge stellar velocity dispersion ($\sigma_\star$), and total galaxy luminosity (L) (Kormendy & Richstone 1995; Magorrian et al. 1998; Ferrarese & Merritt 2000; Gebhardt et al. 2000; Graham et al. 2001; Häring & Rix 2004; Feoli & Mele 2005, 2007; Graham & Driver 2007; McConnell & Ma 2013; Kormendy & Ho 2013). For instance, probably the most striking is the tight correlation between the mass of the SMBHs and the buldge mass of their parent galaxies, $M_\bullet \sim 10^{-3} M_{\rm bulge}$. This remarkable correlation implies that galaxies and their SMBHs have co-evolved through cosmic time and shared physical mechanisms responsible for establishing their observed properties (despite the utmost differences in the scales). Additional observational hints advocating for co-evolution of quasars and galaxies since the earliest cosmic time come from the determined space density distribution of quasars. This distribution peaks around $z \simeq 2-3$ (Fan et al. 2001; Richards et al. 2009; Croom et al. 2009). It suggests that quasar activity might be triggered by merging between host galaxies, which in earlier cosmic times ($z \simeq 2-3$) was happening much more frequently, than today. These findings are also supported by models of hierarchical structure formation and quasar and galaxy co-evolution (Wyithe & Loeb 2003; Springel et al.

[11] If the SMBH is radiating at Eddington luminosity $L_{\rm edd}$, which is the maximum allowed by the steady-state accretion

2005b; Hopkins et al. 2008; Marulli et al. 2008; Conroy & White 2013)[12], which also posit that every massive galaxy underwent a luminous quasar phase, which is responsible for the growth of the supermassive black holes. In many theories powerful feedback from quasars influences the properties of the galaxies themselves (Sanders et al. 1988; Silk & Rees 1998). Energetic quasar radiation can heat and expel the reservoir of gas needed for star formation from the host galaxy, i.e, quench the star formation process. Thus, quasar feedback can regulate the evolution of galaxies and potentially determine why some galaxies are *red* and *dead* while others remain *blue* and thus star-forming (Springel et al. 2005a; Hopkins et al. 2006, 2007b,c).

Our understanding of how correlations between SMBHs properties and their host galaxies were established over cosmic time depends significantly on the timescale of quasar activity. Unfortunately this timescale, now constrained to within only several orders of magnitude, is still a missing piece of the evolutionary puzzle. For instance, the models of accretion are incomplete without proper estimates of the quasar activity timescales. It is not yet well determined if most of the SMBH's mass was gained through the luminous quasar phase ($L \simeq L_{\rm edd}$) or the less efficient and less luminous phases ($L < L_{\rm edd}$). Moreover, as mentioned previously, the powerful quasar feedback may regulate the process of star formation in galaxies, making the duration of the quasar phase important for explaining how the galactic stellar populations evolved. It is a primary goal of this work to develop a method to put tight constraints on the timescale of quasar activity. Naturally, this will be impossible without first building an intuition about the expected values of this timescale, obtained through various approaches. We therefore review the current state of this field in Section 1.4. However, before proceeding, we should cover another essential period in the history of the Universe in which the quasars are believed to take center stage: the epoch of helium reionization.

1.3 Intergalactic medium. Reionization of hydrogen and helium

The *intergalactic medium* (IGM) is the vast space that lies between galaxies, which contains the bulk of baryonic matter. Its fate is strongly connected to that of galaxies and quasars. It is believed that the IGM provides building blocks for galaxy forma-

[12]Remarkably, observations of high-redshift quasars ($z \simeq 6-7$) indicate that some SMBHs with masses $10^8 - 10^9 M_\odot$ are already present in ~ 1 Gyr old Universe (Willott et al. 2003; Kurk et al. 2007; Jiang et al. 2007). Therefore, another challenge for simulations is to understand how the "seeds" of SMBHs appeared so early in the Universe.

tion and plays the role of the gas reservoir from which galaxies can acquire gas for star formation. Galaxies and quasars, on the other hand, produce a large number of ionizing photons that, if they escape into the IGM, can change the state of the intergalactic gas and, subsequently, influence their own evolution. Thus, the history of galaxy and quasar evolution would be incomplete without knowing the history of the IGM. One of its most important periods - *the epoch of reionization (EoR)* - is of particular significance for the work presented on the pages of this thesis. For thorough review we refer the reader to the following works by Fan et al. (2006a); Meiksin (2009); McQuinn (2015); Mesinger (2016).

The epoch of reionization is a major phase transition that occurred in the Universe when the ionization state of the intergalactic gas changed from neutral to once again highly ionized plasma. It is also responsible for the dramatic increase in the temperature of the IGM. Since the baryonic matter in the IGM is mostly hydrogen and helium atoms (which have different ionization potentials), the EoR can be divided into two steps: hydrogen reionization and helium reionization.

Hydrogen reionization

After hydrogen and helium atoms were formed during the Recombination Era the Universe transitioned into the *Dark Ages*. Baryonic matter remained mostly neutral and radiation was represented only by CMB photons and the 21 cm spin line of neutral hydrogen. It is believed that this period lasted for $\sim$ 400 million years until first stars, and then galaxies were formed around $z \sim 10 - 70$ (Barkana & Loeb 2001; Naoz et al. 2006; Bromm & Yoshida 2011). Once the stellar populations of these newborn galaxies started emitting ionizing radiation with energy $\gtrsim$ 13.6 eV the reionization of neutral hydrogen in the IGM began (H I $\rightarrow$ H II). A number of detailed cosmological simulations suggest that hydrogen reionization is a largely inhomogeneous process that started with the growth of isolated H II regions formed around individual galaxies. As time passed, such regions of ionized hydrogen expanded and eventually overlapped, filling the entire Universe (Gnedin 2000; Lidz et al. 2007; McQuinn et al. 2007; Gnedin & Kaurov 2014; Bauer et al. 2015).

We do not yet exactly know the starting point and the duration of hydrogen reionization, although various observational probes suggest that intergalactic hydrogen was reionized in redshift range $z \simeq 6 - 10$[13]. The most robust indicator of when H I

[13] In addition, there is a debate about the sources of hydrogen reionization. While the commonly accepted model is galaxy driven hydrogen reionization (Faucher-Giguère et al. 2008a; Becker & Bolton 2013), it strongly depends on the highly-uncertain fraction of ionizing photons that can escape from galactic environment into the IGM, $f_{\rm esc}$. If this number is high, then observations imply the end of H I reionization around $z \sim 6$ (Robertson et al. 2010; Finkelstein et al. 2012, 2015). However, if $f_{\rm esc}$ is low, then another sources of ionizing radiation, probably a population of undetected low-mass galaxies, are responsible for ionizing the intergalactic hydrogen.

reionization ended is the H I Lyα forest in the spectra of bright high-redshift quasars. Due to the expansion of the Universe, quasar radiation is continuously redshifted as it travels through the IGM. When photons with wavelengths shorter than Lyα are redshifted to $\lambda_{\rm rest} \simeq 1216$Å, they can be absorbed by individual clouds of neutral hydrogen. Such a process produces thin aborption lines (*trees*) blueward of the Lyα emission line in the spectrum of a quasar. A collection of such trees of H I Lyα absorption is called the H I Lyα *forest*. However, if the amount of neutral hydrogen is significant enough, it will produce the *Gunn-Peterson trough*: an opaque, completely saturated region in quasar spectrum (Gunn & Peterson 1965). Several studies of the Lyα opacity in the spectra of high-redshift quasars detected such troughs above $z \simeq 6$, whereas the H I Lyα forest is detected at lower redshifts, suggesting that the reionization of intergalactic hydrogen is mostly complete by $z \simeq 5.5 - 6$ (Becker et al. 2001; Djorgovski et al. 2001; Fan et al. 2002, 2006b; White et al. 2003; Songaila 2004; Becker et al. 2015).

Additional constraints come from the analysis of the secondary anisotropies in the CMB radiation. This includes measurements of the IGM's optical depth $\tau_{\rm e}$ due to Thomson scattering of the CMB photons on free electrons produced during the reionization of hydrogen. The most recent measurements of $\tau_{\rm e}$ from Planck data yield $\tau_{\rm e} = 0.066 \pm 0.016$ (Planck Collaboration et al. 2015b), implying that reionization happened at $z = 8.8^{+1.7}_{-1.4}$ under very simplified assumption that it was an instantaneous process. Also, the EoR induces the small-scale fluctuations in the temperature of the CMB, known as the kinetic Sunyaev-Zel'dovich effect (Sunyaev & Zeldovich 1980), placing an upper limit on the duration of hydrogen reionization $\Delta z < 5.4$ (George et al. 2015).

In contrast, the beginning of H I reionization is still mostly uncharted territory. The number of bright quasars at high redshifts declines rapidly and the IGM simultaneously becomes denser and more neutral, which complicates our ability to obtain information about the EoR. One of the most promising methods to study the beginning of hydrogen reionization is the observations of the redshifted 21 cm spin line of neutral hydrogen. A number of dedicated observational projects (e.g. LOFAR, PAPER, MWA, SKA) might soon revolutionise our understanding of the dawn of reionization.

Helium reionization

It is believed that the morphology of helium reionization (He I $\rightarrow$ He II $\rightarrow$ He III) is similar to that of hydrogen, with two significant differences. First of all, it was likely a two step process. Since H I and He I share similar ionization potentials ($h\nu = 13.6$ eV vs. $h\nu = 24.6$ eV, respectively), helium was likely singly ionized (He I $\rightarrow$ He II) by the same sources at similar redshifts ($z \gtrsim 6$). However, these

stars could not produce the required hard photons ($h\nu \gtrsim 54.4$ eV) to doubly ionize helium (He II $\rightarrow$ He III), which introduces the second major difference between the hydrogen and helium reionization epochs, namely their sources. In contrast to the suspected galaxy-driven hydrogen reionization, it is believed that quasars are responsible for final stages of helium reionization. A set of semi-analytic calculations (Furlanetto 2009; Davies & Furlanetto 2014) together with full hydrodynamical and radiative transfer simulations (McQuinn et al. 2009a; Compostella et al. 2013, 2014) predict that He II reionization has been delayed relative to the hydrogen until $z \simeq 3-4$, concurring with the observed rapid increase in the space density of quasars at $z \simeq 3$ and hardening of the intergalactic ionizing background (Hopkins et al. 2007a; Furlanetto & Oh 2008; Willott et al. 2010).

Analogous to hydrogen reionization, constraints on He II reionization are possible with direct observations of the intergalactic He II Lyα ($\lambda_{\rm rest} = 303.78$Å) absorption in the spectra of $z \simeq 3-4$ quasars, which is, however, only possible from space in the far UV, e.g. with *Cosmic Origins Spectrograph* (COS) onboard *Hubble Space Telescope* (HST). The results of the previous campaigns (Shull et al. 2010; Worseck et al. 2011; Syphers & Shull 2013, 2014; Worseck et al. 2014) indicate the dramatic decrease in the opacity of the He II Lyα forest at redshifts $z \lesssim 3$, which implies the detection of the tail end of He II reionization, as predicted by numerical simulations (McQuinn et al. 2009a; Compostella et al. 2013, 2014). However, the same models predict completely saturated He II Lyα absorption in quasar spectra above $z > 3.2$, inconsistent with detected optically thin regions of IGM at $z \gtrsim 3.5$ (Worseck et al. 2011, 2014; Worseck in prep.). This may, in fact, indicate that He II reionization started much earlier than suggested by simulations, suggesting that other sources of hard photons at $z \gtrsim 4$ maybe required in order to reionize intergalactic helium by $z \simeq 3.5$. Recent results (Giallongo et al. 2015) imply that population of faint quasars might exist at $z \gtrsim 4$ and be responsible for early He II reionization. Alternative scenarios suggest other, more exotic sources of energetic photons for He II reionization such as thermal emission from shock heated gas during structure formation at higher redshifts (Miniati et al. 2004), redshifted X-ray radiation from primordial formation of black holes or globular clusters (Ricotti & Ostriker 2004; Power et al. 2009), and high-redshift mini-quasars (Madau et al. 2004). Unfortunately, the sensitivity limit of HST/COS makes it very ambiguous to directly observe and study intergalactic He II Lyα absorption in spectra of $z \gtrsim 4$ quasars. Thus, another indirect method should be used to constrain the helium reionization at high redshifts. One possibility is to measure the temperature of the IGM, which is expected to increase dramatically during He II reionization (Miralda-Escudé & Rees 1994; Abel & Haehnelt 1999). Section 5 of this thesis is also devoted to this problem.

Clearly, since most of the models posit that quasars are the main drivers of helium reionization, they depend on several most important quasar parameters, such as lu-

minosity and abundance, which define the budget of He II ionizing photons available for reionization of helium atoms in a certain period of time. In this thesis I focus on constraining another missing piece of the puzzle, the timescale of quasar activity, which determines the rate of growth of ionized structures around individual objects and the total duration of He II reionization.

1.4 THE LIFETIME OF QUASARS

As I illustrated in previous sections, the holy grail of research focusing on SMBH-galaxy co-evolution and reionization history is the quasar lifetime and related to it *duty cycle*, $t_{\rm dc}$, defined as the fraction of time that a galaxy hosts an active quasar. This knowledge would shed light on the triggering mechanism for quasar activity (thought to be either major galaxy mergers or secular disk instabilities), on how gas funnels to the center of the galaxy from these mechanisms, and on the properties of the inner accretion disk (Goodman 2003; Hopkins et al. 2008; Hopkins & Quataert 2010). It is well-known that the duty cycle of a population of objects can be inferred by comparing its number density and clustering strength (Cole & Kaiser 1989; Martini & Weinberg 2001; Haiman & Hui 2001). But to date this method has yielded only very weak constraints on the quasar duty cycle of $t_{\rm dc} \sim 10^6 - 10^9$ yr (Adelberger & Steidel 2005; Croom et al. 2005; Shen et al. 2009; White et al. 2012; Conroy & White 2013) because of uncertainties in the dark matter halo population of quasars (White et al. 2012; Conroy & White 2013). Constraints on the duty cycle with comparable uncertainty come from comparing the time integral of the quasar luminosity function to the present day number density of black holes (Yu & Lu 2004).[14]

Moreover, these methods that constrain $t_{\rm dc}$ do not shed light on the duration of individual accretion episodes, i.e., the average quasar lifetime ($t_{\rm lt}$). For instance, if quasars emit their radiation in ~ 1000 bursts over the course of a Hubble time, with each episode having duration of $t_{\rm lt} \sim 10^5$ yr, this would be indistinguishable from steady continuous emission for $t_{\rm lt} \sim 10^8$ yr. The former timescale of $t_{\rm lt} \sim 10^5$ yr is consistent with the picture of Goodman (2003), who argues that the outer regions of quasar accretion disks are unstable to gravitational fragmentation and cannot be much larger than ~ 1 pc. Such small disks would need to be replenished $\sim 100-1000$ times over to grow a SMBH, which could generically result in episodic variability on timescales of $10^5 - 10^6$ yr. However, the latter timescale $t_{\rm lt} \sim 10^8$ yr is roughly what is needed to grow the mass of a black hole by one *e*-folding (the Salpeter time; Salpeter (1964)), and the timescale galaxy merger simulations suggest for the duration of a

[14]This inference suffers from the uncertainties related to the black hole demographics in local galaxy populations, and scaling relations (Kormendy & Ho 2013).

quasar episode (Hopkins et al. 2005).

Current constraints on the quasar lifetime are weak ($t_{\rm lt} \gtrsim 10^4$ yr; Martini 2004), such that lifetimes comparable to the Salpeter time are still plausible. This limit derives from the line-of-sight H I proximity effect – the enhancement in the ionization state of H I in the quasar environment as probed by the H I Lyα forest. The argument is that the presence of a line-of-sight H I proximity effect in $z \sim 2-4$ quasars implies that quasars have been emitting continuously for an equilibration timescale, which corresponds to about 10^4 yr in the $z \sim 2-4$ IGM. Schawinski et al. (2010) and Schawinski et al. (2015) argued for variability of several orders of magnitude in quasar luminosity on short $\sim 10^5$ yr timescales, based on the photoionization of quasar host galaxies and light travel time arguments. However, these constraints are indirect and plausible alternative scenarios related to AGN obscuration could explain the observations without invoking short timescale quasar variability. Furthermore, the discovery of quasar powered giant Lyα nebulae at $z \sim 2$ (Cantalupo et al. 2014; Hennawi et al. 2015) with sizes of ~ 500 pkpc implies quasar lifetimes of $\gtrsim 10^6$yr, in conflict with the Schawinski et al. (2010) and Schawinski et al. (2015) estimates. Recently, the presence of high-equivalent width ($\rm EW_{Ly\alpha} \geq 100$Å) Ly$\alpha$ emitters (LAEs) at large distances $\sim 3-20$ pMpc from hyper-luminous quasars has been used to argue for quasar lifetimes in the range of $1\,{\rm Myr} \lesssim t_{\rm Q} \lesssim 30\,{\rm Myr}$, based on the presumption that such LAEs result from quasar powered Lyα fluoresence (Trainor & Steidel 2013; Borisova et al. 2015). However, at such large distances $\sim 3-20$ pMpc the fluorescent boost due to the quasar is far fainter than the fluxes of the LAEs in the Trainor & Steidel (2013) and Borisova et al. (2015) surveys, and hence some other physical process intrinsic to the LAE and unrelated to quasar radiation must be responsible for these sources[15].

There is an analogous proximity effect in the He II Lyα forest that, as this work shows, is much more sensitive to the quasar lifetime than the line-of-sight H I proximity effect. The He II proximity effect has been detected at $2.7 < z < 3.9$ (Hogan et al. 1997; Anderson et al. 1999; Heap et al. 2000; Syphers & Shull 2014; Zheng et al. 2015). Figure 1.1 shows the two well-studied examples (Shull et al. 2010; Syphers & Shull 2014) that highlight the observed variance in He II proximity zone sizes and shapes (Zheng et al. 2015). HE 2347−4342 may be either young

[15]Using the expression for the fluorescent surface brightness in eqn. (12) of Hennawi & Prochaska (2013), and assuming fluorescent LAEs have a diameter of 1.0″, it can be shown that the expected fluorescent boost from a quasar at a distance of $R = 15$ pMpc is a factor of $\gtrsim 400$ smaller than the fluxes of the Borisova et al. (2015) LAEs. The Trainor & Steidel (2013) survey probes deeper and considers smaller distances $R = 3$ pMpc where the fluorescent boost is larger, but a similar calculation shows the fluorescent Lyα emission is nevertheless a factor of $\gtrsim 5$ smaller than the Trainor & Steidel (2013) LAEs. Hence quasar powered Lyα fluorescence cannot be the mechanism powering high equivalent-width LAEs at such large distances.

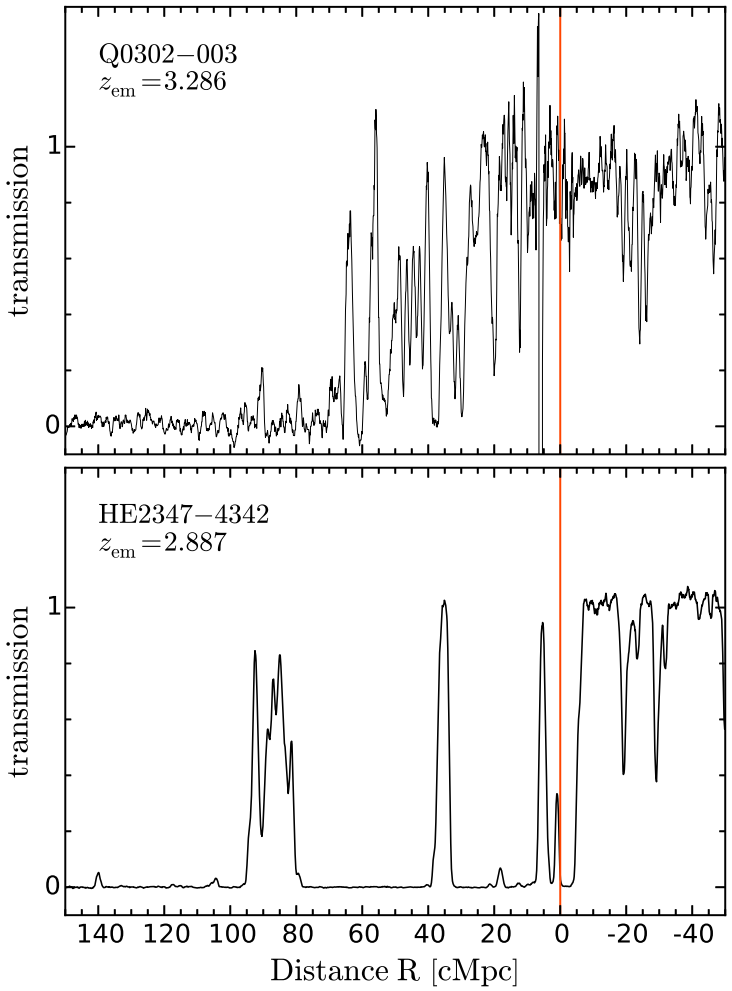

FIGURE 1.1: *UV He II Lyα absorption spectra (R* ∼ 16,000*) of quasars Q 0302−003 (*top*;* $z_{\rm em}$ = 3.286*) and HE 2347−4342 (*bottom*;* $z_{\rm em}$ = 2.887*) as a function of comoving distance from the quasar. Both original spectra were rebinned by a factor of* 3 *to yield the Nyquist sampling and then smoothed with a 'boxcar' kernel of width w* = 11*. Red vertical lines indicate the location of the quasars.*

($t_{\rm Q}$ < 1 Myr, Shull et al. 2010) or peculiar due to an infalling absorber (Fechner et al. 2004). Q 0302−003 shows a large proximity zone of 60 − 100 comoving Mpc depending on the local density field (Syphers & Shull 2014). Adopting a plausible range in the other relevant parameters (quasar luminosity, IGM He II fraction and IGM clumpiness), Syphers & Shull (2014) find that Q 0302−003 may have shone for 0.2 − 31 Myr. The simplifying assumptions of a homogeneous IGM with a He II fraction of unity only allow for rough estimates of the quasar lifetime (Hogan et al. 1997; Anderson et al. 1999; Zheng et al. 2015).

In addition, constraints on the quasar lifetime have also been derived from the so-called transverse proximity effect, i.e. the enhancement of the UV radiation field around a foreground quasar which gives rise to increased IGM transmission in a background sightline. While several effects like anisotropic quasar emission, episodic quasar lifetimes, and overdensities around quasars make a statistical detection of the transverse proximity effect challenging (e.g. Hennawi et al. 2006; Hennawi & Prochaska 2007; Kirkman & Tytler 2008; Furlanetto & Lidz 2011; Prochaska et al. 2013), it has been detected in a few cases, either as a spike in the IGM transmission (Jakobsen et al. 2003; Gallerani et al. 2008) or as a locally harder UV radiation field in the background sightline (Worseck & Wisotzki 2006; Worseck et al. 2007; Gonçalves et al. 2008; McQuinn & Worseck 2014). For the handful of quasars for which such detections have been claimed, the transverse light crossing time between the foreground quasar and the background sightline provides a lower limit to the quasar lifetime of $t_{\rm Q} = 10 - 30$ Myr.

The goal of this work is to understand whether the properties of He II Lyα line-of-sight proximity zones can constrain the duration of the quasar phase. This work is motivated by the large number of He II Lyα forest proximity zones that have been observed over the last five years with the HST/COS (Shull et al. 2010; Worseck et al. 2011; Syphers et al. 2012). Another motivation is to generalize previous analyses from the restrictive assumption of $x_{\rm HeII} = 1$. Even for ionized gas, He II proximity zones around $z \simeq 3$ quasars provide a much more powerful tool for constraining quasar lifetimes than H I proximity zones. In order to produce a detectable proximity zone, the quasar must shine for a time comparable to or longer than the timescale for the IGM to attain equilibrium with the enhanced photoionization rate Γ, known as the equilibration timescale $t_{\rm eq} \simeq \Gamma^{-1}$. Current measurements of the UV background in the $z \sim 3$ H I Lyα forest yield an H I photoionization rate $\Gamma_{\rm HI}^{\rm bkg} \simeq 10^{-12}\,{\rm s}^{-1}$ (Becker et al. 2013) implying $t_{\rm eq} \simeq 3 \times 10^4\,{\rm yr}$. On the other hand, as we argue in § 3.1, current optical depth measurements at $z \sim 3$ (Worseck et al. 2011) imply a He II photoionization rate $\Gamma_{\rm HeII}^{\rm bkg} \simeq 10^{-15}\,{\rm s}^{-1}$, resulting in $t_{\rm eq} \simeq 3 \times 10^7\,{\rm yr}$. Thus, He II proximity zones can probe quasar lifetimes three orders of magnitude larger, closer to the Salpeter timescale. Moreover, the fact that the He II background is ~ 1000 times lower than the H I background implies that the radius within which the quasar dominates over the background will be ~ 30 times larger for He II, and given these much larger zones uncertainties due to density enhancements around the quasar will be much less significant (Faucher-Giguère et al. 2008b).

1.5 Outlook of the Thesis

This thesis consists of three major parts. First, we discuss the numerical simulations we use and describe our radiative transfer algorithm in Chapter 2. In Chapter 3 we explore the physical properties of the intergalactic medium and conditions in He II proximity zones. We introduce a new way of thinking about the proximity zones via time-evolution of He II fraction and the idea of computing stacked He II Lyα transmission profiles. Chapter 4 investigates the dependence of stacked He II spectra on the parameters governing quasars[16]. We introduce *thermal proximity effect* in Chapter 5 and discuss how the quasar changes the thermal state of the intergalactic medium. We present an analysis of the line-of-sight H I Lyα power spectrum statistics and show with MCMC calculations how it can be used to constrain an average He II fraction in the intergalactic medium and the lifetime of quasars[17].

Throughout this work we assume a flat ΛCDM cosmology with Hubble constant $h = 0.7$, $\Omega_{\rm m} = 0.27$, $\Omega_{\rm b} = 0.046$, $\sigma_8 = 0.8$ and $n_s = 0.96$ (Larson et al. 2011), and helium mass fraction $Y_{\rm He} = 0.24$. All distances are in unites of *comoving* Mpc, i.e., cMpc.

In order to avoid confusion, we distinguish between several different timescales that govern the duration of quasar activity. As noted above, the *duty cycle* $t_{\rm dc}$ refers to the total time that galaxies shine as active quasars integrated over the age of the universe. On the other hand, one of the goals of this work is to understand the constraints that can be put on the *episodic lifetime* $t_{\rm episodic}$, which is the time spanned by a single episode of accretion onto the SMBH. But in the context of proximity effects in the IGM, one actually only constrains the quasar *on-time*, which will denote as $t_{\rm Q}$. If we imagine that time $t = 0$ corresponds to the time when the quasar emitted light that is just now reaching our telescopes on Earth, then the quasar on-time is defined such that the quasar turned on at time $-t_{\rm Q}$ in the past. This timescale is, in fact, a lower limit on the quasar episodic lifetime $t_{\rm episode}$, which arises from the fact that we observe a proximity zone at $t = 0$ when the quasar has been shining for time $t_{\rm Q}$, whereas this quasar episode may indeed continue, which we can only record on Earth if we could conduct observations in the future. For simplicity in the text, we will henceforth refer to the quasar on-time as the *quasar lifetime* denoted by $t_{\rm Q}$, but the reader should always bear in mind that this is a lower limit on the quasar lifetime.

[16] Chapters 3-4 are based on the work presented in Khrykin et al. (2015), submitted to ApJ

[17] This chapter is based on work presented in Khrykin et al. (2016) in prep

Chapter 2

Numerical model

"The purpose of computing is insight, not numbers."
Richard Hamming

2.1 Hydrodynamical simulations

To study the impact of quasar radiation on the intergalactic medium we post-process the outputs of a smooth particle hydrodynamics (SPH) simulation using a one dimensional radiative transfer algorithm. For the cosmological hydrodynamical simulation, we use the Gadget-3 code (Springel 2005c) with 2×512^3 particles and a box size of $25h^{-1}$ cMpc. We extract 1000 sightlines, which we will refer to as skewers, from the SPH simulation output at a snapshot corresponding to $z = 3.1$. In § 4.5.1 and § 5 we also consider skewers at a higher redshift of $z = 3.9$. We identify quasars in the simulation as dark matter halos with masses $M > 5{\times}10^{11} M_{\odot}$, by running a friends-of-friends algorithm (Davis et al. 1985) on the dark matter particle distribution. While this mass threshold is 1 dex lower than the halo mass inferred from quasar clustering measurements (White et al. 2012; Conroy & White 2013), our simulation cube does not capture enough such massive halos. However, because the He II proximity effect extends many correlation lengths ($r_0 \approx 10h^{-1}$ Mpc, White et al. 2012), the use of the less clustered halos will not make a difference at most radii we consider.

Starting from the location of the quasars, we create skewers by casting rays through the simulation volume at random angles, and traversing the box multiple times. We use the periodic boundary conditions to wrap a skewer through the box along the chosen direction. This procedure results in skewers from the quasar location through

the intergalactic medium that are 318 cMpc long, significantly larger than the length of our simulation box and the He II proximity region. Our skewers have 27,150 pixels which corresponds to a spatial interval of $dR = 0.012$ cMpc or a velocity interval $dv = 0.893$ km s^{-1}. This is sufficient to resolve all the features in the He II Lyα forest.

2.2 1D RADIATIVE TRANSFER ALGORITHM

We extract the one-dimensional density, velocity, and temperature distributions along these skewers and use them as input to our post-processing radiative transfer algorithm[1], which is based on C^2-Ray algorithm (Mellema et al. 2006). Because this algorithm is explicitly photon conserving, it enables great freedom in the size of the grid cells and the time step. Our one-dimensional radiative transfer algorithm is extremely fast, with one skewer calculation taking ~ 5 seconds on a desktop machine, allowing us to run many realizations. In this section, we describe the salient features of our radiative transfer algorithm, and we refer the reader to the original Mellema et al. (2006) paper on the C^{2}Ray code for additional details.

2.2.1 MODEL OF THE IONIZING SOURCES

We put a single source of radiation, the quasar, at the beginning of each sightline, and trace the change in the ionization state and temperature of the IGM for a finite time, t, as the radiation is propagated[2]. The spectral energy distribution (SED) of the source is modeled as a power-law, such that the quasar photon production rate at any frequency $\nu \geq \nu_{\rm th}$ is

$$N_\nu = \frac{\alpha Q_{\rm 4Ry}}{\nu_{\rm th}} \left(\frac{\nu}{\nu_{\rm th}}\right)^{-(\alpha+1)}, \tag{2.1}$$

where $Q_{\rm 4Ry}$ is the photon production rate at the He II ionization threshold of 4 Ry or a corresponding threshold frequency $\nu_{\rm th} = 1.316 \times 10^{16}$ Hz corresponding to this threshold. We assume a spectral index of $\alpha = 1.5$, $f_\nu \sim \nu^{-\alpha}$, consistent with the

[1] Post-processing is a good approximation because the thermal state of the gas changes only when the quasar reionizes it, increasing its temperature by a factor of ~ 2 (McQuinn et al. 2009a). Even in this case, the ~ 10 Myr time since the quasar turned on is insufficient for intergalactic gas to respond dynamically, as the relaxation time is $(1+\delta)^{1/2}$ of the Hubble time, where δ is the gas overdensity.

[2] For simplicity we assume a 'light bulb' model for a quasar in our simulations, which implies that the luminosity of the quasar does not change over time it is active.

measured values in stacked UV spectra of quasars (Telfer et al. 2002; Shull et al. 2012; Lusso et al. 2015).

The r-band magnitudes of He II quasars in the HST/COS archive range from $r = 16.0 - 19.4$, with a median value of $r \simeq 18.25$. Following the procedure described in Hennawi et al. (2006), we model the quasar spectral-energy distribution (SED) using a composite quasar spectrum which has been corrected for IGM absorption (Lusso et al. 2015). By integrating the Lusso et al. (2015) composite redshifted to $z = 3.1$ against the SDSS filter, we can relate the r-band magnitude of a quasar to the photon production rate at the H I Lyman limit $Q_{1\mathrm{Ry}}$, which is then related to $Q_{4\mathrm{Ry}}$ by $Q_{4\mathrm{Ry}} = Q_{1\mathrm{Ry}} \times 4^{-\alpha}$, assuming the same power law SED governs the quasar spectrum for frequencies blueward of 1 Ry. This procedure implies that quasars in the range $r = 16.0 - 19.4$ have $Q_{4\mathrm{Ry}} = 10^{56.0-57.4}$ s^{-1}, with median $r \simeq 18.25$ and $Q_{4\mathrm{Ry}} = 10^{56.5}$ s^{-1}.

The quasar photoinization rate in every cell is given by

$$\Gamma_{\mathrm{QSO}} = \int_{\nu_{\mathrm{th}}}^{\infty} \frac{N_\nu e^{-\langle\tau_\nu\rangle}}{h_{\mathrm{P}}\nu} \frac{1 - e^{-\langle\delta\tau_\nu\rangle}}{\langle n_{\mathrm{HeII}}\rangle V_{\mathrm{cell}}} d\nu, \tag{2.2}$$

where $\langle\tau_\nu\rangle$ is the optical depth along the skewer from the source to the current cell, $\langle\delta\tau_\nu\rangle$ is the optical depth inside the cell, $\langle n_{\mathrm{HeII}}\rangle$ is the average number density of He II in this cell, V_{cell} is the volume of the cell, and h_{p} is Planck's constant. Here the angular brackets indicate time averages over the discrete time step δt.

Combining with eqn. (2.1), we can then rewrite eqn. (2.2) as

$$\Gamma_{\mathrm{QSO}} = \frac{\alpha Q_{4\mathrm{Ry}}}{n_{\mathrm{HeII}} V_{\mathrm{cell}} \nu_{\mathrm{th}}} \int_{\nu_{\mathrm{th}}}^{\infty} \left(\frac{\nu}{\nu_{\mathrm{th}}}\right)^{-(\alpha+1)} e^{-\langle\tau_\nu\rangle} \left(1 - e^{-\langle\delta\tau_\nu\rangle}\right) d\nu. \tag{2.3}$$

Although this equation for the photoionization rate is an integral over frequency, in practice the code is not tracking multiple frequencies. For the power-law quasar SED that we have assumed, and He II ionizing photon absorption cross section $\sigma_\nu \approx \sigma_{\mathrm{th}}(\nu/\nu_{\mathrm{th}})^{-3}$, eqn. (2.3) has an analytic solution that depends on $\langle\tau_{\mathrm{th}}\rangle$ and $\langle\delta\tau_{\mathrm{th}}\rangle$, the time-averaged optical depth to the cell and inside the cell, respectively, evaluated at the He II ionization threshold. Thus, given the values for these optical depths evaluated at the single edge frequency, we can compute the frequency-integrated photoionization rate.

The foregoing has considered the case of a single source of radiation, namely the quasar. This scenario is likely appropriate early on in He II reionization, when each quasar photoionizes its own He III zone. However, at later times, the intergalactic medium is filled with He II ionizing photons emitted by many sources. In order to properly model the radiative transfer along our skewer, we need to account for additional ionizations caused by this intergalactic ionizing background. We approximate

this background $\Gamma^{\rm bkg}_{\rm HeII}$ as being a constant in space and time, and simply add it into each pixel of our sightline to model the presence of these other sources

$$\Gamma_{\rm tot} = \Gamma_{\rm QSO} + \Gamma^{\rm bkg}_{\rm HeII}. \tag{2.4}$$

As such, this procedure does the full one-dimensional radiative transfer to compute the photoionization rate $\Gamma_{\rm QSO}$ produced by the quasar, but it would treat the background as an unattenuated and homogeneous radiation field present at every location. However, the densest regions of the IGM will be capable of self-shielding against ionizing radiation, thus giving rise to He II Lyman-limit systems (He II-LLSs). Within these systems our 1D radiative transfer algorithm always properly attenuates the quasar photoionization rate $\Gamma_{\rm QSO}$, however, if we take the the He II ionizing background $\Gamma^{\rm bkg}_{\rm HeII}$ to be constant in every pixel along the skewers, this would be effectively treating the He II-LLSs as optically thin, thus underestimating the He II fraction in the densest regions. In order to more accurately model the attenuation of the He II background by the He II-LLSs, we implement an algorithm described in McQuinn & Switzer (2010). In Appendix B we summarize this approach and show that the effect of self-shielding of He II-LLSs to the He II background $\Gamma^{\rm bkg}_{\rm HeII}$ has a negligible effect on the structure of the He II proximity zones. We nevertheless treat the He II LLSs with this technique for all of the results described in this work. In § 4.5.1 we also discuss the impact of spatial fluctuations in the He II ionizing background $\Gamma^{\rm bkg}_{\rm HeII}$ on our results (showing that the average transmission profile is largely unaffected by such fluctuations).

2.2.2 THE EVOLUTION OF HE II FRACTION

Having arrived at an expression for the photoionization rate in each cell, the next step is to determine the evolution of the He II fraction $x_{\rm HeII}$ in response to this time-dependent $\Gamma_{\rm tot}\,(t)$. The time evolution of the He II fraction is given by

$$\frac{dx_{\rm HeII}}{dt} = -\Gamma_{\rm tot}(t)\, x_{\rm HeII} + \alpha_{\rm A} n_{\rm e}\,(1 - x_{\rm HeII})\,, \tag{2.5}$$

which if $n_{\rm e}$ is independent of $x_{\rm HeII}$ (which holds at the 6% level) has the solution of

$$x_{\rm HeII}\,(t) = x_{\rm HeII,0} {\rm e}^{-\int_0^t dt' t_{\rm eq}(t')^{-1}} + \int_0^t dt' \alpha_{\rm A} n_{\rm e} {\rm e}^{-\int_0^{t'} dt'' t_{\rm eq}(t'')^{-1}}. \tag{2.6}$$

where $x_{\rm HeII,0}$ is the initial singly ionized fraction and $t_{\rm eq}$ is the equilibration timescale given by

$$t_{\rm eq} = (\Gamma_{\rm tot} + n_{\rm e}\alpha_{\rm A})^{-1}\,, \tag{2.7}$$

$n_{\rm e}$ is the electron density, and $\alpha_{\rm A}$ is the Case A recombination coefficient. In the limit when $\Gamma_{\rm tot}(t)$ does not change over t (and also the same for $\alpha_{\rm A} n_e$ which is less of an approximation) eqn. (2.6) simplifies considerably to

$$x_{\rm HeII}\,(t) = x_{\rm HeII,eq} + \Big(x_{\rm HeII,0} - x_{\rm HeII,eq}\Big)\, e^{-t/t_{\rm eq}}, \tag{2.8}$$

where we have defined the initial and equilibrium He II fractions as

$$x_{\rm HeII,0} = \frac{n_{\rm e}\alpha_{\rm A}}{\Gamma^{\rm bkg}_{\rm HeII} + n_{\rm e}\alpha_{\rm A}} \tag{2.9}$$

$$x_{\rm HeII,eq} = \frac{n_{\rm e}\alpha_{\rm A}}{\Gamma_{\rm tot} + n_{\rm e}\alpha_{\rm A}} \tag{2.10}$$

We discuss our treatment of He II ionizing photons produced by recombinations and the justification for adopting Case A in § 2.2.5 below. We have ignored collisional ionizations which contribute negligibly in proximity zones, where gas is relatively cool $\Big(T \sim 10^4{\rm K}\Big)$, and are even more highly suppressed for He II relative to H I. Given that the He II fraction starts at an initial value $x_{\rm HeII,0}$, eqn. (2.8) gives the He II fraction at a later time t, provided that $\Gamma_{\rm tot}$, $n_{\rm e}$, and $\alpha_{\rm A}$ are constant over this interval. As such, this equation is only exact for infinitesimal time intervals.

Following Mellema et al. (2006), we can compute the time averaged He II fraction inside a cell by averaging eqn. (2.8) over the discrete time-step δt, yielding

$$\langle x_{\rm HeII}\rangle = x_{\rm HeII,eq} + \Big(x_{\rm HeII,t} - x_{\rm HeII,eq}\Big)\Big(1 - e^{-\frac{\delta t}{t_{\rm eq}}}\Big)\frac{t_{\rm eq}}{\delta t}, \tag{2.11}$$

where $x_{\rm HeII,t}$ is the He II fraction at the previous timestep t. We then use eqn. (2.11) to calculate the time-averaged optical depth in the cell at the He II edge

$$\langle \delta\tau_{\rm th}\rangle = \langle x_{\rm HeII}\rangle n_{\rm He}\sigma_{\rm th}\Delta r, \tag{2.12}$$

where Δr is the size of the cell. Likewise, the time-averaged optical depth to the cell $\langle\tau_{\rm th}\rangle$ is computed by adding, in causal order, all the $\langle\delta\tau_{\rm th}\rangle$ of the cells lying between the source and the cell under consideration. The electron density $\langle n_{\rm e}\rangle$ and number density of He II atoms $\langle n_{\rm HeII}\rangle$ are similarly computed using eqn. (2.11).

The iterative process that we employ to find the new ionization state in each cell (see the flow-chart in Fig 2 of Mellema et al. 2006) can be described as follows. Starting with the cell nearest the source and moving outward, we:

1. Set the mean He II fraction $\langle x_{\rm HeII}\rangle$ to that given by the previous time-step (or the initial conditions, i.e., He II background).

2. Evaluate the optical depth between the source and the cell $\langle\tau_{\rm th}\rangle$ by summing the $\delta\tau_{\rm th}$ from the previous time-step.

3. Iterate the following until convergence of the He II fraction $\langle x_{\rm HeII}\rangle$ is achieved

   - compute the time-averaged optical depth $\langle\delta\tau_{\rm th}\rangle$ within the cell (eqn. 2.12);
   - compute the photoionization rate $\Gamma_{\rm tot}$ (eqns. 2.3 and 2.4);
   - compute the mean electron number density based on the current mean ionization state;
   - calculate the new He II fraction $x_{\rm HeII}\,(t)$ at this time step (eqn. 2.8), as well as its time-step averaged value $\langle x_{\rm HeII}\rangle$ (eqn. 2.11)
   - check for convergence

4. Once convergence is reached, advance to the next cell.

Following this procedure for every time-step, we thus integrate the time-evolution over time interval $t_{\rm Q}$, which denotes the quasar lifetime, yielding the He II fraction $x_{\rm HeII}$ at each location in space in the proximity zone.

2.2.3 IMPLEMENTATION OF HEATING AND COOLING

We assume that the excess from photoionization of helium heats the surrounding gas. In reality, instead of heating, the electron produced during the photoionization, can become a source of secondary (collisional) ionization, but they are unimportant for the highly ionized IGM, which will clearly be the case for He II proximity zones. The amount of heat injected per time interval is given by (Abel & Haehnelt 1999)

$$\frac{{\rm d}T}{{\rm d}t} \approx \frac{2Y_{\rm He}}{3k_{\rm B}(8-5Y_{\rm He})}\langle E\rangle\frac{{\rm d}x_{\rm HeII}}{{\rm d}t} \tag{2.13}$$

where ${\rm d}x_{\rm HeII}/{\rm d}t$ is the change in the He II fraction over the time step and $\langle E\rangle$ is the average excess energy of a photon above He II ionization threshold, which is given by

$$\langle E\rangle = \left[\frac{\int_{\nu_{\rm th}}^{\infty} N_\nu\sigma_\nu e^{-\langle\tau_\nu\rangle}\left(1-e^{-\langle\delta\tau_\nu\rangle}\right)(h_{\rm P}\nu - h_{\rm P}\nu_{\rm th})\,{\rm d}\nu}{\int_{\nu_{\rm th}}^{\infty} N_\nu\sigma_\nu e^{-\langle\tau_\nu\rangle}\left(1-e^{-\langle\delta\tau_\nu\rangle}\right){\rm d}\nu}\right] \tag{2.14}$$

For a power law SED, this frequency integral can be solved analytically, and yields a function that depends on the optical depth between the source and the current cell $\langle\tau_\nu\rangle$ and optical depth of the cell $\langle\delta\tau_\nu\rangle$. This function is evaluated at each time step and the resulting change in the temperature added to each cell. We ignore the heating caused by the He II ionizing background $\Gamma^{\rm bkg}_{\rm HeII}$, since this is accounted for via the photoionization heating in the hydrodynamical simulations (and it does not depend on the normalization of the photoionizing background, which we freely adjust). We also do not include cooling in our simulations because the gas cooling time at mean density is comparable to the Hubble time which is much longer than the expected lifetime of the quasar (i.e., $t_{\rm cool} \gg t_{\rm Q}$) and thus can be safely ignored. The more detailed description of heating mechanism implemented in our radiative transfer algorithm is given in Section 5.1.

2.2.4 Finite Speed of Light

Our code works in the infinite speed of light limit, similar to other one-dimensional radiative transfer codes which attempt to model observations along the line-of-sight (White et al. 2003; Bolton & Haehnelt 2007a; Lidz et al. 2007; Davies et al. 2014). Thus, the results do not depend on the speed of light, which may seem problematic because the light travel times across the proximity region can be tens of Myr. However, in Appendix A, we show that because absorption observations also occur along the light-cone, the infinite speed of light assumption exactly describes the ionization state of the gas probed by line-of-sight observations.

2.2.5 Recombinations

We use the Case A recombination coefficient throughout the work. Quasar proximity zones represent highly ionized media which typically have $x_{\rm HeII} \lesssim 10^{-2}$, making most cells optically thin to ionizing photons produced by recombinations directly to the ground state. This recombination radiation is an additional source of ionizations, but we do not include it in our computations. We show in Appendix C that neglecting secondary ionizations from recombination radiation is justified as it is negligible in comparison to the quasar radiation.

2.2.6 AN EXAMPLE RADIATIVE TRANSFER OUTPUT

We calculate He II spectra along each of the sightlines taken from the SPH simulations following the procedure described in Theuns et al. (1998), which we outline in Appendix D. Figure 2.1 shows various physical properties along an example line-of-sight. The quasar is located on the right side of the plot at $R = 0$. These physical properties are drawn from a model that has the quasar lifetime set to $t_{\rm Q} = 10$ Myr, the photon production rate $Q_{\rm 4Ry} = 10^{56.1}$ s^{-1}, and the He II ionizing background $\Gamma^{\rm bkg}_{\rm HeII} = 10^{-14.9}$s^{-1}, which is our preferred value at $z = 3.1$ following the discussion in § 3.1.

The uppermost panel of Figure 2.1 shows the gas density along the skewer in units of the cosmic mean density, illustrating the level of density fluctuations present in the $z = 3.1$ IGM. The second panel shows the H I transmitted flux, which exhibits the familiar absorption signatures characteristic of the Lyα forest. A weak H I proximity effect (Carswell et al. 1982; Bajtlik et al. 1988) is noticeable by eye near the quasar for $R \lesssim 20$ cMpc. This weak H I proximity effect is expected: given the high value of the H I ionizing background, the region where the quasar radiation dominates over the background is relatively small. Furthermore, the low H I Lyα optical depth at $z = 3.1$ reduces the contrast between the proximity zone and regions far from the quasar. On the contrary, the He II transmission clearly indicates the large and prominent ($\simeq 50$ cMpc) He II proximity zone around the quasar. At larger distances $R > 50$ cMpc the transmission drops to nearly zero, giving rise to long troughs of Gunn-Peterson (GP; Gunn & Peterson 1965) absorption, as is commonly observed in the He II transmission spectra of quasars observed with HST (Worseck et al. 2011; Syphers & Shull 2014). This GP absorption results from the large He II optical depth in the ambient IGM, which is in turn set by our choice of $\Gamma^{\rm bkg}_{\rm HeII} = 10^{-14.9}$s^{-1}. The He II transmission follows the radial trend set by the He II fraction $x_{\rm HeII}$. As expected, close to the quasar $R \lesssim 20$ cMpc, helium is highly ionized ($x_{\rm HeII} < 10^{-3}$) by the intense quasar radiation. At larger radii the quasar photoionization rate weakens, dropping approximately as R^{-2}, as indicated in the bottom panel. Eventually, at large distances $R \gtrsim 70$ cMpc the quasar radiation no longer dominates over the the background $\Gamma^{\rm bkg}_{\rm HeII}$, and $x_{\rm HeII}$ gradually asymptotes to a value $x_{\rm HeII,0} \simeq 10^{-2}$, set by the chosen He II ionizing background.

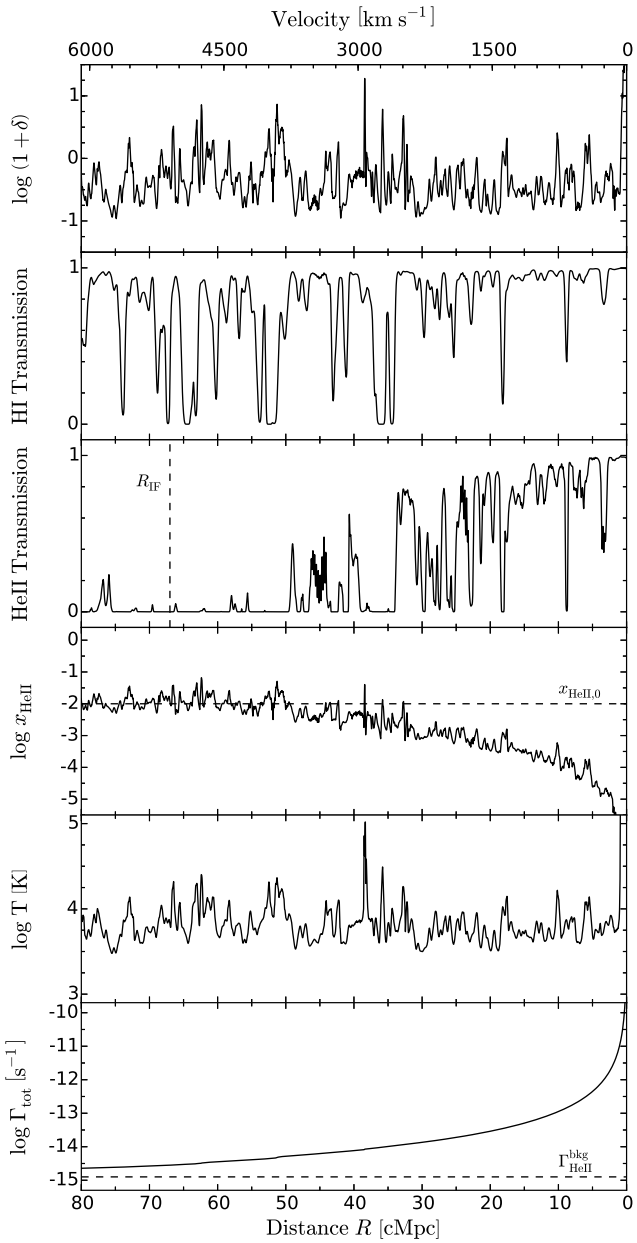

FIGURE 2.1: *Example sightline at $z = 3.1$ from our radiative transfer code assuming a quasar has been on for $t_{\rm Q} = 10^7$yr at a photon production rate $Q_{\rm 4Ry} = 10^{56.1}$ s^{-1} with He II ionizing background $\Gamma^{\rm bkg}_{\rm HeII} = 10^{-14.9}$s^{-1}. The lower x-axis indicates distance R from the quasar in units of comoving Mpc, whereas the upper x-axis is the corresponding velocity in units of* km s^{-1}. *Panels show (from top to bottom): the overdensity, transmitted flux in hydrogen, transmitted flux in helium, the He II fraction $x_{\rm HeII}$, temperature T, photoionization rate $\Gamma_{\rm tot}$. The vertical dashed line in the panel with He II transmission shows the extent of the quasar ionization front (see § 3.2 for the description). We indicate the initial He II fraction before the quasar is on by the dashed line in the panel with $x_{\rm HeII}$ evolution. The dashed line in the bottom panel indicates the value of the He II ionizing background $\Gamma^{\rm bkg}_{\rm HeII}$.*

Chapter 3

A new way of thinking about the proximity zones

"A method is more important than a discovery, since the right method will lead to new and even more important discoveries."
Lev Landau

The transmitted flux in the proximity zone results from an interplay between different parameters. In order to constrain the quasar lifetime, $t_{\rm Q}$, independently from other parameters, such as the He II ionizing background $\Gamma^{\rm bkg}_{\rm HeII}$ or the rate at which He II ionizing photons are emitted by the quasar $Q_{\rm 4Ry}$, we need to understand the impact of each one of them on the structure of the proximity zone. We begin first by considering the constraints on $\Gamma^{\rm bkg}_{\rm HeII}$ from observational data. We then introduce a new way of thinking about the He II proximity zones in terms of the time-evolution of the He II fraction, which incorporates the dependencies on quasar lifetime, quasar photon production rate and He II ionizing background. We present a simple analytical formula describing such dependencies and the most important physical process: the approach of the helium gas in the intergalactic medium around the quasar to the equilibrium with enhanced radiation field due to the quasar turning on, which is given by the equilibration time $t_{\rm eq}$ (see eqn. (2.7)).

3.1 OBSERVATIONAL CONSTRAINTS ON THE HE II IONIZING BACKGROUND $\Gamma^{\rm bkg}_{\rm HeII}$

In order to model the He II proximity regions, we need to make some assumptions about the background radiation field in the IGM. At $z \gtrsim 2.8$ this background may not be spatially uniform, as it has been argued that He II reionization is occurring (McQuinn 2009b; Shull et al. 2010). He II reionization is thought to be driven by quasars turning on and emitting the hard photons required to doubly ionize helium (Madau & Meiksin 1994; Miralda-Escudé et al. 2000; McQuinn et al. 2009a; Haardt & Madau 2012; Compostella et al. 2013). At $z = 3.1$, redshifts characteristic of much of the HST/COS data, the IGM is still likely to consist of mostly reionized He III regions, but there may be some quasars that turn on in He II regions. The latter case should become increasingly more likely with increasing redshift. In this work we model the full range of possibilities, but let us first get a sense for what currently available data implies about typical regions of the IGM.

Recent measurements of the He II effective optical depth $\tau_{\rm eff}$ from Worseck et al. (2014) & Worseck et al. in prep, albeit with large scatter, imply $\langle\tau^{\rm HeII}_{\rm eff}\rangle \simeq 4-5$ on scales $\Delta z = 0.04$ ($\Delta R \simeq 40$ cMpc) at $z \sim 3.1$ (see the upper panel of Figure 3.1). We use our 1D radiative transfer algorithm to try to understand how these observational results constrain the He II ionizing background $\Gamma^{\rm bkg}_{\rm HeII}$. Similarly to Worseck et al. (2014), we exclude the proximity zone from our calculations by turning the quasar off. The resulting transmission through the IGM is solely due to the He II background $\Gamma^{\rm bkg}_{\rm HeII}$. We then vary $\Gamma^{\rm bkg}_{\rm HeII}$, and calculate the effective optical depth defined by $\tau_{\rm eff} \equiv -\ln\langle F\rangle$, where we take the average of the simulated transmission F in 5 regions along 100 skewers, each region with size $\Delta z = 0.04$ equal to the size of the bin in the observations. We also calculate the average value of the He II fraction $\langle x_{\rm HeII}\rangle$ in the same bins.

The results are shown in Figure 3.1. The solid red line in the middle panel shows the values of our modeled He II effective optical depth as a function of the He II ionizing background $\Gamma^{\rm bkg}_{\rm HeII}$. The corresponding He II fraction $\langle x_{\rm HeII}\rangle$ is shown in the bottom panel of Figure 3.1. We find that the effective optical depth $\tau_{\rm eff} \simeq 4-5$ implies a characteristic He II ionizing background of $\Gamma^{\rm bkg}_{\rm HeII} \simeq 10^{-14.9}{\rm s}^{-1}$, which will refer to henceforth as our fiducial value for $z = 3.1$. This He II background corresponds to an average He II fraction $\langle x_{\rm HeII}\rangle \simeq 0.02$. Note that our ability to constrain the average He II fraction to be $x_{\rm HeII} \sim 10^{-2}$ contrasts sharply with the case of H I GP absorption at $z \sim 6-7$. For hydrogen at these much higher redshifts the most sensitive measurements imply a lower limit on the H I fraction $x_{\rm HI} \gtrsim 10^{-4}$ (Fan et al. 2002, 2006b). This difference in sensitivity between He II Lyα at $z \sim 3$ and H I

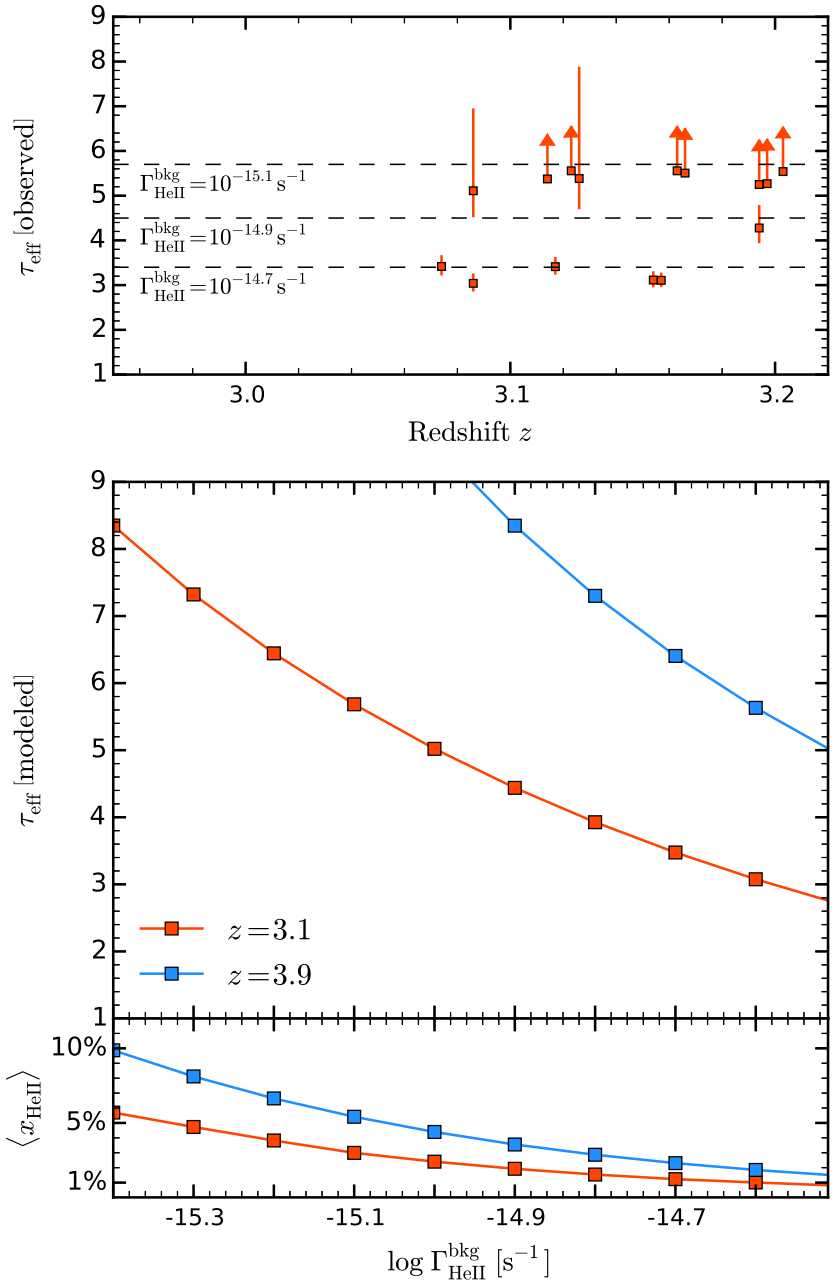

FIGURE 3.1: *Results of the radiative transfer simulations with just a uniform He II ionizing background and no quasar source. The red curve corresponds to the calculations performed at redshift* $z = 3.1$*, while the blue curve is for* $z = 3.9$*.* Top panel: *the observed distribution of the He II effective optical depth at* $z = 3.0 - 3.2$ *from Worseck et al. (2014) & Worseck et al. in prep. The dashed curves show the mean effective optical depths on the same spatial scale as data* ($\Delta z = 0.04$) *corresponding to the indicated* $\Gamma^{\rm bkg}_{\rm HeII}$ *value in the* 1*D radiative transfer simulations.* Middle panel*: He II effective optical depth* $\tau_{\rm eff}$ *as a function of the He II ionizing background field* $\Gamma^{\rm bkg}_{\rm HeII}$ *from our* 1*D radiative transfer algorithm.* Bottom panel*: He II fraction* $x_{\rm HeII}$ *as a function of He II background* $\Gamma^{\rm bkg}_{\rm HeII}$*.*

Lyα at $z \sim 6$ results from several factors: 1) the He II Lyα GP optical depth is 4 times smaller than H I Lyα due to the higher frequency of He II; 2) the abundance of helium is a factor of ~ 12 smaller than that of hydrogen 3) the intergalactic medium is on average a factor of 5.4 less dense at $z \sim 3$ compared to $z \sim 6$, but also the cosmological line element is 2.3 times larger at $z \sim 6$ than at $z \sim 3$. All of these factors combined together therefore imply an increase of two orders of magnitude in the sensitivity of the He II GP optical depth at $z \sim 3$ to the He II fraction and hence the He II ionizing background.

While uniformity is likely not a good assumption during He II reionization, which makes the above number highly approximate (and probably an underestimate for $x_{\rm HeII}$), it is a good assumption thereafter, i.e. $z \simeq 2.5$, where fluctuations of He II ionizing background are on the order of unity (McQuinn & Worseck 2014).

We also preformed the same set of calculations at higher redshift of $z = 3.9$ and plot the results as blue curves in Figure 3.1. Note, that at higher redshifts the gas in the intergalactic medium is becoming more dense, and the steep redshift dependence of the GP optical depth $\tau_{\rm GP} \propto (1+z)^{3/2}$ gives rise to significantly higher optical depths at $z = 3.9$. Thus at these high redshifts even He II fractions of $x_{\rm HeII} \sim 0.01$ give rise to large effective optical depths $\tau_{\rm eff} \gtrsim 5$. While we mostly consider $z = 3.1$, § 4.5.1 considers $z \simeq 3.9$.

3.2 Time-evolution of the He II fraction

Consider the case of a quasar emitting radiation for time $t_{\rm Q}$ into a homogeneous IGM with He II fraction $x_{\rm HeII}$. The time evolution of the He III ionization front is governed by the equation (Haiman & Cen 2001; Bolton & Haehnelt 2007a)

$$\frac{dR_{\rm IF}}{dt} = \frac{Q_{\rm 4Ry} - \frac{4}{3}R_{\rm IF}^3 \alpha_{\rm HeIII} n_{\rm He}^2}{4\pi R_{\rm IF}^2 x_{\rm HeII} n_{\rm He}}, \tag{3.1}$$

which has the solution

$$R_{\rm IF} = R_S \left[1 - \exp\left(-\frac{t_{\rm Q}}{x_{\rm HeII} t_{\rm rec}}\right)\right]^{1/3}, \tag{3.2}$$

where $t_{\rm rec} = 1/n_{\rm e}\alpha_{\rm A}$ is the recombination timescale and $R_{\rm S}$ is the classical Strömgren radius $R_{\rm S} = \left(\frac{3Q_{\rm 4Ry}}{4\pi\alpha_{\rm A} n_{\rm HeIII} n_{\rm e}}\right)^{1/3}$, which is the radius of the sphere around a source of radiation, within which ionizations are exactly balanced by recombinations.

Previous observational studies of the H I Lyα proximity zones around $z \simeq 6$ quasars have primarily focused on measuring proximity zone sizes (Cen & Haiman 2000;

Madau & Rees 2000; Mesinger & Haiman 2004; Fan et al. 2006b; Carilli et al. 2010), guided by the faulty intuition that, for assuming a highly neutral IGM $x_{\rm HI} \sim 1$, the location where the transmission profile goes to zero can be identified with the location of the ionization front $R_{\rm IF}$ in eqn. (3.2). However, the transmission profile for a H II region expanding into a significantly neutral IGM can be difficult to distinguish from that of a "classical" proximity zone embedded in an already highly ionized IGM (Bolton & Haehnelt 2007b; Maselli et al. 2007; Lidz et al. 2007). This degenerate situation arises, because even very small residual neutral fractions in the proximity zone $x_{\rm HI} \gtrsim 10^{-5}$ are sufficient to saturate H I Lyα, which may occur well before the location of the ionization front is reached (Bolton & Haehnelt 2007a). Thus, naively identifying the size of the proximity zone with the location of the ionization front $R_{\rm IF}$, can lead to erroneous conclusions about the parameters governing eqn. (3.2), e.g. the quasar lifetime and the ionization state of the IGM.

A similar degeneracy also exists for He II proximity zones, which is exemplified in Figure 2.1 where the He II transmission saturates at $R \simeq 50$ cMpc, whereas the ionization front is located much further from the quasar $R_{\rm IF} \simeq 67$ cMpc (dashed vertical line). However, all previous work analyzing the structure of He II proximity zones has been based on the assumption that the edge of the observed proximity zone can be identified with $R_{\rm IF}$ (Hogan et al. 1997; Anderson et al. 1999; Syphers & Shull 2014; Zheng et al. 2015). In addition, the majority of studies have assumed that helium is completely singly ionized $x_{\rm HeII} = 1$ for quasars at $3.2 < z < 3.5$ (Hogan et al. 1997; Anderson et al. 1999; Zheng et al. 2015), whereas our discussion in the previous section (see Figure 3.1) indicates that at $z = 3.1$ observations of the effective optical depth suggest that $\Gamma^{\rm bkg}_{\rm HeII} = 10^{-14.9}{\rm s}^{-1}$ implying $x_{\rm HeII} \simeq 0.01$ (although the average $x_{\rm HeII}$ could be much larger if some regions are predominantly He II at $z > 2.8$, Compostella et al. 2013; Worseck et al. 2014). Hence, in many regions one is actually in the classical proximity zone regime, where radiation from the quasar increases the ionization level of nearby material which was already highly ionized to begin with and the location of the ionizaton front is irrelevant. Furthermore, as we describe below, the background level determines the equilibration timescale $t_{\rm eq} \approx 1/\Gamma^{\rm bkg}_{\rm HeII}$ (see eqn. 2.7), which is the characteristic time on which the He II ionization state of IGM gas responds to the changes in the radiation field. For our fiducial value of the background $\Gamma^{\rm bkg}_{\rm HeII} = 10^{-14.9}{\rm s}^{-1}$, $t_{\rm eq} \simeq 2.5 \times 10^7$ yr is comparable to the Salpeter time. This suggests that the approach of $x_{\rm HeII}$ to equilibrium is the most important physical effect in He II proximity zones, and in what follows we introduce a simple analytical equation for understanding this time evolution.

The full solution to the time evolution of $x_{\rm HeII}$ is given by eqn. (2.6), which involves a nontrivial integral because $\Gamma_{\rm tot}$, $n_{\rm e}$ and $\alpha_{\rm A}$ are all functions of time. Indeed, this is exactly the equation that is solved at every grid cell in our 1D radiative transfer

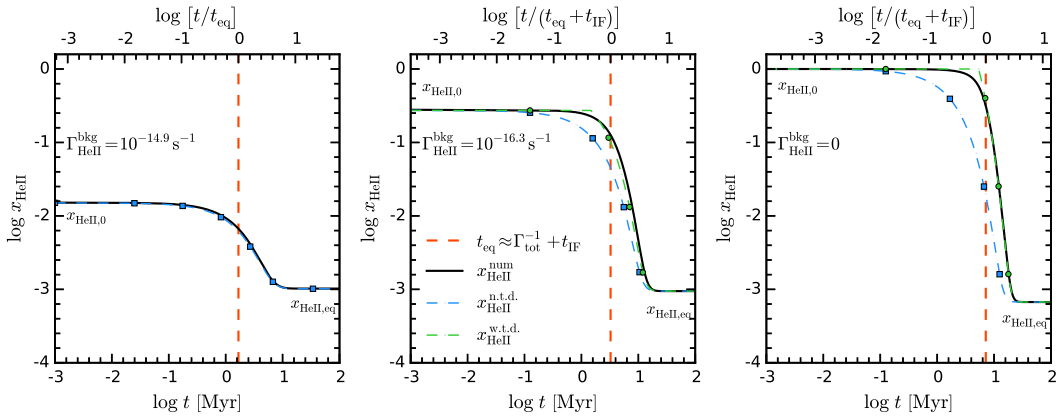

FIGURE 3.2: *Time evolution of the He II fraction, $x_{\rm HeII}\,(t, R)$, at a single location in the proximity zone at $R = 25$ cMpc, produced from our radiative transfer solution (solid black curve), compared to the analytical expression given by eqn. (3.3) (dashed blue curve with square markers).* The left panel *shows the results for a model with $\Gamma^{\rm bkg}_{\rm HeII} = 10^{-14.9}{\rm s}^{-1}$ ($x_{\rm HeII,0} \simeq 0.02$).* The middle panel *is the same, but for $\Gamma^{\rm bkg}_{\rm HeII} = 10^{-16.3}{\rm s}^{-1}$ ($x_{\rm HeII,0} \simeq 0.3$). The zero background model $\Gamma^{\rm bkg}_{\rm HeII} = 0$ (i.e., $x_{\rm HeII,0} = 1$) is shown in the* right panel. *The dashed green curves correspond to the corrected analytical solution given by eqn. (3.6). The He II fraction $x_{\rm HeII,eq}$ and the equilibration time $t_{\rm eq}$ (red dashed vertical line in all panels) are evaluated using the quasar photoionization rate for a fully equilibrated IGM in the analytic expression.*

calculation, by integrating over infinitesimal timesteps (see eqn. 2.8). However, in the limit of a highly ionized IGM $x_{\rm HI} \ll 1$, $n_{\rm e} \propto (1+z)^3$ which is approximately constant over the quasar lifetimes we consider. Furthermore, as we will demonstrate later, the low singly ionized fraction $x_{\rm HeII} \ll 1$ implies that the attenuation is small in most of the proximity zone and, hence, the photoionization rate $\Gamma_{\rm tot}$ is also approximately constant in time. Similarly, $\alpha_{\rm A}$ varies only weakly with temperature (i.e., $\propto T^{-0.7}$), and given that the temperature will also not vary significantly with time if the HeII already has been reionized, $\alpha_{\rm A}$ can also be approximated as constant. In this regime where $\Gamma_{\rm tot}$, $n_{\rm e}$ and $\alpha_{\rm A}$ are constant in time, eqn. (2.8) reduces to the simpler expression evaluated at $t = t_{\rm Q}$, the quasar lifetime:

$$x_{\rm HeII}\,(t_{\rm Q}) = x_{\rm HeII,eq} + \left(x_{\rm HeII,0} - x_{\rm HeII,eq}\right) e^{-t_{\rm Q}/t_{\rm eq}}, \tag{3.3}$$

Given that the recombination timescale $t_{\rm rec} \equiv 1/\alpha_{\rm A} n_{\rm e} \simeq 10^9$ yr is very long compared to the longest ionization timescales $1/\Gamma^{\rm bkg}_{\rm HeII}$, we can write $t_{\rm eq} \approx 1/\Gamma_{\rm tot}$, $x_{\rm HeII,0} \approx \alpha_{\rm A} n_{\rm e}/\Gamma^{\rm bkg}_{\rm HeII}$, and $x_{\rm HeII,eq} \approx \alpha_{\rm A} n_{\rm e} t_{\rm eq}$.

In the left panel of Figure 3.2, the solid black curve shows the time evolution of $x_{\rm HeII}\,(t, R)$ at a single location in the proximity zone $R = 25$ cMpc, produced from our radiative transfer solution for the quasar photon production rate $Q_{\rm 4Ry} = 10^{56.1}{\rm s}^{-1}$

and finite background case $\Gamma^{\rm bkg}_{\rm HeII} = 10^{-14.9}{\rm s}^{-1}$ corresponding to an initial He II fraction $x_{\rm HeII,0} = 0.02$. The dashed blue curve is the analytical solution eqn. (3.3). where $x_{\rm HeII,eq}$ and $t_{\rm eq}$ have been evaluated from the code outputs, using the total photoionization rate $\Gamma_{\rm tot}$ for a fully equilibrated IGM. In other words, we evaluate $\Gamma_{\rm tot}(t = \infty) = \Gamma_{\rm QSO}(t = \infty) + \Gamma^{\rm bkg}_{\rm HeII}$ where $t = \infty$ is taken to be our last output at $t = 100\,{\rm Myr}$. It is clear that for the case $\Gamma^{\rm bkg}_{\rm HeII} = 10^{-14.9}{\rm s}^{-1}$ and thus an initially highly ionized IGM $x_{\rm HeII} \simeq 10^{-2}$, eqn. (3.3) provides an excellent match to the result of the full radiative transfer calculation.

Due to the patchy and inhomogeneous nature of He II reionization some regions on the IGM might, however, have a very high He II fraction. Therefore, it is important to check if our analytical approximation also holds in this case. The middle and right panels of Figure 3.2 show the time evolution of the He II fraction at the same location and value of $Q_{\rm 4Ry}$, but now for $\Gamma^{\rm bkg}_{\rm HeII} = 10^{-16.3}{\rm s}^{-1}$ and $\Gamma^{\rm bkg}_{\rm HeII} = 0$, which correspond to $x_{\rm HeII,0} \simeq 0.3$ and $x_{\rm HeII,0} = 1$ respectively. The analytical approximation (blue squares and curve) clearly fails to reproduce the time evolution. Specifically, it predicts too rapid a response to the quasar ionization relative to the true evolution, and this discrepancy is largest for $\Gamma^{\rm bkg}_{\rm HeII} = 0$ where the true evolution to equilibrium is delayed by ~ 5.5 Myr.

Recall that, because we observe on the light cone, the speed of light is effectively infinite in our code. Thus, at the location $R = 25$ cMpc we expect no delay in the response of the proximity zone to the quasar radiation caused by finite light travel time effects. For the $x_{\rm HeII,0} \simeq 0.02$ ($\Gamma^{\rm bkg}_{\rm HeII} = 10^{-14.9}{\rm s}^{-1}$) case the ionization front travels at nearly the speed of light and, because we observe on the light cone, there is thus no noticeable delay between the evolution of the He II fraction and eqn. (3.3). However, if the ionization front does not travel at the speed of light, which will be the case for the lower backgrounds $\Gamma^{\rm bkg}_{\rm HeII} = 10^{-16.3}{\rm s}^{-1}$ and $\Gamma^{\rm bkg}_{\rm HeII} = 0$ and correspondingly higher He II fractions ($x_{\rm HeII,0} \simeq 0.3$ and $x_{\rm HeII,0} = 1$), then the time that it takes the ionization front to propagate to the location $R = 25$ cMpc is no longer negligible relative to the equilibration timescale, and the response of the He II fraction will be delayed.

We can estimate this time delay by noting that the location of the ionization front (see eqn. 3.2) is given by

$$R_{\rm IF} \approx \left[\frac{3Q_{\rm 4Ry}t_{\rm IF}}{4\pi n_{\rm He}x_{\rm HeII}}\right]^{1/3}, \tag{3.4}$$

assuming that $t_{\rm Q} \ll x_{\rm HeII}t_{\rm rec} = (x_{\rm HeII}/1.0)1.16 \times 10^9\,{\rm yr}$, valid for $x_{\rm HeII} \sim 0.3 - 1.0$ and the quasar lifetimes we consider. In this regime the ionization front is simply the radius of the ionized volume around the quasar. Inverting this equation, we obtain that at a location R, the time delay between the quasar turning on and the arrival of

the first ionizing photons is[1]

$$t_{\rm IF}\left(R\right) = 6.7\,\left(\frac{x_{\rm HeII}}{1.0}\right)\left(\frac{Q_{\rm 4Ry}}{10^{56}\ {\rm s}^{-1}}\right)^{-1}\left(\frac{R}{25\ {\rm cMpc}}\right)^{3}\ {\rm Myr} \tag{3.5}$$

For $R = 25$ cMpc this delay is very nearly the delay seen in the middle and right panels of Figure 3.2, suggesting a simple physical interpretation for the behavior of the He II fraction in the proximity zone for the $\Gamma^{\rm bkg}_{\rm HeII} = 10^{-16.3}{\rm s}^{-1}$ and $\Gamma^{\rm bkg}_{\rm HeII} = 0$ cases. Namely, eqn. (3.3) still describes the equilibration of the He II fraction, but it must be modified to account for the delay in the arrival of the ionization front, only after which equilibration begins to occur. We thus write

$$x_{\rm HeII}\left(t_Q, r\right) = x_{\rm HeII,eq} + \left(1 - x_{\rm HeII,eq}\right){\rm e}^{\frac{-\left(t_{\rm Q} - t_{\rm IF}\right)}{t_{\rm eq}}} \tag{3.6}$$

The green curves in the middle and right panels of Figure 3.2 illustrate that the simple equilibration time picture, but now modified to account for a delay in the arrival of the ionization front, provides a good description of the time evolution of $x_{\rm HeII}$ in the proximity zone for $\Gamma^{\rm bkg}_{\rm HeII} = 10^{-16.3}{\rm s}^{-1}$ and $\Gamma^{\rm bkg}_{\rm HeII} = 0$ cases.

To summarize, we have shown that the He II fraction in quasar proximity zones is governed by a simple analytical equation (eqn. 3.3), which describes the exponential time evolution from an initial pre-quasar ionization state $x_{\rm HeII,0}$ set by the He II ionizing background $\Gamma^{\rm bkg}_{\rm HeII}$ to an equilibrium value $x_{\rm HeII,eq}$. The enhanced photoionization rate near the quasar $\Gamma_{\rm tot}$ sets both the timescale of the exponential evolution $t_{\rm eq} = 1/\Gamma_{\rm tot}$, and the equilibrium value attained $x_{\rm HeII,eq} \approx \alpha_{\rm A} n_{\rm e} t_{\rm eq}$. For very high He II fractions $x_{\rm HeII,0} \simeq 1$, this exponential equilibration is delayed by the time it takes the sub-luminal ionization front to arrive to a given location.

3.3 Degeneracy between the He II background and the lifetime of quasars

Previous work on H I proximity zones at $z \sim 6$ have pointed out that the quasar lifetime and ionization state of the IGM (or equivalently the ionizing background) are degenerate in determining the location of the ionization front $R_{\rm IF}$ (Bolton & Haehnelt 2007a,b; Lidz et al. 2007; Bolton et al. 2012), which is readily apparent from the exponent in eqn. (3.2). Although, many studies simply assume a fixed value for the quasar lifetime of $t_Q = 10^7$ yr when making inferences about the ionization state

[1]The mean number density of helium $n_{\rm He}$ is calculated assuming an average overdensity $1+\delta \simeq 0.7$, similar to the value used in the radiative transfer solution for chosen skewer.

of the IGM (but see Bolton et al. 2012 for a more careful treatment). This degeneracy between lifetime and ionizing background is complicated by the fact that, at $z \sim 6$ only lower limits on the hydrogen neutral fraction $x_{\rm HI}$ (upper limits on the background photoionization rate $\Gamma^{\rm bkg}_{\rm HI}$) can be obtained from lower limits on the GP absorption optical depth. The situation is further exacerbated if there are significant spatial fluctuations in the background caused by foreground galaxies that may have 'pre-ionized' the IGM (Lidz et al. 2007; Bolton & Haehnelt 2007b; Wyithe et al. 2008).

An analogous degeneracy exists between $t_{\rm Q}$ and $x_{\rm HeII}$ for He II proximity zones, as we illustrate in Figure 3.3. The upper panel shows three example transmission spectra for the same skewer and value of He II background, but different values of quasar lifetime, which are clearly distinguishable. The situation changes if we also allow the He II background to vary, which is shown in the bottom panel of Figure 3.3 where transmission spectra are plotted for the same skewer, but several distinct combinations of lifetime and background. The nearly identical resulting spectra indicate that the same degeneracy exists at $z \simeq 3.1$ between the quasar lifetime $t_{\rm Q}$ and the value of the He II ionizing background $\Gamma^{\rm bkg}_{\rm HeII}$. In what follows, we discuss this degeneracy in detail, aided by our analytical model for the time evolution of the He II fraction from the previous section.

We can understand this degeneracy by rearranging eqn. (3.3)

$$x_{\rm HeII}\left(t_{\rm Q}, R\right) = x_{\rm HeII,eq}\left[1 + \frac{\Gamma_{\rm QSO}}{\Gamma^{\rm bkg}_{\rm HeII}} {\rm e}^{-\frac{t_{\rm Q}}{t_{\rm eq}(R)}}\right] \tag{3.7}$$

where for simplicity we have focused on the finite background case where the ionization front time delay can be ignored. There are two regimes that are relevant to this degeneracy. First, very near the quasar the attenuation of $\Gamma_{\rm QSO}$ is negligible, implying that $t_{\rm eq} \propto \Gamma^{-1}_{\rm QSO} \propto R^2$ and given by

$$t_{\rm eq} = 0.08 \left(\frac{Q_{\rm 4Ry}}{10^{56}\ {\rm s}^{-1}}\right)^{-1} \left(\frac{R}{5\ {\rm cMpc}}\right)^{2}\ {\rm Myr}. \tag{3.8}$$

At small distances ($R \lesssim 15$ cMpc in Fig. 3.3) in the highly ionized 'core' of the proximity zone, $t_{\rm eq} \ll t_{\rm Q}$ for the quasar lifetimes we consider, and eqn. (3.7) indicates that the proximity zone structure depends only on the luminosity of the quasar, which determines $x_{\rm HeII,eq} \approx \alpha_{\rm A} n_{\rm e}/\Gamma_{\rm QSO}$, but there is no sensitivity to either $t_{\rm Q}$ or $\Gamma^{\rm bkg}_{\rm HeII}$.

Second, at larger distances the equilibration time grows as $t_{\rm eq} \propto R^2$ and will eventually be comparable to the quasar lifetime. We define the equilbration distance $R_{\rm eq}$ to be the location where $t_{\rm eq}(R_{\rm eq}) \equiv t_{\rm Q}$, which gives

$$R_{\rm eq} = 17 \left(\frac{Q_{\rm 4Ry}}{10^{56}\ {\rm s}^{-1}}\right)^{1/2} \left(\frac{t_{\rm Q}}{1\ {\rm Myr}}\right)^{1/2}\ {\rm cMpc}, \tag{3.9}$$

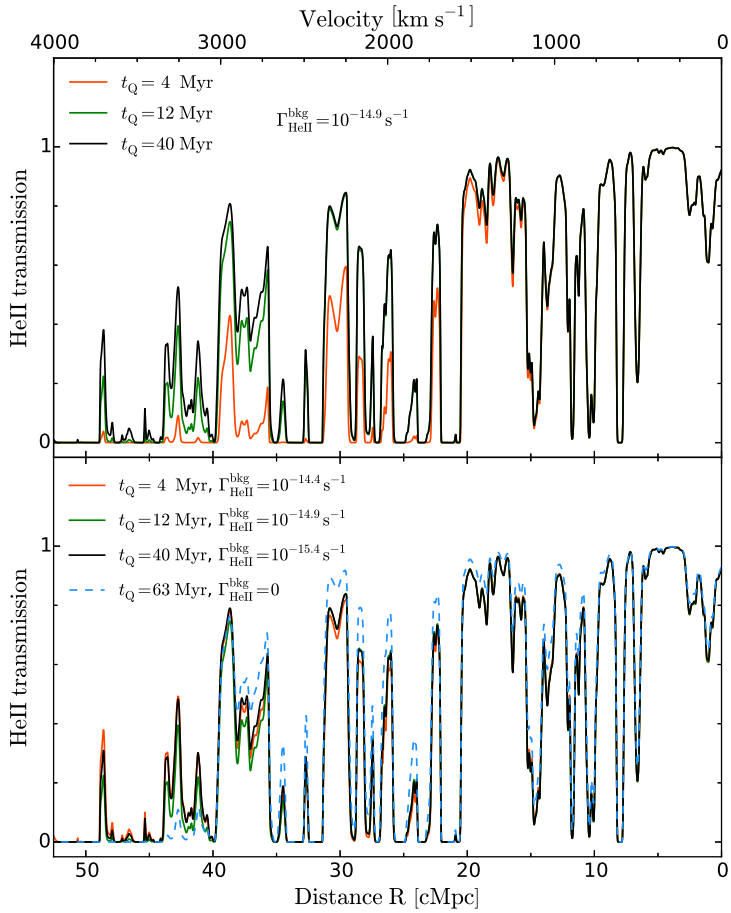

FIGURE 3.3: *Illustration of the partial degeneracy between the He II ionizing background and the quasar lifetime for the specified values of* Γ^{bkg}_{HeII} *and* t_Q. The upper panel *shows three models with* $t_Q = 4$ *Myr (red),* $t_Q = 12$ *Myr (green) and* $t_Q = 40$ *Myr (black) with He II background fixed to our fiducial value* $\Gamma^{bkg}_{HeII} = 10^{-14.9}s^{-1}$. The bottom panel *shows four models with the same values of quasar lifetime as before, but with different He II backgrounds. The red curve corresponds to* $t_Q = 4$ *Myr and* $\Gamma^{bkg}_{HeII} = 10^{-14.4}s^{-1}$, *whereas the solid black curve corresponds to* $t_Q = 40$ *Myr and* $\Gamma^{bkg}_{HeII} = 10^{-15.4}s^{-1}$. *The model with* $t_Q = 12$ *Myr and* $\Gamma^{bkg}_{HeII} = 10^{-14.9}s^{-1}$ *is shown by the green curve, and the dashed blue curve shows a* $\Gamma^{bkg}_{HeII} = 0$ *model with* $t_Q = 63$ *Myr. The photon production rate is* $Q_{4Ryd} = 10^{56.1}s^{-1}$ *for all models.*

where for simplicity we neglect the impact of attenuation of Γ_{QSO}. At distances comparable to the equilibration distance $R \sim R_{eq}$, eqn. (3.7) indicates that the He II fraction will be sensitive to t_Q. Note that at $R \sim R_{eq}$ the quasar still dominates over the background $\Gamma_{QSO} \gg \Gamma^{bkg}_{HeII}$, such that $x_{HeII,eq}$ is still independent of Γ^{bkg}_{HeII}. One then sees from eqn. (3.7) that for any change in quasar lifetime t_Q one can always make a

corresponding change to the value of $\Gamma^{\rm bkg}_{\rm HeII}$ to yield the same value of $x_{\rm HeII}$. But note that this degeneracy holds only at a single radius R, because $t_{\rm eq}\,(R)$ is a function of R, whereas our $\Gamma^{\rm bkg}_{\rm HeII}$ is assumed to be spatially constant. Therefore, there is no way to choose a constant $\Gamma^{\rm bkg}_{\rm HeII}$ such that the $x_{\rm HeII}\,(t_{\rm Q}, R)$ matches different values of $t_{\rm Q}$ at all R. In reality, $\Gamma^{\rm bkg}_{\rm HeII}$ will fluctuate spatially, but it will not have the required dependence on R to counteract the lifetime dependence.

Similar arguments also apply when $\Gamma^{\rm bkg}_{\rm HeII} = 0$, and the $x_{\rm HeII}(t, R)$ evolution is governed by eqn. (3.6). In this case, the time evolution depends only on the quasar lifetime $t_{\rm Q}$ and the ionizing photon production rate of the quasar $Q_{\rm 4Ry}$. Very close to the quasar ($R \lesssim 15$ cMpc), there is no sensitivity to quasar lifetime provided that $t_{\rm Q} - t_{\rm IF}(R) \gg t_{\rm eq}$, which is the case for the long quasar lifetime model $t_{\rm Q} = 63$ Myr shown in Figure 3.3 with $\Gamma^{\rm bkg}_{\rm HeII} = 0$ (dashed blue curve), which is indistinguishable from the finite background models at small radii. Although note that for much shorter quasar lifetimes $t_{\rm Q} \sim t_{\rm IF}\,(R)$ comparable to the ionization front travel time, eqn. (3.6) indicates one may retain sensitivity to the quasar lifetime even in the core of the zone. At larger distances $R \gtrsim 15\,$Mpc where $t_{\rm Q} - t_{\rm IF}\,(R) \sim t_{\rm eq}$, the $\Gamma^{\rm bkg}_{\rm HeII} = 0$ case becomes sensitive to quasar lifetime according to eqn. (3.6), but Figure 3.3 still indicates that the transmission profile is remarkably similar to the finite background case. In principle $Q_{\rm 4Ry}$ could be varied to produce a curve that appears even more degenerate, but we do not explore that here (but see the discussion in § 4.5.1).

Finally, an obvious difference between the $\Gamma^{\rm bkg}_{\rm HeII} = 0$ and finite background case is of course the transmission level far from the quasar, which is zero for $\Gamma^{\rm bkg}_{\rm HeII} = 0$, but corresponds to a finite value of $\tau_{\rm eff}$ for $\Gamma^{\rm bkg}_{\rm HeII} \neq 0$ (see Figure 3.1). At low redshifts $z \simeq 3$ where the effective optical depth can be measured, this provides an independent constraint on $\Gamma^{\rm bkg}_{\rm HeII}$ which rules out a $\Gamma^{\rm bkg}_{\rm HeII} = 0$ model. As discussed in § 3.1, the enhanced sensitivity of $\tau_{\rm eff}$ measurements to the He II background level for He II GP absorption at $z \sim 3$, as compared to H I GP absorption at $z \sim 6-7$ (where only upper limits on the background are available), constitutes an important difference between He II and H I proximity zones, which can be leveraged to break the degeneracy between the quasar lifetime $t_{\rm Q}$ and He II ionizing background $\Gamma^{\rm bkg}_{\rm HeII}$, as we will elaborate on in the next section.

3.4 SUMMARY

We have shown that observations of the He II effective optical depth at $z \simeq 3.1$ suggest the characteristic He II ionizing background $\Gamma^{\rm bkg}_{\rm HeII} = 10^{-14.9}{\rm s}^{-1}$ and hence indicate that Helium is highly doubly ionized in He III regions $x_{\rm HeII} \simeq 0.02$ at this

redshift. Thus He II proximity zones are more likely to be in a regime where radiation from the quasar increases the ionization level of nearby material which was already highly ionized before quasar activity. In this regime the location of the ionizaton front, that was used in previous work analyzing the structure of He II proximity zones, is irrelevant.

We have introduced a new and more appropriate way of thinking about proximity zones in terms of the time-evolution of the He II fraction and its approach to equilibrium, which governs both the case of a quasar turning on in an IGM for which Helium is singly ionized, as well as case where the IGM is already highly doubly ionized. We presented a simple analytical formula describing this time evolution, and showed that it agrees with the results of detailed radiative transfer calculations. We have also illustrated that at $z \simeq 3.1$ the degeneracy existing between the quasar lifetime and He II ionizing background can be broken, because the value of He II ionizing background is determined independently from the measurements of the He II effective optical depth.

Chapter 4

Properties of the stacked transmission profiles

"Never trust to general impressions, my boy,
but concentrate yourself upon details."
Sir Arthur Conan Doyle
(The Adventures of Sherlock Holmes)

Density fluctuations in the intergalactic medium around the quasar result in a significant variation in the proximity zone sizes for individual sightlines, which complicates our ability to constrain any parameters from quasar proximity regions. This effect is illustrated in Figure 4.1, where we show simulated transmission profiles for the same model with values of quasar lifetime $t_{\rm Q} = 10$ Myr, He II ionizing background of $\Gamma^{\rm bkg}_{\rm HeII} = 10^{-14.9}{\rm s}^{-1}$ and photon production rate of $Q_{\rm 4Ry} = 10^{56.1}{\rm s}^{-1}$, but for two skewers that have different underlying density fields. The bottom panel shows the case for the same quasar lifetime and photon production rate, but with the He II background set to zero. A nonzero background $\Gamma^{\rm bkg}_{\rm HeII}$ results in significantly more transmission far from the quasar, and concomitant sightline-to-sightline scatter, increasing the ambiguity in determining the edge of the He II proximity zone (see also discussion in Bolton & Haehnelt 2007a,b; Lidz et al. 2007).

One approach to mitigate the impact of these density fluctuations, is to average them down by stacking different He II proximity regions, using potentially all ~ 30 He II

Lyα forest sightlines observed to date (Worseck et al. 2011; Syphers et al. 2012). From the perspective of the modeling, this also helps to isolate the salient dependencies of the mean transmission profile on the model parameters. In this section we will analyze stacked He II Lyα profiles and study their dependence on the three parameters that govern the structure of the proximity zones: the quasar lifetime $t_{\rm Q}$, the He II ionizing background $\Gamma^{\rm bkg}_{\rm HeII}$, and the quasar photon production rate $Q_{\rm 4Ry}$.

In Figure 4.2 we show stacks of 1000 skewers for a sequence of proximity zone models with different quasar lifetimes in the range $t_{\rm Q} = 1 - 500$ Myr, indicated by the colored curves, but with other parameters ($\Gamma^{\rm bkg}_{\rm HeII}$ and $Q_{\rm 4Ry}$) fixed. The panels show, from top to bottom, the stacked transmission profiles in He II Lyα region, the He II

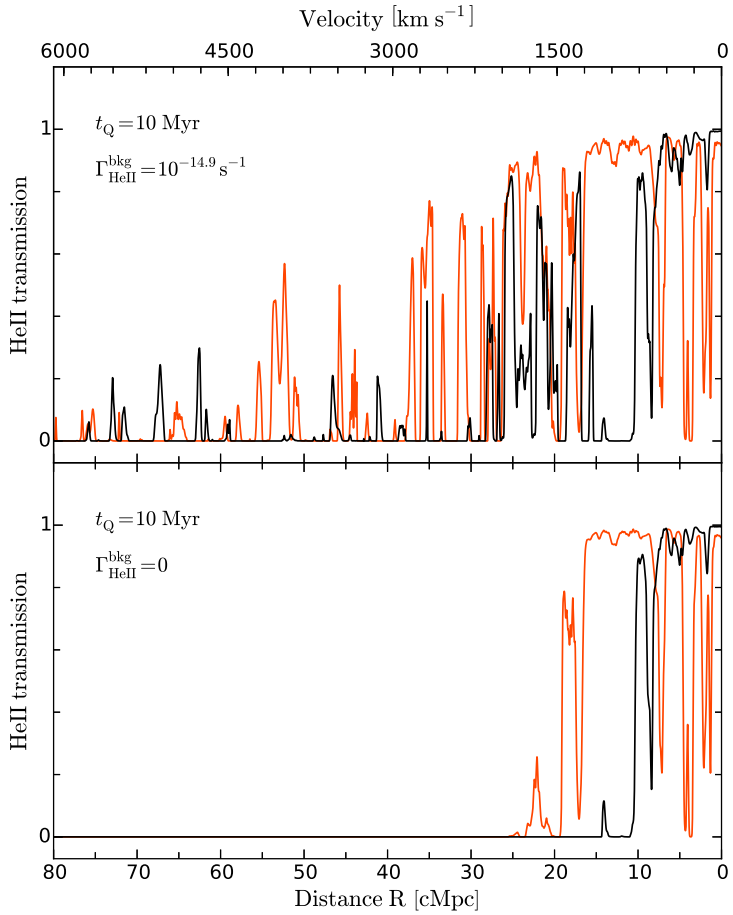

FIGURE 4.1: *He II proximity region for two different density skewers and the same model parameters (top panel:* $t_{\rm Q} = 10$ *Myr,* $\Gamma^{\rm bkg}_{\rm HeII} = 10^{-14.9}$s^{-1}*, bottom panel:* $t_{\rm Q} = 10$ *Myr,* $\Gamma^{\rm bkg}_{\rm HeII} = 0$*). Density fluctuations alter the proximity region profile even with other parameters fixed, acting as a source of uncertainty in our analysis.*

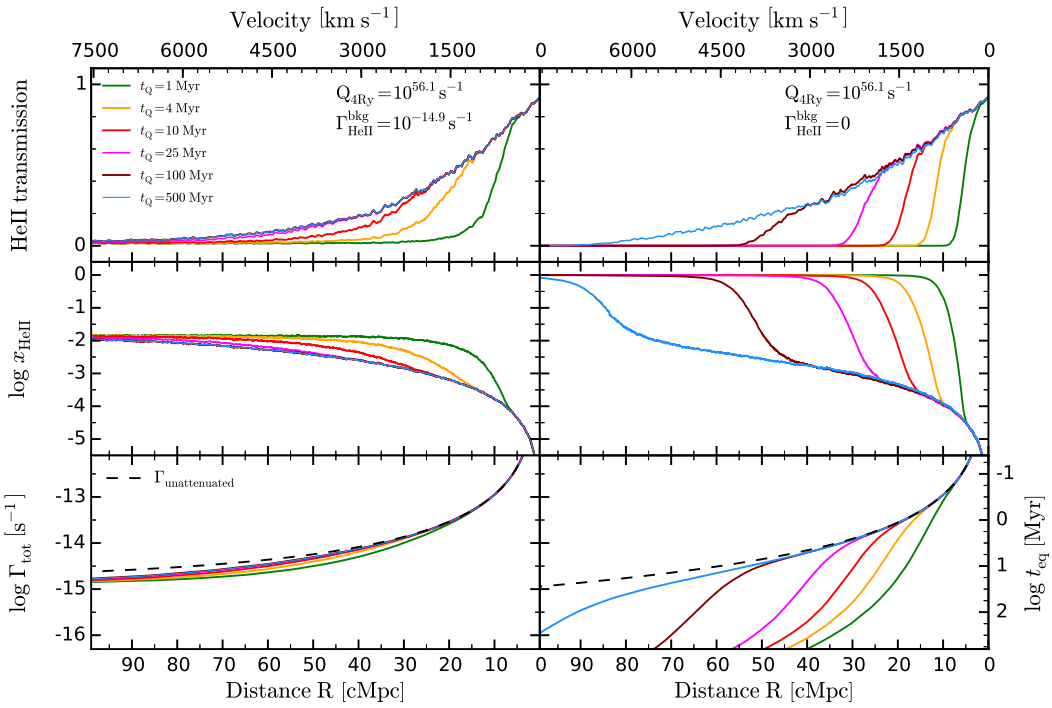

FIGURE 4.2: *Results of the radiative transfer simulations. Three panels show (from top to bottom): a) transmission profiles for different values of quasar lifetime and fixed values of* $\Gamma^{bkg}_{HeII} = 10^{-14.9}$s^{-1} *and* $Q_{4Ry} = 10^{56.1}$s^{-1}*; b) evolution of the median He II fraction* x_{HeII} *for each of the models; c) total photoionization rate* Γ_{tot} *(dashed line corresponds to the total unattenuated photoionization rate). Left side panels show models with He II ionizing background* $\Gamma^{bkg}_{HeII} = 10^{-14.9}$s^{-1}*, while the right side panels show models with zero background, i.e.,* $\Gamma^{bkg}_{HeII} = 0$*. The equilibration timescale* t_{eq} *is plotted on the right y-axis in the bottom panel.*

fraction x_{HeII}, and the total photoionization rate $\Gamma_{tot} = \Gamma_{QSO} + \Gamma^{bkg}_{HeII}$ together with the unattenuated photoionization rate $\Gamma_{unatt.}$. The panels on the left show the models with fixed values of $\Gamma^{bkg}_{HeII} = 10^{-14.9}$s^{-1}, whereas the right side illustrates the $\Gamma^{bkg}_{HeII} = 0$ case. The photon production rate has been set to fiducial value $Q_{4Ry} = 10^{56.1}$s^{-1} throughout.

Several qualitative trends are readily apparent from Figure 4.2. First, as was also mentioned in § 3.3, at the smallest radii $R \lesssim 5$ cMpc, there is a 'core' of the proximity zone, which is insensitive to the changes of the quasar lifetime such that all transmission profiles overlap. Second, it is clear that both with ($\Gamma^{bkg}_{HeII} = 10^{-14.9}$s^{-1}) and without ($\Gamma^{bkg}_{HeII} = 0$) a He II ionizing background, increasing the quasar lifetime t_Q results in larger proximity zones, reflecting the longer time that the nearby IGM has been exposed to the radiation from the quasar. Third, in the presence of a He II

ionizing background $\Gamma^{\rm bkg}_{\rm HeII} = 10^{-14.9}{\rm s}^{-1}$, the transmission profile shape loses sensitivity to quasar lifetime for models with $t_{\rm Q} > 25$ Myr, whereas for $\Gamma^{\rm bkg}_{\rm HeII} = 0$ case, the proximity zone continues to grow with increasing quasar lifetime up to large values of $t_{\rm Q} = 500\,{\rm Myr}$.

We can gain a better physical understanding of the origin of these trends from the equation that describes the time evolution of the He II fraction $x_{\rm HeII}\,(t)$ given by eqn. (3.3) and discussed in § 3.2 and § 3.3. In what follows we focus on the specific example $\Gamma^{\rm bkg}_{\rm HeII} = 10^{-14.9}{\rm s}^{-1}$, but our discussion also applies to the case of zero ionizing background, provided that the equation for the time evolution is modified to account for the time-delay associated with the arrival of the ionization front (see eqn. (3.6) in § 3.2). At $z \sim 3$, observations of the effective optical depth strongly favor a finite background (see § 3.1) $\Gamma^{\rm bkg}_{\rm HeII} \simeq 10^{-14.9}{\rm s}^{-1}$ ($x_{\rm HeII} \simeq 10^{-2}$), although most of the previous interpretations of observed He II proximity regions have concentrated on the $\Gamma^{\rm bkg}_{\rm HeII} = 0$ case (Shull et al. 2010; Syphers & Shull 2014; Zheng et al. 2015).

4.1 THE DEPENDENCE ON QUASAR LIFETIME

The three panels in Figure 4.3 show the time evolution of the He II fraction at three different distances from the quasar $R = [3, 25, 50]$ cMpc, labeled A, B, and C, respectively. The black curves show the average $x_{\rm HeII}\,(t)$ computed from 100 skewers, where the quasar was on for the entire $t_{\rm Q} = 100$ Myr that is shown. The dashed blue curves show the time evolution from eqn. (3.3), where for the input parameters we have averaged the outputs from the radiative transfer code. Specifically, to compute the blue curves we take an average value of photoionization rate $\langle\Gamma_{\rm tot}\rangle$ which is a mean of 100 skewers and we do the same for the equilibrium $x_{\rm HeII,eq} = \langle\alpha_{\rm A}\,({\rm T})\,n_{\rm e}\rangle/\langle\Gamma_{\rm tot}\rangle$, and initial neutral fractions $x_{\rm HeII,0} = \langle\alpha_{\rm A}\,({\rm T})\,n_{\rm e}\rangle/\Gamma^{\rm bkg}_{\rm HeII}$ [1].

This procedure excellently reproduces the evolution given by the solid black curves, computed from a full time integration of the radiative transfer. Whereas we previously saw that this analytical approximation provides a good fit to the time evolution of the He II fraction of a single skewer (see Figure 3.2), it is somewhat surprising that it also works so well for the stacked spectra using these averaged quantities.

As Figure 4.3 shows the full time evolution of He II fraction over 100 Myr, observing a quasar with a given quasar lifetime $t_{\rm Q}$ is equivalent to evaluating $x_{\rm HeII}\,(t)$ at the time

[1] Note, however, that taking the average values of $\langle\alpha_{\rm A}\,({\rm T})\rangle$ and $\langle n_{\rm e}\rangle$ separately does not reproduce the time integrated results from the radiative transfer because these two quantities are highly correlated due to the temperature-density relation and thus $\langle\alpha_{\rm A}\,({\rm T})\,n_{\rm e}\rangle \neq \langle\alpha_{\rm A}\,({\rm T})\rangle\langle n_{\rm e}\rangle$.

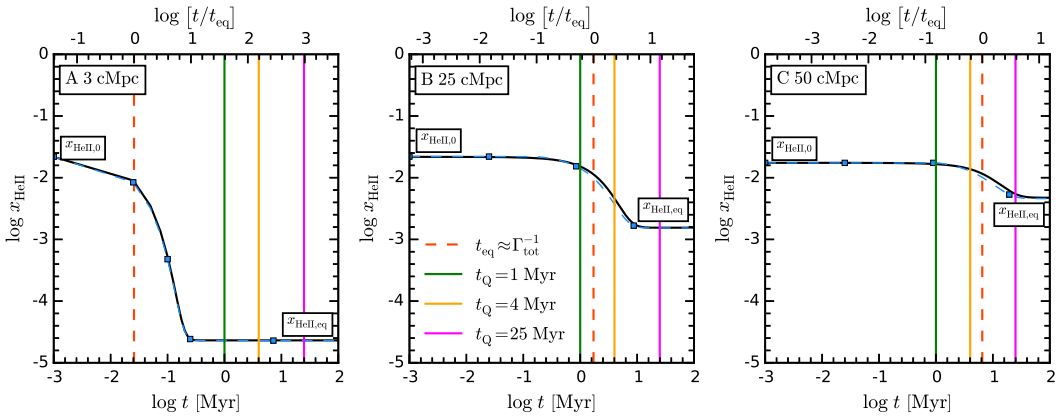

FIGURE 4.3: *Time evolution of* $x_{\rm HeII}\,(t, R)$ *at different distances from the quasar: A)* 3 *cMpc, B)* 25 *cMpc, and C)* 50 *cMpc. Solid black and dashed blue curves show* $x_{\rm HeII}\,(t, R)$ *evolution as output from the radiative transfer algorithm and analytical approximation based on eqn. (3.3), respectively. Red dashed vertical lines in each panel show the equilibration time* $t_{\rm eq}$ *at the distance R; green, orange and magenta vertical lines indicate three quasar lifetimes we consider here, i.e.,* $t_{\rm Q} = [1, 4, 25]$ *Myr. These calculations use our fiducial value of the He II ionizing background* $\Gamma^{\rm bkg}_{\rm HeII} = 10^{-14.9}{\rm s}^{-1}$*, and have a photon production rate* $Q_{\rm 4Ry} = 10^{56.1}\ {\rm s}^{-1}$.

$t = t_{\rm Q}$. The green, yellow, and magenta vertical lines indicate three possible quasar lifetimes of $t_{\rm Q} = 1,\ 4,$ and 25 Myr, respectively. The spatial profile of $x_{\rm HeII}$ and Lyα transmission are shown in the middle and bottom panels of Figure 4.4 for the same three quasar lifetime models (with the same line colors as in Figure 4.3). The black curves in these two panels show the "equilibrium" $t = \infty$ profiles for $x_{\rm HeII}$ and the transmission, which we define to correspond to $t_{\rm Q} = 100\,{\rm Myr}$, at which time $x_{\rm HeII}$ has fully equlibrated. The vertical dashed lines labeled A, B, and C in Figure 4.4 indicate the three distances from the quasar $R = [3, 25, 50]$ cMpc for which the time evolution is shown in Figure 4.3.

First, consider location A in the inner 'core' of the proximity zone at a distance of $R = 3$ cMpc, at which the He II fraction and transmission profiles in Figure 4.4 are all identical for the quasar lifetimes we consider. The uppermost panel of Figure 4.4 shows the equilibration time as a function of distance from the quasar, which indicates that at $R = 3\,{\rm cMpc}$ $t_{\rm eq} = 0.025$ Myr. The reason why all quasar lifetimes are indistinguishable at this distance can be easily understood from the $x_{\rm HeII}\,(t)$ evolution in the left panel of Figure 4.3. Irrespective of whether the quasar has been emitting for $t_{\rm Q} = 1$ Myr (green), $t_{\rm Q} = 4$ Myr (yellow) or $t_{\rm Q} = 16$ Myr (magenta), because at this distance the equilibration time (red vertical dashed line) $t_{\rm eq} \ll t_{\rm Q}$, the IGM has already equilibrated $x_{\rm HeII,eq} \simeq 2.5 \times 10^{-5}$, and there is thus no sensitivity to quasar

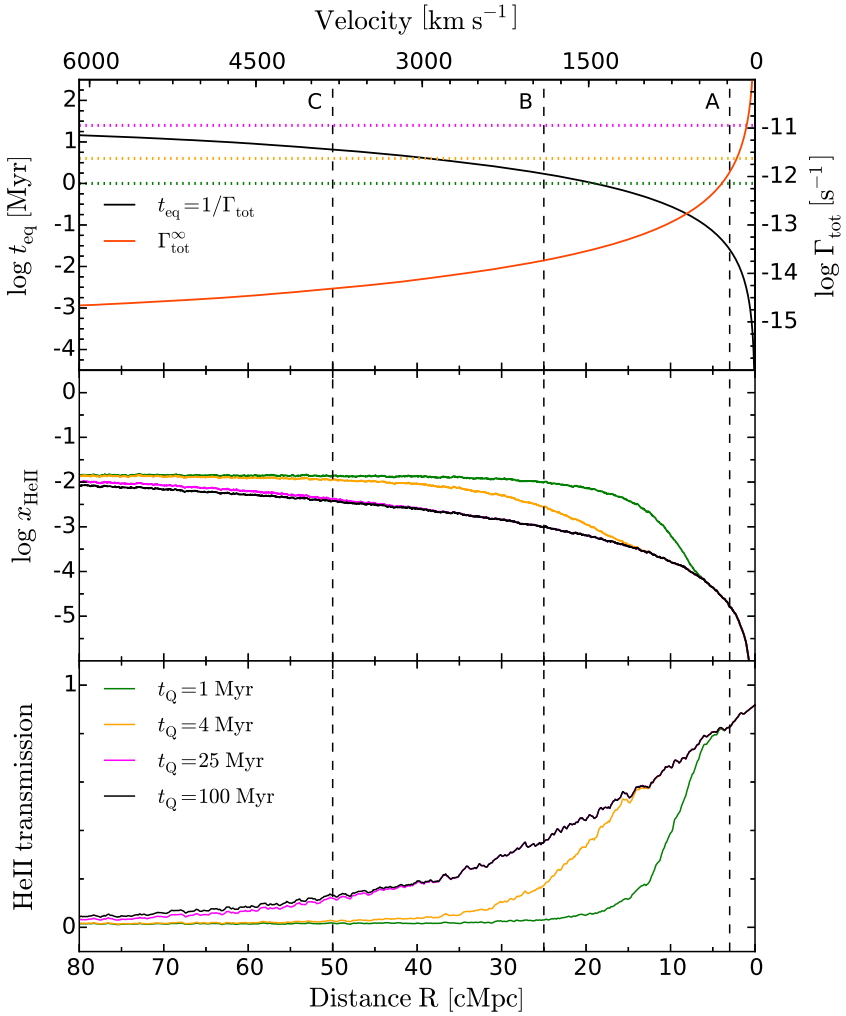

FIGURE 4.4: *Top panel: total photoionization rate* $\Gamma_{\rm tot}$ *as a function of distance R (red) and the equilibration time* $t_{\rm eq} = 1/\Gamma_{\rm tot}$ *(black). Dashed vertical lines correspond to the locations A,B and C in Figure 4.3 where we traced the time-evolution of the He II fraction. Three horizontal dotted lines in the upper panel correspond to the values of quasar lifetimes* $t_{\rm Q}$ *that we consider in Figure 4.3. Middle panel: time evolution of the He II fraction computed at* $t = t_{\rm Q} = [1, 4, 25, 100]$ Myr *as a function of distance R from the quasar. Bottom panel: stacked transmission profiles for models with different quasar lifetimes (same as Figure 4.2).*

lifetime (see also the discussion in § 3.3 and eqn. 3.7).

Note however that the $t_{\rm eq} \sim R^2$ dependence of equilibration time shown in the top panel of Figure 4.4 indicates that at greater distances, the equilibration time is larger and becomes comparable to the lifetimes we consider. This manifests as significant differences in the stacked $x_{\rm HeII}$ and transmission profiles for different lifetimes in

Figure 4.4, which can again be understood from the time evolution in Figure 4.3. For example, consider location B (middle panel of Figure 4.3) at $R = 25$ cMpc, at which the equilibration time is $t_{\rm eq} = 1.7$ Myr (red vertical dashed line). For the shortest quasar lifetime of 1 Myr (green line), the IGM has not been illuminated long enough to equilibrate, i.e., $t_{\rm Q} < t_{\rm eq}$, and thus still reflects the He II fraction $x_{\rm HeII,0}$ consistent with the $\Gamma^{\rm bkg}_{\rm HeII}$ that prevailed before the quasar turned on. This $x_{\rm HeII,0} \simeq 2.2 \times 10^{-2}$, much larger than the equilibrium value $x_{\rm HeII,eq} \simeq 1.5 \times 10^{-3}$, explains why the corresponding transmission at location B in Figure 4.4 (green curve) lies far below the fully equilibrated model $t_{\rm Q} = 100$ Myr (black curve). Likewise, the $t_{\rm Q} = 4$ Myr model (yellow) is still in the process of equilibriating, whereas the $t_{\rm Q} = 25$ Myr model (magenta) has fully equilibrated, explaining the respective values of the $x_{\rm HeII}$ and transmission for these models at location B in Figure 4.4.

Because equilibration time increases with distance from the quasar, the stacked transmission profile becomes sensitive to larger quasar lifetimes at larger radii. This is evident from the transmission profiles in Figure 4.2 and Figure 4.4, where models with progressively larger lifetimes peel off from the equilibrium model ($t_{\rm Q} = 100$ Myr) at progressively larger radii. However, eventually far from the quasar, this sensitivity saturates, as $t_{\rm eq}$ approaches its asymptotic value $t_{\rm eq} \sim 1/\Gamma^{\rm bkg}_{\rm HeII}$ (see upper panel of Figure 4.4), which for our fiducial $\Gamma^{\rm bkg}_{\rm HeII} = 10^{-14.9}{\rm s}^{-1}$ corresponds to $t_{\rm eq} = 25$ Myr. This saturation effect is illustrated by the time evolution at location C, $R = 50$ cMpc from the quasar, in the right panel of Figure 4.3. If the quasar has been illuminating the IGM for $t_{\rm Q} = 25$ Myr (magenta curve), the He II fraction has nearly reached equilibrium $x_{\rm HeII,eq}$, and thus at location C Figure 4.4 exhibits only a small but still noticeable difference between the $x_{\rm HeII}$ at $t_{\rm Q} = 25$ Myr and the equilibrium model (black curve), and consequently the transmission profiles (lower panel) hardly differ at all. It would clearly be extremely challenging to distinguish between different models with $t_{\rm Q} > 25$ Myr. Finally, at the largest radii $R > R_{\rm bkg} = 70$ cMpc, where $R_{\rm bkg}$ is defined to be the location where $\Gamma^{\rm bkg}_{\rm HeII} = \Gamma_{\rm QSO}$, the quasar no longer dominates over the background, and all the transmission profiles converge to the mean transmission set by the He II background. Finally, we again note that if $\Gamma^{\rm bkg}_{\rm HeII} = 0$, there is no such asymptote in the equilibration time, and the transmission profile continues to be sensitive to values of quasar lifetime as large as $t_{\rm Q} = 500\,$Myr as shown in Figure 4.2. However, in practice for very long quasar lifetimes and therefore very large proximity zones, one might eventually encounter locations in the universe where the background is no longer zero.

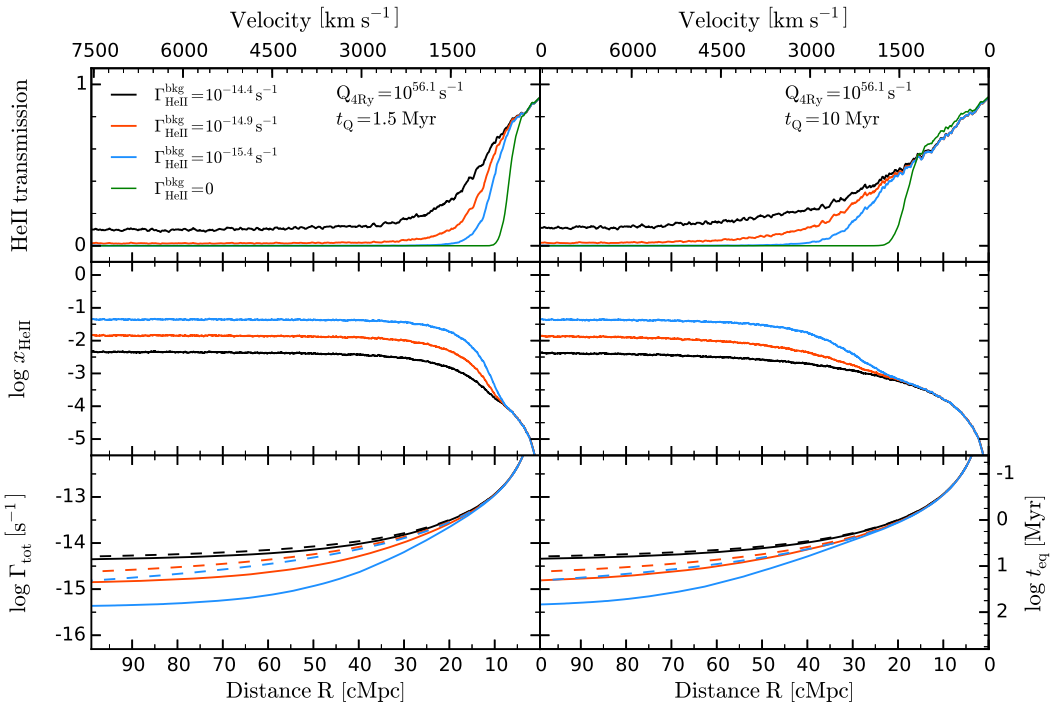

FIGURE 4.5: *Stacked proximity region trends when varying the He II ionizing background, where each curve is calculated from* 1000 *skewers. Lefthand panels show three models with* $\Gamma^{\rm bkg}_{\rm HeII} = \left[10^{-14.4}, 10^{-14.9}, 10^{-15.4}, 0\right]$ s^{-1} *for a quasar lifetime* $t_{\rm Q} = 1.5$ *Myr. Righthand panels show the same models of* $\Gamma^{\rm bkg}_{\rm HeII}$ *but for the quasar lifetime* $t_{\rm Q} = 10$ *Myr. All panels take a photon production rate of* $Q_{\rm 4Ry} = 10^{56.1}{\rm s}^{-1}$. *See Figure 4.2 for a description of the quantities plotted on the y-axis.*

4.2 THE DEPENDENCE ON HE II IONIZING BACKGROUND

In Figure 4.5 we illustrate the impact of varying the He II ionizing background $\Gamma^{\rm bkg}_{\rm HeII}$ on the stacked transmission profile, with $t_{\rm Q}$ and $Q_{\rm 4Ry}$ held fixed. The left panels show a quasar lifetime of $t_{\rm Q} = 1.5$ Myr, whereas the right show $t_{\rm Q} = 10$ Myr. Four different values for $\Gamma^{\rm bkg}_{\rm HeII}$ are plotted, including the $\Gamma^{\rm bkg}_{\rm HeII} = 0$ case.

From Figure 4.5, we see that in the inner core $R < 5$ cMpc of the proximity zone, the transmission profile is independent of $\Gamma^{\rm bkg}_{\rm HeII}$, analogous to the behavior in Figure 4.2, where we saw that the core is also independent of $t_{\rm Q}$. As discussed in § 3.3 (see also the previous section), this insensitivity to $\Gamma^{\rm bkg}_{\rm HeII}$ and $t_{\rm Q}$ can be understood from eqn. (3.7) governing the time evolution of $x_{\rm HeII}$. For $t_{\rm eq} \ll t_{\rm Q}$, the IGM has already equilibrated and $x_{\rm HeII}(t_{\rm Q}) \approx x_{\rm HeII,eq}$. At small distances $R \ll R_{\rm bkg}$ the quasar dominates over the background $\Gamma_{\rm QSO} \gg \Gamma^{\rm bkg}_{\rm HeII}$ and attenuation is negligible, hence

the equilibrium He II fraction $x_{\rm HeII,eq} \propto \Gamma_{\rm QSO}^{-1}$ is determined by the quasar photon production rate alone, and is independent of the background and quasar lifetime.

In the previous section we argued that the equilibration time picture explains why the transmission profiles for progressively larger lifetimes peel off from the equilibrium model ($t_{\rm Q} = 100$ Myr) at progressively larger radii (see Figure 4.2). The curves in Figure 4.5 illustrate that varying the ionizing background has a different effect, namely to change the slope of the transmission profile about this peel off point, as well as to determine the transmission level far from quasar. The different response of the transmission profile to these two parameters, $t_{\rm Q}$ and $\Gamma_{\rm HeII}^{\rm bkg}$, results from the functional form of eqn. (3.7). The stronger peel off behavior with $t_{\rm Q}$ is due to the exponential dependence on the quasar lifetime $t_{\rm Q}$ in eqn. (3.7), whereas the milder variation of the slope with $\Gamma_{\rm HeII}^{\rm bkg}$ arises because of the inverse proportionality of $x_{\rm HeII,eq}$ on $\Gamma_{\rm HeII}^{\rm bkg}$. Furthermore, at large distances from the quasar where $\Gamma_{\rm tot} \simeq \Gamma_{\rm HeII}^{\rm bkg}$, $x_{\rm HeII,eq}$ approaches $x_{\rm HeII,0} \propto 1/\Gamma_{\rm HeII}^{\rm bkg}$ and the background sets the absorption level as expected. As we also noted in § 3.3, the different dependence of the transmission profile on $t_{\rm Q}$ and $\Gamma_{\rm HeII}^{\rm bkg}$ suggests that the degeneracy between these parameters could be broken by the shape of the transmission profile, which we discuss further in § 4.5.1.

4.3 THE DEPENDENCE ON QUASAR PHOTON PRODUCTION RATE

Figure 4.6 shows the effect of the photon production rate on the structure of the proximity zone. The quasar lifetime has been set to the value $t_{\rm Q} = 10$ Myr, and the background is $\Gamma_{\rm HeII}^{\rm bkg} = 10^{-14.9}{\rm s}^{-1}$ on the left and $\Gamma_{\rm HeII}^{\rm bkg} = 0$ on the right. One can see that the impact of the photon production rate $Q_{\rm 4Ry}$ on the resulting transmission profile is twofold. First, as expected, more luminous quasars produce larger proximity zones, i.e., increasing the photon production rate by 0.5 dex expands the characteristic size of the proximity zone by a factor of ~ 2. Second, besides increasing the overall size, the slope of the stacked transmission profile becomes shallower when $Q_{\rm 4Ry}$ is increased.

The increase in proximity zone size with $Q_{\rm 4Ry}$ can be easily understood in the equilibration time picture. From eqn. (3.9), we see that the equilibration distance $R_{\rm eq}$, which sets the location where the transmission profile becomes sensitive to $t_{\rm Q}$ and approaches the mean transmission level of the IGM (see Figure 4.2), scales as $R_{\rm eq} \propto Q_{\rm 4Ry}^{1/2}$. Hence an increase (decrease) in photon production rate $Q_{\rm 4Ry}$ results in a larger (smaller) characteristic size of the proximity zone.

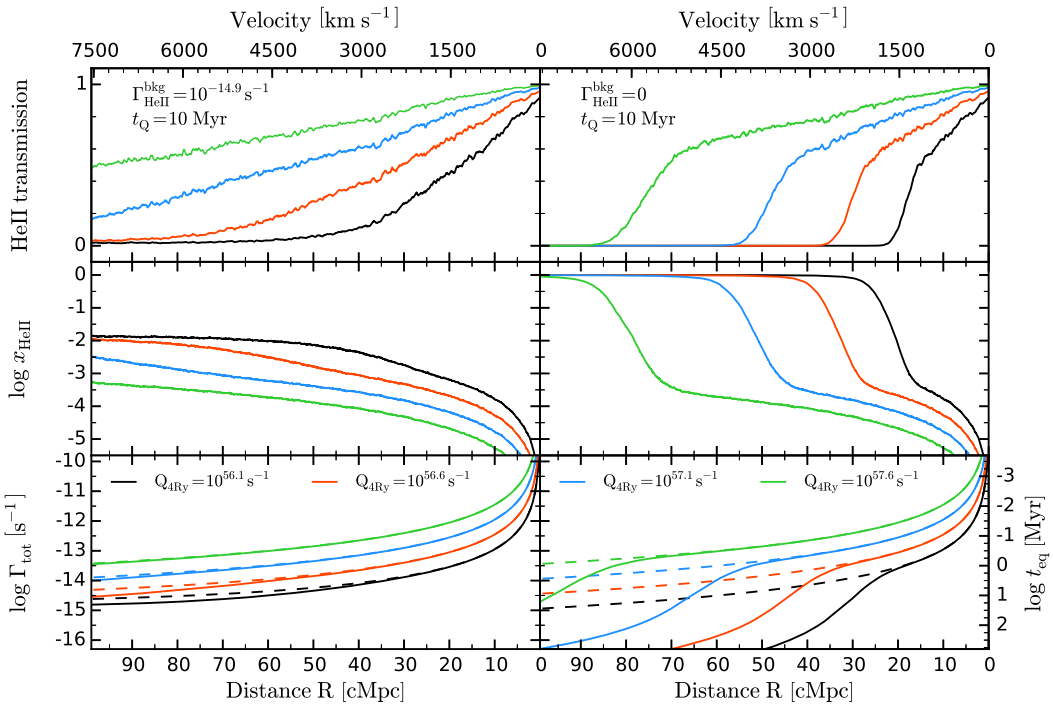

FIGURE 4.6: *Stacked proximity region trends with varying the quasar* 4 *Ry photon production rate,* $Q_{\rm 4Ry}$*, where each curve is calculated from* 1000 *skewers. All curves assume a fixed quasar lifetime of* $t_{\rm Q} = 10$ *Myr and fixed He II ionizing background* $\Gamma^{\rm bkg}_{\rm HeII}$ *where the lefthand panels take* $\Gamma^{\rm bkg}_{\rm HeII} = 10^{-14.9}{\rm s}^{-1}$ *and the righthand panels take* $\Gamma^{\rm bkg}_{\rm HeII} = 0$ *(i.e.,* $x_{\rm HeII} = 1$*). See Figure 4.2 for a description of the quantities plotted on the y-axis.*

To understand the change in transmission profile slope with $Q_{\rm 4Ry}$, consider that in the core of the proximity zone where $t_{\rm eq} \ll t_{\rm Q}$, the He II fraction has equilibrated and is given by $x_{\rm HeII}\,(t) = x_{\rm HeII,eq}$, where $x_{\rm HeII,eq} \propto Q^{-1}_{\rm 4Ry}$. As the transmitted flux is just the exponential of a constant times $x_{\rm HeII,eq}$, an increase (decrease) in $Q_{\rm 4Ry}$ makes this exponent smaller (larger) and thus the slope of the transmission profile becomes shallower (steeper).

4.4 DISTRIBUTION OF QUASAR LIFETIMES AND HE II BACKGROUNDS

In the previous sections we assumed only single values of quasar lifetime and He II background when exploring their impact on the stacked transmission profiles. How-

ever, this approach is probably too simplistic because in reality these parameters are expected to vary. The He II background will fluctuate from one line-of-sight to another due to the density fluctuations. Analogously, quasars will also have a distribution of the lifetimes. Therefore, in this section we want to check if the results we obtained in previous sections still hold if we consider more realistic models with a distribution of quasar lifetimes and He II ionizing backgrounds as one expects to encounter in the universe. In what follows we study the impact of the distribution of quasar lifetimes and He II backgrounds on the shape of the stacked transmission profiles in He II Lyα regions at $z = 3.1$ using the same stacking technique.

First, we consider the distribution of quasar lifetimes only, while keeping He II background and quasar photon production rate fixed to our fiducial values $\Gamma^{\rm bkg}_{\rm HeII} = 10^{-14.9}{\rm s}^{-1}$ and $Q_{\rm 4Ry} = 10^{56.1}{\rm s}^{-1}$, respectively. The upper panel of Figure 4.7 shows the comparison between the stacked transmission profiles of our fiducial model with single quasar lifetime $t_{\rm Q} = 10$ Myr and three models with different distributions of $t_{\rm Q}$. We model the distribution of quasar lifetimes as a uniform sampling from 5 discrete $t_{\rm Q}$ values centered on $\log\,(t_{\rm Q}/{\rm Myr}) = 1.00$ spanning a total range of $0 \leq \log\,(t_{\rm Q}/{\rm Myr}) \leq 2$, but with different widths $\Delta\log\,(t_{\rm Q}/{\rm Myr}) = [0.5, 1.0, 2.0]$. This is done by constructing stacks of 1000 skewers, where each skewer is randomly chosen from one of the single lifetime models over the range specified by the width. The black curve in the upper panel of Figure 4.7 represents the stack of skewers taken from models with $\log\,(t_{\rm Q}/{\rm Myr}) = [0.75, 0.875, 1.00, 1.125, 1.25]$, red is a stack of skewers with $\log\,(t_{\rm Q}/{\rm Myr}) = [0.50, 0.75, 1.00, 1.25, 1.50]$ and green is $\log\,(t_{\rm Q}/{\rm Myr}) = [0.00, 0.50, 1.00, 1.50, 2.00]$. The numbers in square brackets represent the values of $t_{\rm Q}$ or $\Gamma^{\rm bkg}_{\rm HeII}$ (see below) used in the models that contributed to the stacks of the distribution models.

The upper panel of Figure 4.7 clearly shows that in comparison to the single lifetime model, there appears to be a reduction in the transmission in the range $R \simeq 10 - 40$ cMpc in the stacked spectra of models with the distribution of quasar lifetimes. This is due to the skewers with lower values of $t_{\rm Q}$. In these models the IGM did not have enough time to respond to the changes in the radiation field caused by the quasar and still reflects a higher He II fraction set by the He II ionizing background, resulting in decreased transmission. Furthermore, the transmission becomes more depressed as the width of the quasar lifetime distribution increases, indicating that stacked transmission profiles are also sensitive to the width of the quasar lifetime distribution.

Similarly, we now investigate how the distribution of He II backgrounds affects the stacked transmission profiles. As we discussed in § 3.1, our fiducial value of He II background $\Gamma^{\rm bkg}_{\rm HeII} = 10^{-14.9}{\rm s}^{-1}$ is derived from measurements of the He II effective optical depth $\tau_{\rm eff}$ which give $\tau_{\rm eff} \simeq 4.5$ at $z = 3.1$ (see Figure 3.1). Therefore, the

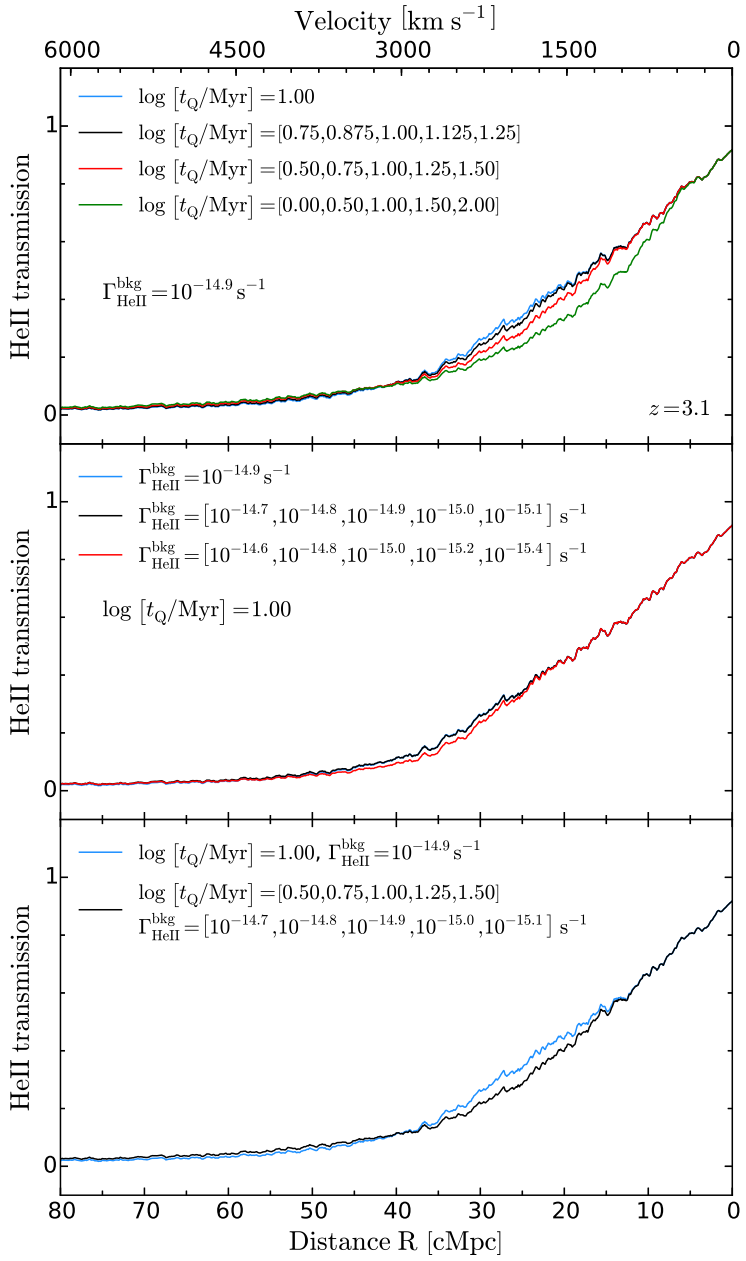

FIGURE 4.7: *Top panel: effect of the quasar lifetime distribution on the stacked transmission profile. The He II background is fixed for all models to* $\Gamma^{bkg}_{HeII} = 10^{-14.9}s^{-1}$. *Each of the curves represents a stack of* 1000 *skewers. The blue curve shows the stacked profile of the model with single value of quasar lifetime* $t_Q = 10$ *Myr, while other curves correspond to the stacked profiles of the models that take distribution of* t_Q *with different widths:* log (t_Q/Myr) = [0.75, 0.875, 1.00, 1.125, 1.25] *(black),* log (t_Q/Myr) = [0.50, 0.75, 1.00, 1.25, 1.50] *(red),* log (t_Q/Myr) = [0.00, 0.50, 1.00, 1.50, 2.00] *(green). Middle panel: The same, but for distribution of He II backgrounds. Quasar lifetime is fixed to* log (t_Q/Myr) = 1.00. *The blue curve has a fiducial value of* $\Gamma^{bkg}_{HeII} = 10^{-14.9}s^{-1}$, *and other curves take the distribution of backgrounds, i.e.,* $\Gamma^{bkg}_{HeII} = \left[10^{-14.7}, 10^{-14.8}, 10^{-14.9}, 10^{-15.0}, 10^{-15.1}\right]s^{-1}$ *(black),* $\Gamma^{bkg}_{HeII} = \left[10^{-14.6}, 10^{-14.8}, 10^{-15.0}, 10^{-15.2}, 10^{-15.4}\right]s^{-1}$ *(red). Bottom panel: The combined effect of the distributions of quasar lifetimes and He II backgrounds.*

distribution of He II ionizing backgrounds should also correspond to the same observed mean effective optical depth of $\tau_{\rm eff} \simeq 4.5$. Analogously to § 3.1, we run our radiative transfer calculation with the quasar turned off for 100 skewers chosen from several models with different values of the He II background. We focus on two uniform distributions for $\Gamma^{\rm bkg}_{\rm HeII}$ which yield the same effective optical depth $\tau_{\rm eff} \simeq 4.5$: $\Gamma^{\rm bkg}_{\rm HeII} = \left[10^{-14.7}, 10^{-14.8}, 10^{-14.9}, 10^{-15.0}, 10^{-15.1}\right] {\rm s}^{-1}$ and $\Gamma^{\rm bkg}_{\rm HeII} = \left[10^{-14.6}, 10^{-14.8}, 10^{-15.0}, 10^{-15.2}, 10^{-15.4}\right] {\rm s}^{-1}$. We then run our 1D radiative transfer algorithm with the quasar on for $t_{\rm Q} = 10$ Myr and calculate 10 different models with the above mentioned values of He II background. Similar to the distribution of quasar lifetimes, we calculate two stacked transmission profiles using 1000 skewers randomly chosen from these models.

The results of this exercise are shown in the middle panel of Figure 4.7, where the blue curve corresponds to the model with a single value of He II background fixed at our fiducial value of $\Gamma^{\rm bkg}_{\rm HeII} = 10^{-14.9} {\rm s}^{-1}$, the black curve shows the model with a background distribution that spans a range of 0.4 dex $\Gamma^{\rm bkg}_{\rm HeII} = \left[10^{-14.7} - 10^{-15.1}\right] {\rm s}^{-1}$, and the red curve is for the model spanning 0.8 dex $\Gamma^{\rm bkg}_{\rm HeII} = \left[10^{-14.6} - 10^{-15.4}\right] {\rm s}^{-1}$. It is apparent that for the distributions we consider here, varying the He II background, but in such a way that the mean effective optical depth is fixed, has only a small effect on the resulting transmission profile. Thus, comparing to the upper panel of Figure 4.7 we can conclude that the distribution of quasar lifetimes has a dominant effect on the stacked transmission profile and future attempts to model stacked proximity zone should take this into account. This is illustrated in the bottom panel of Figure 4.7 where we combine these effects and model both the distributions of quasar lifetimes $t_{\rm Q}$ and He II backgrounds $\Gamma^{\rm bkg}_{\rm HeII}$ simultaneously, by combining skewers drawn from different models in both parameters.

In § 4.1 and § 4.2 we showed that variations in the quasar lifetime and He II background impact stacked transmission profiles in distinct ways. Our analysis here shows that the width of the distribution of quasar lifetimes, can significantly change the shape of the stacked transmission profile, and should be included in any attempt to model real observations. Nevertheless, we argue that that at $z \simeq 3.1$ one should be able to put interesting constraints on the quasar lifetime given that the average He II background can be determined from the level of transmission in the IGM as quantified by effective optical depth measurements (see Figure 3.1 in § 3.1), and due to the fact that the stacked transmission profile is relatively insensitive to fluctuations in the He II background.

4.5 PROSPECTS AT $z \simeq 4$

The complete reionization of intergalactic helium is a temporally extended process and the conditions in the IGM will evolve and might affect the sensitivity of our models to the quasar and IGM parameters. Recall Figure 3.1, where the blue curve shows the evolution of the mean He II effective optical depth $\tau_{\rm eff}$ and the mean He II fraction at $z = 3.9$ in our simulations. At this higher redshift, the $\tau_{\rm GP} \propto (1+z)^{3/2}$ dependence of the optical depth, implies that even backgrounds which correspond to a IGM with on average relatively low He II fraction of only $\simeq 0.03 - 0.04$, correspond to very large effective optical depth is $\tau_{\rm eff} \simeq 8 - 9$. Thus, unlike the situation at $z \simeq 3$, it would be extremely challenging to measure an optical depth that high with HST/COS, making it virtually impossible to measure the He II background and thus distinguish between IGM with low He II fraction ($x_{\rm HeII} < 0.05$) and the high He II fraction ($x_{\rm HeII} = 1$) at $z \simeq 4$. It is, therefore, interesting to explore whether the shape of the transmission profile of He II proximity zones can be used to independently probe both the quasar lifetime and the He II background at $z \sim 4$, where the background cannot be independently constrained. In what follows we consider two diagnostic methods. First, we use the same stacked transmission profiles that we discussed in previous sections. Second, we study the distribution of the He II proximity zone sizes, the statistics that has been previously used in the literature to characterize high-redshift H I and He II proximity zones.

4.5.1 STACKED TRANSMISSION PROFILES AT $z \simeq 4$

We begin by applying our method to skewers drawn from the same hydrodynamical simulation at redshift $z = 3.9$. Following our approach in the previous section, we choose a finite background model with uniform distribution $\Gamma^{\rm bkg}_{\rm HeII} = [10^{-14.5}, 10^{-14.7}, 10^{-14.9}, 10^{-15.1}, 10^{-15.3}]$ s^{-1}. For the distribution of lifetimes we adopt $\log(t_{\rm Q}/{\rm Myr}) = [0.50, 0.75, 1.00, 1.25, 1.50]$, and fix the photon production rate to $Q_{\rm 4Ry} = 10^{56.1}{\rm s}^{-1}$. The resulting stacked transmission profile is shown by the blue curve in Figure 4.8. Despite the finite background and relatively small average He II fraction $\langle x_{\rm HeII}\rangle \simeq 0.05$, far from the quasar $R > 50$ cMpc, the average transmission is very nearly zero reflecting the large effective optical depth $\tau_{\rm eff} \simeq 8 - 9$ for this model. The dashed black curve in Figure 4.8 shows the stacked transmission profile for a model with the same distribution of quasar lifetimes, but with $\Gamma^{\rm bkg}_{\rm HeII} = 0$ and hence an IGM with $\langle x_{\rm HeII}\rangle = 1.0$, and $Q_{\rm 4Ry}$ fixed to the same value. In the absence of the He II background, one sees that the proximity zone is smaller, and the transmission approaches zero at smaller distance from the quasar than for the finite

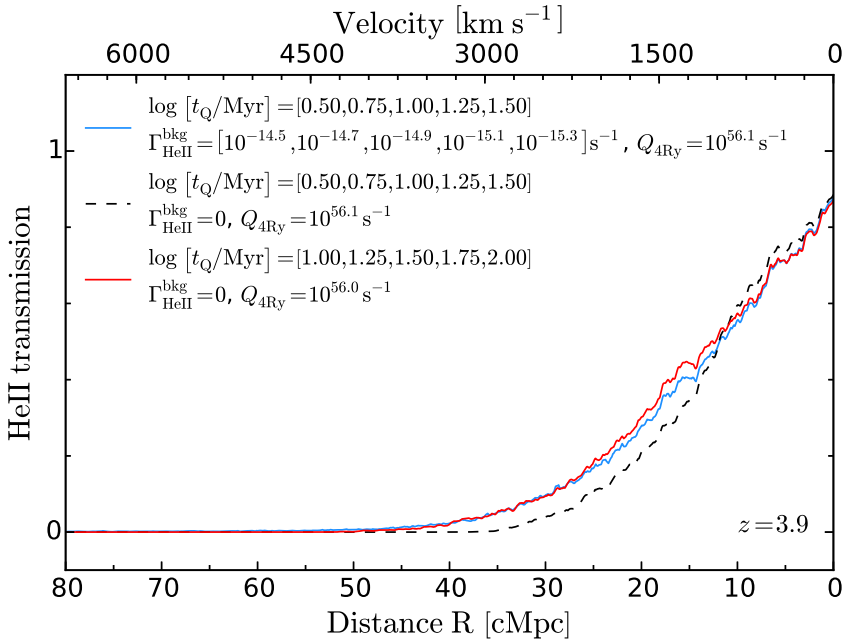

FIGURE 4.8: *Comparison between the stacked finite He II background model with* $\Gamma^{bkg}_{HeII} = \left[10^{-14.5}, 10^{-14.7}, 10^{-14.9}, 10^{-15.1}, 10^{-15.3}\right]$ s^{-1}, log (t_Q/Myr) = [0.50, 0.75, 1.00, 1.25, 1.50] *(solid blue curve) and zero He II background models (x_{HeII} = 1 initially) with the same quasar lifetime distribution (dashed black curve). Both models have a fiducial value of photon production rate* $Q_{4Ry} = 10^{56.1}$s^{-1}. *The solid red curve shows the model with* log (t_Q/Myr) = [1.00, 1.25, 1.50, 1.75, 2.00] *and reduced photon production rate* $Q_{4Ry} = 10^{56.0}$s^{-1}. *All calculations are performed at quasar redshift* z = 3.9.

background model. This significant difference in the transmission profile naively suggests that proximity zones can be used to determine the value of the background.

However, clearly one way of compensating for this difference between the transmission profiles is to consider: 1) a distribution with longer quasar lifetimes and, 2) a change in the quasar photon production rate Q_{4Ry}, for the zero background model. Both of these parameter variations change the size of the proximity zone, which could make the two models look more similar. In principle the photon production rate Q_{4Ry} should be determined by our knowledge of the quasar magnitudes, however in practice the average quasar SED is not well constrained at energies above 4 Ry, giving rise to at least $\sim$ 50% relative uncertainty in Q_{4Ry} (see e.g. Lusso et al. 2015). To illustrate these parameter degeneracies, we increase the values of t_Q in our distribution for the zero background model by 0.50 dex to log (t_Q/Myr) = [1.00, 1.25, 1.50, 1.75, 2.00], and simultaneously slightly reduce the value of the photon production rate by 0.1 dex to $Q_{4Ry} = 10^{56.0}$s^{-1}. The result of this exercise is shown by the solid red curve in Fig-

ure 4.8, which shows that the the transmission profiles for a highly doubly ionized helium ($\langle x_{\rm HeII}\rangle = 0.05$) and a completely singly ionized helium ($\langle x_{\rm HeII}\rangle = 1.0$) are essentially indistinguishable.

In conclusion we see, that at $z \sim 4$ the limited sensitivity of HST/COS combined with the steep rise of effective optical depth with redshift (see Figure 3.1), implies that one will likely only be able to place lower limits on the the average effective optical depth $\tau_{\rm eff}$, and hence upper limits on the value of the He II background. The two very different models that we considered for the He II background in Figure 4.8 are expected to be consistent with such limits. Without an independent measurement on the He II background, and given our poor knowledge of the SEDs of quasars above 4 Ryd, the similarity of the models in Figure 4.8 (blue and red curves) illustrate that it will be extremely challenging to break the degeneracies between quasar lifetime, ionizing background, and photon production rate, given existing data or even data that might be collected in the future with HST/COS. Thus, in contrast with $z \sim 3$, where an independent determination of the the He II background from effective optical depth measurements allows one to infer the quasar lifetime from proximity zones, the proximity zones of $z \sim 4$ quasars alone cannot independently constrain the quasar lifetime and ionization state of the IGM. Nevertheless, a degenerate combination of these parameters would still be extremely informative, and could be combined with other measurements to yield tighter constraints.

4.5.2 DISTRIBUTION OF THE PROXIMITY ZONE SIZES

Previous studies of H I proximity zones at $z \simeq 6$ have concentrated on the location of the 'edge' of the ionized regions in order to infer the unknown parameters governing proximity zones. In this section we adopt a similar technique to investigate if it is a better diagnostic tool than stacking, considered in the previous section, for constraining the properties of the IGM and quasars at $z = 3.9$.

We follow previous conventions (Fan et al. 2006b) and define the size of the He II proximity zone to be the location where the appropriately smoothed transmission profile crosses the threshold value $F = 0.1$ for the first time. For the choice of smoothing we follow conventions that have been adopted in the study of H I proximity zones at $z \sim 6$ (Fan et al. 2006b; Carilli et al. 2010; Bolton & Haehnelt 2007a; Lidz et al. 2007). Specifically, following the work of Fan et al. (2006b), these studies smooth the spectra by a Gaussian filter with FWHM = 20Å in the observed frame, which corresponds to a velocity interval $\Delta v \sim 700$ km s^{-1} or proper distance $R_{\rm prop} \simeq 0.97$ Mpc. We adopt the same value of the smoothing scale in proper units $R_{\rm prop}^{z=3.9} = 0.97$ Mpc, which corresponds to a comoving scale of $R_{\rm com} = 4.75$ cMpc

at $z = 3.9$, or a velocity interval $\Delta v \sim 410\,\mathrm{km\,s^{-1}}$. This is approximately twice the FWHM of HST/COS (for G140L grating).

Figure 4.9 shows the distribution of the proximity zone sizes determined in this way measured from a set of 1000 skewers for the two models shown in Figure 4.8 whose stacked spectra were degenerate. Given the large degree of overlap between the histograms for these two models, and the relatively small number $\simeq 8$ of $z \gtrsim 3.5$ quasars with HST/COS spectra it is clear that it will be extremely challenging to measure the value of quasar lifetime or He II background using this definition of the proximity zone size. In § 4 we discussed how density fluctuations also introduce scatter in the distribution of the proximity zone sizes and thus complicate our ability to infer parameters (see Figure 4.1). We conclude that this statistical approach of measuring the sizes of He II proximity zones does not result in higher sensitivity to the properties of quasars or the IGM parameters at high redshift $z \sim 4$.

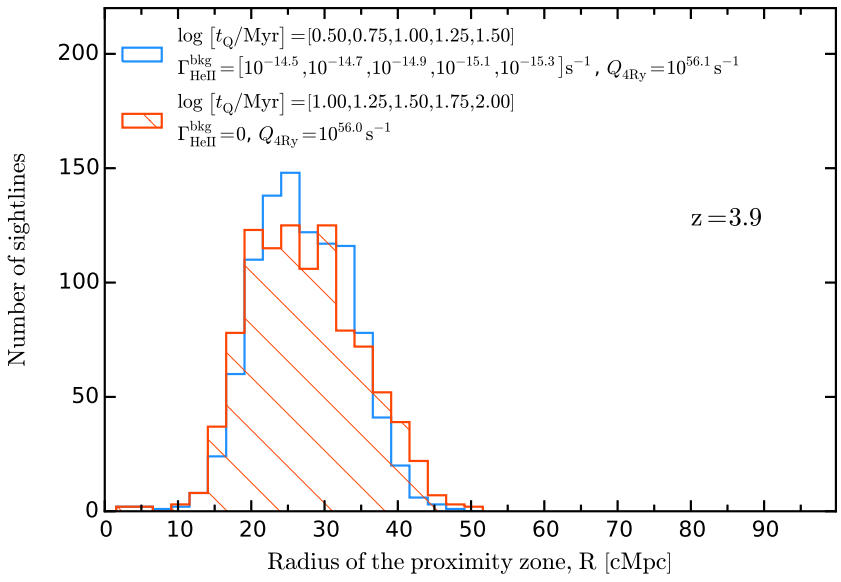

FIGURE 4.9: *Distribution of the He II proximity zone sizes measured from radiative transfer calculations on* 1000 *skewers. The models are the same as in Figure 4.8. The size of the proximity zone is defined as the location where the smoothed spectra crosses the threshold* $F = 0.1$ *(see text for details). The overlap of the histograms makes it impossible to precisely distinguish one model from another.*

4.6 SUMMARY

We have illustrated that IGM density fluctuations result in significant dispersion in the sizes and properties of the He II proximity zone, making it difficult to isolate parameter dependencies. In order to eliminate this source of variation, we investigated stacking proximity zones for ensembles of quasars.

We have used the new model described in Chapter 3 to understand how the He II proximity zone' properties reflect the dependencies of the stacked transmission profiles on quasar lifetime $t_{\rm Q}$, He II ionizing background $\Gamma^{\rm bkg}_{\rm HeII}$, and the photon production rate $Q_{\rm 4Ry}$, and the degeneracies between these parameters. The approach to ionization equilibrium in the proximity zone is set by the equilibration timescale, which is the inverse of the local photoionization rate $t_{\rm eq} \simeq \Gamma^{-1}_{\rm tot}$. We have shown that for an IGM in which Helium is already highly doubly ionized, which is likely to be the case at $z = 3.1$, the maximum value of the quasar lifetime that one can probe is $t^{\rm max}_{\rm Q} \simeq 1/\Gamma^{\rm bkg}_{\rm HeII} \simeq 2.5 \times 10^7$ yr, which is comparable to the Salpeter time.

As we showed in Chapter 3, the degeneracy which exists between quasar lifetime and He II background can be broken at $z \simeq 3$, therefore the stacked transmission profiles at this redshift can be used to determine the quasar lifetime. The results of our simulations at $z \simeq 4$ also imply that it will be extremely challenging to use the analogous He II proximity zones at higher redshifts to put constraints on either quasar lifetime or ionization state of the IGM due to unknown He II effective optical depth and uncertainties in the quasar spectral energy distribution.

Chapter 5

Thermal Proximity Effect

"Whether you can observe a thing or not
depends on the theory which you use.
It is the theory which decides what
can be observed.."
Albert Einstein

As discussed in Section 1.3, recent measurements of the He II Lyα effective optical depth in the spectra $2.7 \lesssim z \lesssim 3.5$ quasars (Shull et al. 2010; Worseck et al. 2011; Syphers & Shull 2013, 2014; Worseck et al. 2014; Worseck in prep.) indicate that He II reionization has been mostly completed by $z \simeq 2.7$, $\tau_{\rm eff}^{\rm HeII} \simeq 2-3$. However, the same observations have detected a large number of low optical depth regions with $\tau_{\rm eff}^{\rm HeII} \simeq 3-5$ at $z \gtrsim 3.5$, yielding $x_{\rm HeII} \simeq 2-5\%$ (see discussion in section 3.1). These results suggest that sources of He II ionizing photons should be present in the IGM at $z \gtrsim 4$ in order to significantly doubly ionize intergalactic medium by $z \simeq 3.5$ (at least in some regions), which goes against the predictions of current state-of-the-art simulations of the late He II reionization (McQuinn et al. 2009a; Compostella et al. 2013, 2014). Additional motivation for an early He II reionization is given by the possible discovery of previously undetected population of faint quasars at $4 \lesssim z \lesssim 6$ (Giallongo et al. 2015). In this context, Madau & Haardt (2015) explored the possibility that quasars alone are responsible for reionization of both hydrogen and helium. Their model is, indeed, consistent with an early He II reionization at $z \simeq 4.2$. Unfortunately, this prediction is very hard to probe observationally. As mentioned in Section 1.3, the intergalactic He II Lyα absorption in the spectra of

quasars offers the only direct method to study the He II reionization. Sadly, these observations are very ambiguous at redshifts $z_{\rm em} \gtrsim 4$ due to the sensitivity limit of HST/COS and the general lack of sufficiently bright in far-UV quasars at $z \gtrsim 4$. Thus, another method is needed to constrain the duration of He II reionization at $z \gtrsim 4$.

In this Chapter we investigate an alternative indirect way to constrain the phases of He II reionization and the lifetime of quasars simultaneously. The temperature of the intergalactic medium is strongly connected to the reionization history. First, when the ionization fronts traversed through and reionized the intergalactic hydrogen at $z \lesssim 6$ the IGM temperature increased to $T \approx 2 \times 10^4$ K (Miralda-Escudé & Rees 1994; McQuinn 2012). Similar, the IGM was heated up by $\Delta T \approx 5 - 10 \times 10^3$ K during the He II reionization (Hui & Haiman 2003; Furlanetto & Oh 2008; McQuinn et al. 2009a; Haardt & Madau 2012; Bolton et al. 2012; Compostella et al. 2013; Puchwein et al. 2015; Upton Sanderbeck et al. 2015), and because the cooling time of the low density intergalactic gas is long, the IGM preserves the information about the duration and morphology of the reionization events. A variety of methods has been used in the past to access this information contained in the observed high-resolution spectra of high-redshift quasars, including the direct fitting of the widths of H I Lyα absorption lines (Schaye et al. 2000; Ricotti et al. 2000; McDonald et al. 2001; Bolton et al. 2014), measurements of the probability density function of the transmitted flux, wavelet analysis of H I Lyα forest (Theuns et al. 2002; Lidz et al. 2010), estimates of the curvature of the 1D power spectrum (Becker et al. 2011; Boera et al. 2014, 2015), and 1D and 3D power spectrum measurements of the transmitted flux (Zaldarriaga et al. 2001; Kim et al. 2007; Bolton et al. 2008; Viel et al. 2009; Lukić et al. 2015; Lee et al. 2015). The majority of these works detected elevated IGM temperatures at $3 \lesssim z \lesssim 4$, explained as the effect of He II reionization.

This photoheating during He II reionization is expected to have a significant effect on the spectra of high-redshift quasars, the so-called *thermal proximity effect*. It describes the thermal broadening and smoothing of the absorption lines in the H I and He II Lyα spectra produced by the quasar ionization fronts traversing through the surrounding intergalactic medium and boosting its temperature (Miralda-Escudé & Rees 1994; Theuns et al. 2002; Meiksin et al. 2010; Meiksin & Tittley 2012; Bolton et al. 2012). Recently, it has been shown (Bolton et al. 2009; Meiksin et al. 2010) that during He II reionization the temperature evolution in the intergalactic medium surrounding the quasar is driven by the evolution of the He II fraction in response to the quasar radiation. Herein, the intervening medium hardens the radiation field, producing a distinct radial trend in the temperature evolution profiles. Further, it is easy to show that, similar to H I and He II proximity zones, the size of the region experiencing an elevated temperatures due to the quasar activity depends on the quasar lifetime. For instance, Bolton et al. (2012) have performed the first measurements of the IGM temperatures in the vicinity of $z \sim 6$ quasars, finding the strong correlation

with the quasar lifetime. Using the thermal proximity effect as a probe of the temperatures they have constrained the lower limit of quasar activity to be $t_{\rm Q} \gtrsim 10^7$ yr. Meiksin et al. (2010), however, showed that the influence of the thermal proximity effect on the properties of the individual H I and He II Lyα absorption lines can be hard to distinguish from the effect of the intrinsic peculiar motions of the gas and fluctuations of the underlying density field. Therefore, the detailed hydrodynamical and radiative transfer simulations are required to disentangle these two effects.

The aim of this Chapter is to investigate the properties of the thermal proximity effect and determine if it can be used not only to put constraints on the duration of the He II reionization, but also to infer the duration of the quasar episodic lifetime. We perform detailed cosmological hydrodynamical simulations at $z \simeq 4$ and the post-processing radiative transfer simulations using the algorithm described in Chapter 2. In what follows we analyze the results of numerical simulations in the framework of our model for time evolution of He II fraction (see Chapter 3). Instead of the direct line-fitting technique used by Meiksin (2009) we propose a new method to constrain the quasar lifetime and fraction of singly ionized helium based on the power spectrum statistics.

5.1 TEMPERATURE EVOLUTION

First, consider an element of ideal gas in the expanding Universe exposed to the quasar radiation. The temperature T of the gas element then evolves with time t according to (see Hui & Gnedin 1997)

$$\frac{{\rm d}T}{{\rm d}t} = -2HT + \frac{2T}{3\,(1+\delta)}\frac{{\rm d}\delta}{{\rm d}t} - \frac{T}{\Sigma_i X_i}\frac{{\rm d}\Sigma_i X_i}{{\rm d}t} + \frac{2}{3k_{\rm B}n_{\rm b}}\frac{{\rm d}Q}{{\rm d}t} \tag{5.1}$$

where H is the Hubble parameter and $n_{\rm b}$ is the number density of the baryonic particles, and $k_{\rm B}$ is the Boltzmann constant.

The first three terms on the right-hand side of eqn. (5.1) correspond to adiabatic cooling due to the expansion of the Universe, cooling or heating from formation of the structure and change in the internal energy of the gas (due to the change in the number density of particles), respectively. The last term represents the amount of heat gained (lost) per unit volume from radiation processes. Because the cooling timescale for the low density IGM is, effectively, the Hubble time $t_{\rm H}$, the first term can be omitted as long as we consider quasar lifetimes $t_{\rm Q} \ll t_{\rm H}$. This is clearly the case, since we consider quasar lifetimes in range 10^6 yr $\lesssim t_{\rm Q} \lesssim 10^8$ yr and the Hubble time at $z = 3.9$ is $t_{\rm H} \simeq 2 \times 10^9$ yr. The contribution from the second and third

terms is small in comparison to the photoheating, described by the last term on the right-hand side of eqn. (5.1). Thus, they can also be neglected in the context of this work. Finally, assuming that hydrogen and helium are already (singly) ionized, we can approximate eqn. (5.1) by

$$\frac{\mathrm{d}T}{\mathrm{d}t} \simeq \frac{2}{3k_{\mathrm{B}}n_{\mathrm{b}}}\frac{\mathrm{d}Q}{\mathrm{d}t} = \frac{2}{3k_{\mathrm{B}}n_{\mathrm{b}}}n_{\mathrm{HeII}}\epsilon_{\mathrm{HeII}} \tag{5.2}$$

where n_{HeII} is the number density of He II atoms and ϵ_{HeII} is the total quasar photoheating rate, which in our radiative transfer algorithm is given by

$$\epsilon_{\mathrm{HeII}} = \int_{\nu_{\mathrm{th}}}^{\infty} N_{\nu}\sigma_{\nu}\mathrm{e}^{-\langle\tau_{\nu}\rangle}\left(1-\mathrm{e}^{-\langle\delta\tau_{\nu}\rangle}\right)(h_{\mathrm{P}}\nu - h_{\mathrm{P}}\nu_{\mathrm{th}})\,\mathrm{d}\nu \tag{5.3}$$

It is easy to show that in case of photoionization equilibrium and given that the recombination timescale is very long ($t_{\mathrm{rec}} \simeq 10^9$ yr) eqn. (5.2) becomes

$$\frac{\mathrm{d}T}{\mathrm{d}t} \simeq \frac{2}{3k_{\mathrm{B}}n_{\mathrm{b}}}\frac{\mathrm{d}n_{\mathrm{HeII}}}{\mathrm{d}t}\frac{\epsilon_{\mathrm{HeII}}}{\Gamma^{\mathrm{tot}}_{\mathrm{HeII}}} \tag{5.4}$$

We can also describe the n_{HeII} rate of change $\mathrm{d}n_{\mathrm{HeII}}/\mathrm{d}t$ in terms of He II fraction x_{HeII} as

$$\frac{\mathrm{d}n_{\mathrm{HeII}}}{\mathrm{d}t} = \frac{\rho_{\mathrm{crit}}\Omega_{\mathrm{b}}}{m_{\mathrm{p}}}\frac{Y_{\mathrm{He}}}{4}(1+\delta)(1+z)^3\frac{\mathrm{d}x_{\mathrm{HeII}}}{\mathrm{d}t} \tag{5.5}$$

where ρ_{crit} is the critical density of the Universe, m_{p} is the mass of proton, and $(1+\delta) = \rho/\bar{\rho}$ is the gas density in units of the cosmic mean density. Finally, combining eqn. (5.4) and eqn. (5.5) and taking into account that the total number density of baryons is $n_b = n_{\mathrm{H}} + n_{\mathrm{He}} + n_{\mathrm{e}}$ (number density of hydrogen and helium atoms, and electrons) the temperature evolution is given by

$$\frac{\mathrm{d}T}{\mathrm{d}t} \simeq \frac{2}{3k_{\mathrm{B}}}\frac{Y_{\mathrm{He}}}{4\,(2-5Y_{\mathrm{He}}/4)}\frac{\mathrm{d}x_{\mathrm{HeII}}}{\mathrm{d}t}\langle E\rangle \tag{5.6}$$

where $\langle E\rangle = \epsilon_{\mathrm{HeII}}/\Gamma^{\mathrm{tot}}_{\mathrm{HeII}}$ is the average excess energy per photoionization of He II atom given by eqn. (2.14).

Eqn. (5.6) is solved at each time step of our 1D radiative transfer simulations for which we make the following assumptions: first, we ignore secondary collisional ionizations and assume that all excess energy from photoionizations of He II ions is converted into the heat, second, we also neglect the heating generated by the He II

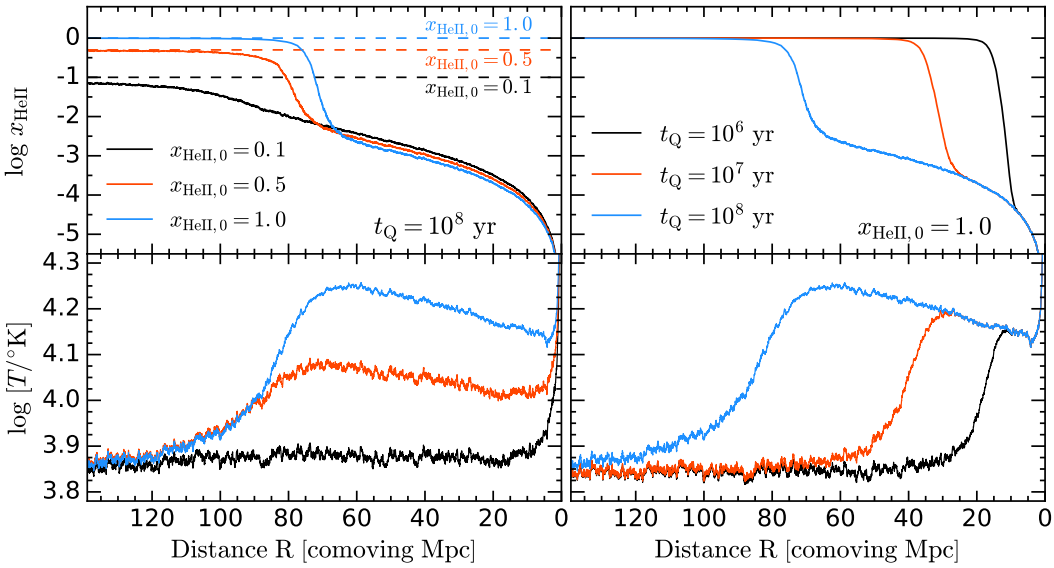

FIGURE 5.1: *Thermal evolution of the intergalactic medium around the quasar in different radiative transfer simulations. The upper panels show the evolution of the median fraction of singly ionized helium* $x_{\rm HeII}$*, while the bottom panels illustrate the evolution of the median temperature of the IGM.* Left side panels *show thermal evolution of the IGM as a function of initial He II fraction at a fixed quasar lifetime* $t_{\rm Q} = 10^8$ *yr. Whilst* right side panels *show thermal evolution of the IGM as a function of different values of quasar lifetime while keeping fixed initial He II fraction* $x_{\rm HeII,0} = 1.0$*. The dashed lines in the upper left panel indicate the values of initial He II fraction* $x_{\rm HeII,0}$ *in three different models. All median profiles are computed from* 1000 *simulated skewers.*

ionizing background, since this is accounted for via the photoionization heating in the hydrodynamical simulations (and it does not depend on the normalization of the photoionizing background, which we freely adjust). For a given SED (eqn. (2.1)) of the quasar the integral of the average excess energy per ionization $\langle \Delta E \rangle$ is calculated analytically at each time step.

The resulting evolution of the IGM temperature around the quasar from our radiative transfer simulations is shown in Figure 5.1 with upper panels illustrating the evolution of the median He II fraction $x_{\rm HeII}$ and bottom panels showing the median IGM temperature T, calculated from 1000 skewers in several distinct models. The left-side panels show the evolution of these parameters as a function of initial He II fraction $x_{\rm HeII,0}$ (set be the He II ionizing background prior to quasar activity, see Chapter 3) while keeping the quasar lifetime fixed to $t_{\rm Q} = 10^8$ yr. Whereas, the right-side panels illustate models with three different values of quasar lifetime $t_{\rm Q}$ and the initial fraction of singly ionized helium fixed to $x_{\rm HeII,0} = 1.0$. The several trends are immediately apparent from Figure 5.1.

IGM temperature: dependence on quasar lifetime

In Chapter 3 we have shown that the size of the He II proximity zone, where the initial fraction of singly ionized helium $x_{\rm HeII,0}$ is greatly reduced by the quasar ionization front sweeping across the IGM, depends strongly on the quasar lifetime $t_{\rm Q}$. The same dependence is shown by the temperature profiles in the bottom right panel of Figure 5.1. One can see that variations in quasar lifetime $t_{\rm Q}$ change the characteristic size of the region of the IGM around the quasar influenced by the elevated temperatures. This is because for longer lifetimes (e.g., $t_{\rm Q} = 10^8$ yr) the quasar ionization front travels much further into the IGM, boosting the IGM temperature by $\Delta T \simeq 0.3 - 0.4$ dex (in case of $x_{\rm HeII,0} = 1.0$). In contrast, the quasar ionization front has not yet reached the same distance in short lifetime model (e.g., $t_{\rm Q} = 10^6$ yr), for which the size of the region with increased temperature is ≈ 5 times smaller. In other words, the longer the IGM has been exposed to the quasar radiation, the larger the radial extent of the thermal proximity effect. At the same time the amplitude of these changes has only a modest dependence on the value of quasar lifetime.

IGM temperature: dependence on initial He II fraction

Furthermore, the left-side panels of Figure 5.1 indicate that the resulting IGM temperature in the quasar proximity zone also depends significantly on the amount of singly ionized helium, $x_{\rm HeII,0}$. It is apparent that if the initial fraction of singly ionized helium was $x_{\rm HeII,0} = 1.0$ (blue curve), the hard photons of quasar radiation are absorbed by the IGM and the median temperature is boosted by $\Delta T \simeq 0.3 - 0.4$ dex, whereas there is no significant change in temperature if helium has been already highly doubly ionized ($x_{\rm HeII,0} = 0.1$) before quasar turned on (black curve). According to eqn. (5.6) the amount of heat injected into the IGM is proportional to the rate of change of the He II fraction. This is because if the initial He II fraction is already low, then quasar radiation does not significantly change the ionization state of the gas because hardly any hard photons are absorbed. Thus, in contrast to the effect of quasar lifetime, the value of initial He II fraction does not change the extent of thermal proximity effect, but rather sets the amplitude of the elevated IGM temperature in quasar proximity zone.

Filtering of the radiation by the IGM

In addition, one can also see that for fixed values of initial He II fraction and quasar lifetime the amount of heat input into the IGM is larger at larger distances from the quasar. This happens because the IGM effectively filters the intrinsic quasar radiation, which results in the hardening of the ionizing radiation field (McQuinn et al. 2009a; Bolton et al. 2009; Meiksin et al. 2010). Recall eqn. (5.6), which shows that the amount of heat input over the time-step t is proportional to the average excess

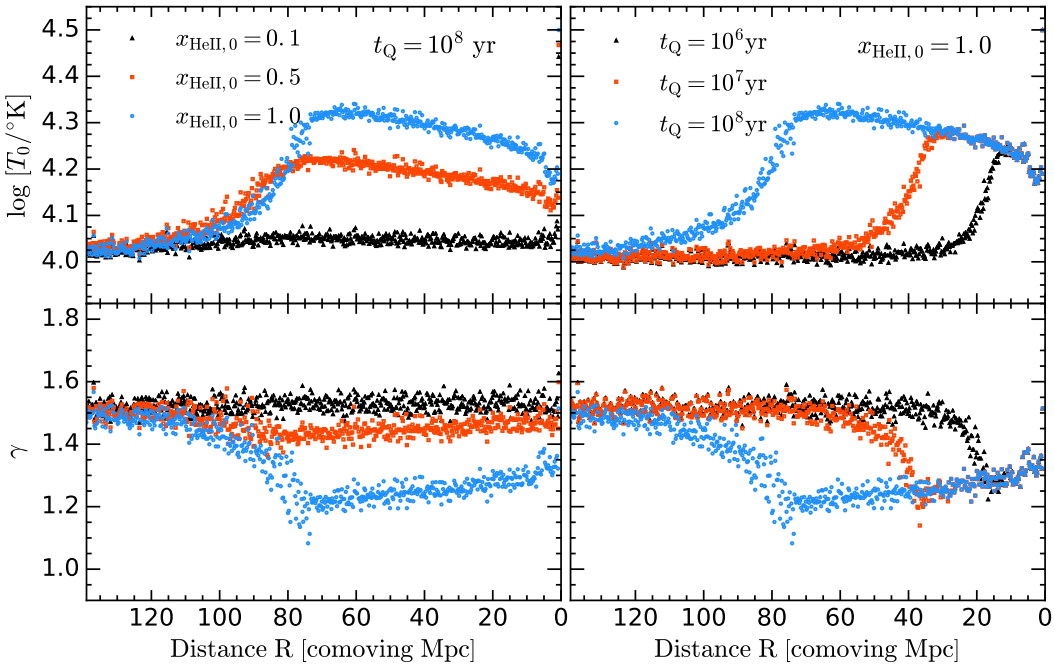

FIGURE 5.2: *Parameters of the temperature-density relation: temperature at mean density T_0 and the power-law index γ, for the same set of radiative transfer simulations as in Figure 5.1.*

energy $\langle E \rangle$. The mean free path of He II ionizing photons scales as $\lambda_{\rm mfp} \propto \nu^3$ and therefore photons with energies $E_{\rm ion} = h\nu \simeq 4$ Ry have a short mean free path. They are preferably absorbed by the intergalactic medium instantly in the vicinity of quasar leading to a very small gain in $\langle E \rangle$. On the other hand, the high-energy photons can travel much further into the intergalactic medium before getting absorbed, due to sufficiently longer mean free path. They, thus, inject more heat at larger distances from the quasar.

Temperature-Density relation

An interplay between the metagalactic ionizing radiation which heats up the IGM and the expansion of the Universe which adiabatically cools the IGM produces a tight relation between temperature and density of the gas which can be approximated by a power-law $T = T_0 \Delta_{\rm b}^{\gamma-1}$ (for $\Delta_{\rm b} \leq 10$) , where T_0, $\Delta_{\rm b} = \rho/\bar{\rho}$ and γ are the gas temperature at mean density, gas overdensity in units of critical density, and the power-law index, respectively. Although with some scatter, typically assumed values for T_0 are on the order of $\simeq 10^4$ K and the power-law index naturally asymptotes to $\gamma \approx 1.6$ (Miralda-Escudé & Rees 1994; Hui & Gnedin 1997).

It is expected that He II reionization will significantly change the $T - \Delta_{\rm b}$ relation

(McQuinn et al. 2009a; Compostella et al. 2013). In order to check how the quasar radiation affects this relation we fit the distribution of densities and temperatures in each pixel along 1000 sightlines with the power-law to calculate T_0 and γ. To reduce the fluctuation scatter we also calculate the mean T_0 and γ in bins of 20 pixels, which corresponds to $\Delta R \simeq 0.25$ cMpc. The results are shown in Figure 5.2, where we used the same models illustrated in Figure 5.1. As one might expect the evolution of T_0 and γ closely follows the evolution of the median temperature of the IGM and reflects the dependencies on He II fraction and quasar lifetime described previously. The main effect of quasar radiation on the temperature-density relation in the low density IGM is twofold. First, the intergalactic medium becomes much hotter due to additional heat injected by the quasar ionization front traversing through the IGM, which is reflected by the increase in T_0. Second, during He II reionization, the $T - \Delta_b$ relation flattens in the quasar proximity zone with power-law index γ deviating from the asymptotic value $\gamma \approx 1.5 - 1.6$ towards the isothermal value of $\gamma = 1$. As illustrated previously, the exact amplitude and extent of these changes strongly depend on the value of the initial He II fraction and quasar lifetime. Thus is again shown by different curves in Figure 5.2.

* * *

To summarize, we investigated the connection between the radial evolution of the median IGM temperature and the initial He II fraction $x_{\rm HeII,0}$, as well as the quasar lifetime $t_{\rm Q}$. We illustrated that the radial extent of the elevated IGM temperatures probes the quasar lifetime, whereas the amplitude of the temperature boost is set by the amount of singly ionized helium in the IGM prior to quasar turning on. Therefore, the presence of the increased IGM temperatures around quasars, i.e. thermal proximity effect, can be used to constrain both of these parameters and ultimately determine the redshift at which He II reionization has occurred. In what follows we describe a method to detect the thermal proximity effect.

5.2 LINE-OF-SIGHT POWER SPECTRUM STATISTICS

Among other methods used to study thermal evolution of the IGM (see discussion in the beginning of this Chapter 5) the Lyα forest flux power spectrum is the most sensitive probe of the temperature fluctuations. This is due to the fact that thermal Doppler broadening affects the properties of the H I and He II Lyα forest in quasar spectra and results in the prominent small-scale cut-off in the power (McDonald et al. 2000; Zaldarriaga et al. 2001; Croft et al. 2002; Viel et al. 2009). Unfortunately,

the number of observed He II Lyα absorption spectra of high-redshift quasars is very small ($N \simeq 30$) and sensitivity limit of HST/COS complicates our ability to obtain more information at $z \gtrsim 3.5$. However, the H I Lyα forest provides similar sensitivity to the fluctuations of the IGM temperature and, in contrast to the He II Lyα forest, is accessible at all redshifts $z \lesssim 5$, after H I reionization is presumably completed. Therefore, in what follows we propose to use H I Lyα forest to detect thermal proximity effect and constrain the He II fraction $x_{\rm HeII}$ and quasar lifetime $t_{\rm Q}$.

Fluctuations of the flux along the line-of-sight can be described as

$$\delta F\left(x\right) = \frac{F\left(x\right)}{\bar{F}} - 1 \tag{5.7}$$

where $F\left(x\right) = \exp\left(-\tau\right)$ is the transmitted flux in each pixel x of the skewer with optical depth τ, and $\bar{F}$ is the mean flux in a given volume, for which we adopt $\bar{F} = 0.425$ consistent with measurements of Becker & Bolton (2013) at redshift $z = 3.9$. The 1D power spectrum of Lyα forest $P\left(k\right)$ is then given by

$$P\left(k\right) = \langle|\delta\tilde{F}\left(k\right)|^2\rangle_N \tag{5.8}$$

where $\delta\tilde{F}\left(k\right)$ corresponds to the Fourier transformation of δF for a given wavenumber k, and angular brackets denote the averaging over total ensemble of skewers N. We also adopt the common convention and use the dimensionless power spectrum $\pi^{-1}kP\left(k\right)$.

Recall Figure 5.1 where we showed that the amplitude and the extent of the thermal proximity effect around the quasar has a strong radial dependence due to effect of quasar lifetime. Therefore, the properties of the H I Lyα forest will be a function of quasar lifetime $t_{\rm Q}$, initial He II fraction $x_{\rm HeII,0}$ and distance R from the quasar. Our approach is therefore to calculate the average H I Lyα forest power spectrum of a sample of quasars (we use a total number of $N = 1000$ simulated H I Lyα spectra.) in bins of $\Delta R = 10$ cMpc and to compare the results with the power spectra from the control region far away from the quasar. The high-temperature shocked gas near the quasar host halo may complicate our calculations and, thus, we also exclude first 3 cMpc closest to the location of the quasar. Following the algorithm described in Section 2.2.1, we calculate the quasar He II-ionizing photon production rate $Q_{\rm 4Ry}$ from the sample of $z \simeq 4$ quasars with median i-band magnitude $i = 18$, yielding $Q_{\rm 4Ry} = 10^{56.5}{\rm s}^{-1}$. This fiducial value is fixed in all models discussed in what follows.

5.2.1 SENSITIVITY TO QUASAR LIFETIME

First, we use our method to investigate the sensitivity of the average H I Lyα power spectra to the value of quasar lifetime. We calculate three different models with $t_{\rm Q} = 10^6$ yr, $t_{\rm Q} = 10^7$ yr, and $t_{\rm Q} = 10^8$ yr, while the value of the initial He II fraction is fixed to $x_{\rm HeII,0} = 1.0$. The left columns of Figure 5.3 show simulated individual H I Lyα spectra and temperature profiles in the proximity zone for these three models, calculated in three different R-bins, while the right column illustrates the corresponding H I Lyα power spectra in the same R-bins. We also show the difference ΔP in each R-bin between the power spectrum of $t_{\rm Q} = 10^8$ yr model and other models divided by the the simulated bootstrap error $\sigma_{\rm data}$ for the sample of $N = 50$ spectra taken from $t_{\rm Q} = 10^8$ yr model. There are several trends that are immediately apparent from Figure 5.3.

First, the time required by the ionization front to reach the bin closest to the quasar ($R = 3 - 13$ cMpc) is less than quasar lifetime values in all three model. Thus, very close to the quasar the amplitude of the temperature boost is the same independent of the actual value of quasar lifetime. Hence, the resulting H I Lyα forest and temperature profiles of three models with different quasar lifetime values are indistinguishable in this bin. Consequently, the average power spectra of these models are identical. However, as one goes further away from the quasar the difference between power spectra increases.

It is apparent that at an intermediate bin $R = 43 - 53$ cMpc the Lyα spectra and temperature profiles of the three models differ significantly. For the longest lifetime model the quasar ionization front has already traversed this distance and boosted the median IGM temperature by $\Delta T \approx 0.3 - 0.4$ dex (see Figure 5.1), whereas it has not yet reached this distance in models with shorter quasar lifetime ($t_{\rm Q} = 10^7$ yr and $t_{\rm Q} = 10^6$ yr). Thus, the temperature of this region of IGM is lower in these models, than in $t_{\rm Q} = 10^8$ yr model. This difference in the IGM temperature produces different amounts of thermal broadening in the Lyα forest, that is why the H I Lyα forest of the longest lifetime model becomes smoother and contains less saturated absorption features, than H I Lyα spectra of cooler models. Accordingly, the power spectrum of the $t_{\rm Q} = 10^8$ yr models indicates a decreased signal at small scales (large values of k), which was washed away by the thermal broadening and converted into the signal at large scales (smaller values of k). There is considerably more signal at small scales ($k \gtrsim 0.1$ km^{-1}s) in models with shorter quasar lifetimes. Withal, the difference between the power spectra in this R-bin, which is illustrated in the bottom subpanel, shows that these models should be easily distinguishable.

Finally, far away from the quasar at $R \simeq 93 - 103$ cMpc the difference between

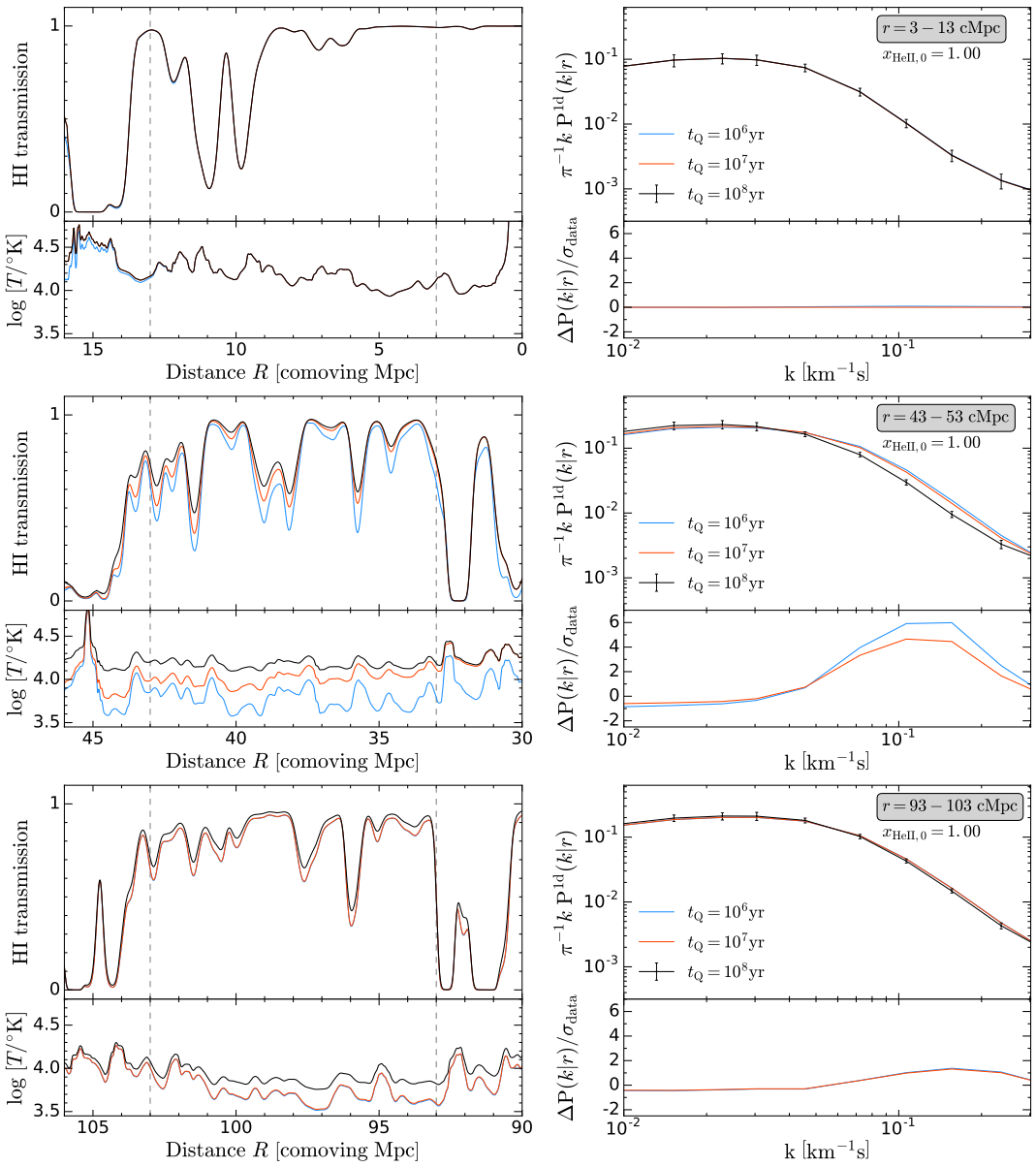

FIGURE 5.3: *Sensitivity of the H I Lyα forest power spectrum statistics to the value of quasar lifetime. Each row corresponds to the different R-bin from the quasar. Left column illustrates the simulated individual H I Lyα spectra (top) and IGM temperature profiles (bottom) for three models with* $t_{\rm Q} = 10^6$ *yr (blue),* $t_{\rm Q} = 10^7$ *yr (red) and* $t_{\rm Q} = 10^8$ *yr (black). The value of initial fraction of singly ionized helium is fixed to* $x_{\rm HeII,0} = 1.0$ *in all models. Right column shows the average H I Lyα power spectra (top subpanels) of the same models. Bootstrap simulated errors are shown on the black curve for the sample of* 50 *spectra. The difference between the power spectrum of* $t_{\rm Q} = 10^8$ *yr model and the other models divided by the simulated error (see text for explanation) is shown in the bottom subpanels.*

the power spectra of all three models diminishes again because there was not enough time for the quasar ionization front to reach this distance and significantly change the temperature of the IGM. Therefore, the structure of the H I Lyα forest experiences almost the same amount of thermal broadening for considered models with $t_{\rm Q} \lesssim 10^8$ yr.

5.2.2 SENSITIVITY TO INITIAL HE II FRACTION

Similarly, we now investigate the sensitivity of the line-of-sight Lyα power spectrum statistics to the variations of the initial He II fraction. Akin to the discussion the in previous section we create three radiative transfer simulations, each with different value of the initial He II fraction $x_{\rm HeII,0} = 0.05$, $x_{\rm HeII,0} = 0.50$, and $x_{\rm HeII,0} = 1.00$. The quasar lifetime is fixed to $t_{\rm Q} = 10^8$ yr. Figure 5.4 illustrates the resulting H I Lyα transmission, IGM temperature profiles and power spectra of these models in the same R-bins.

In Section 5.1 we showed that the initial He II fraction establishes the overall amplitude of the thermal proximity effect (see left panels of Figure 5.1). Thus, one naturally expects to see significant differences in the properties of the H I Lyα forest and its power spectrum between models with very different values of $x_{\rm HeII,0}$. Indeed, one can see from the left column of Figure 5.4 that the temperature of the IGM significantly differs between the considered models. As expected, the maximum amount of photoheating due to ionization of singly ionized helium atoms is gained in $x_{\rm HeII,0} = 1.00$ model (black). On the contrary, as explained in Section 5.1 the temperature of the IGM hardly changes if helium is predominantly highly doubly ionized before quasar turns on ($x_{\rm HeII,0} = 0.05$, blue curve). Analogous to the discussion in Section 5.2.1, this difference in the photoheating results in different amount of thermal broadening of the H I Lyα forest, therefore affecting the power spectra of the models, i.e. decreasing the small-scale power in the hotter model ($x_{\rm HeII,0} = 1.00$) in comparison to the cooler one ($x_{\rm HeII,0} = 0.05$).

Interestingly, the difference between the power spectra of the hotter and cooler models increases from the bin closest to the quasar ($R = 3 - 13$ cMpc) to the intermediate bin ($R = 43 - 53$ cMpc) and then again decreases as one goes to the outskirts of the quasar proximity zone ($R = 93 - 103$ cMpc). This behavior is driven by two effects. First of all, as we noted in Section 5.2.1, the intergalactic medium filters quasar radiation with hard photons injecting more heat at larger distances from the quasar. Therefore, the thermal broadening of the H I Lyα forest in $x_{\rm HeII,0} = 1.00$ model is larger in the intermediate R-bin ($\Delta T \approx 0.3 - 0.4$ dex), than in the closest bin to the quasar ($\Delta T \approx 0.2$ dex). At the same time the IGM temperature (and the

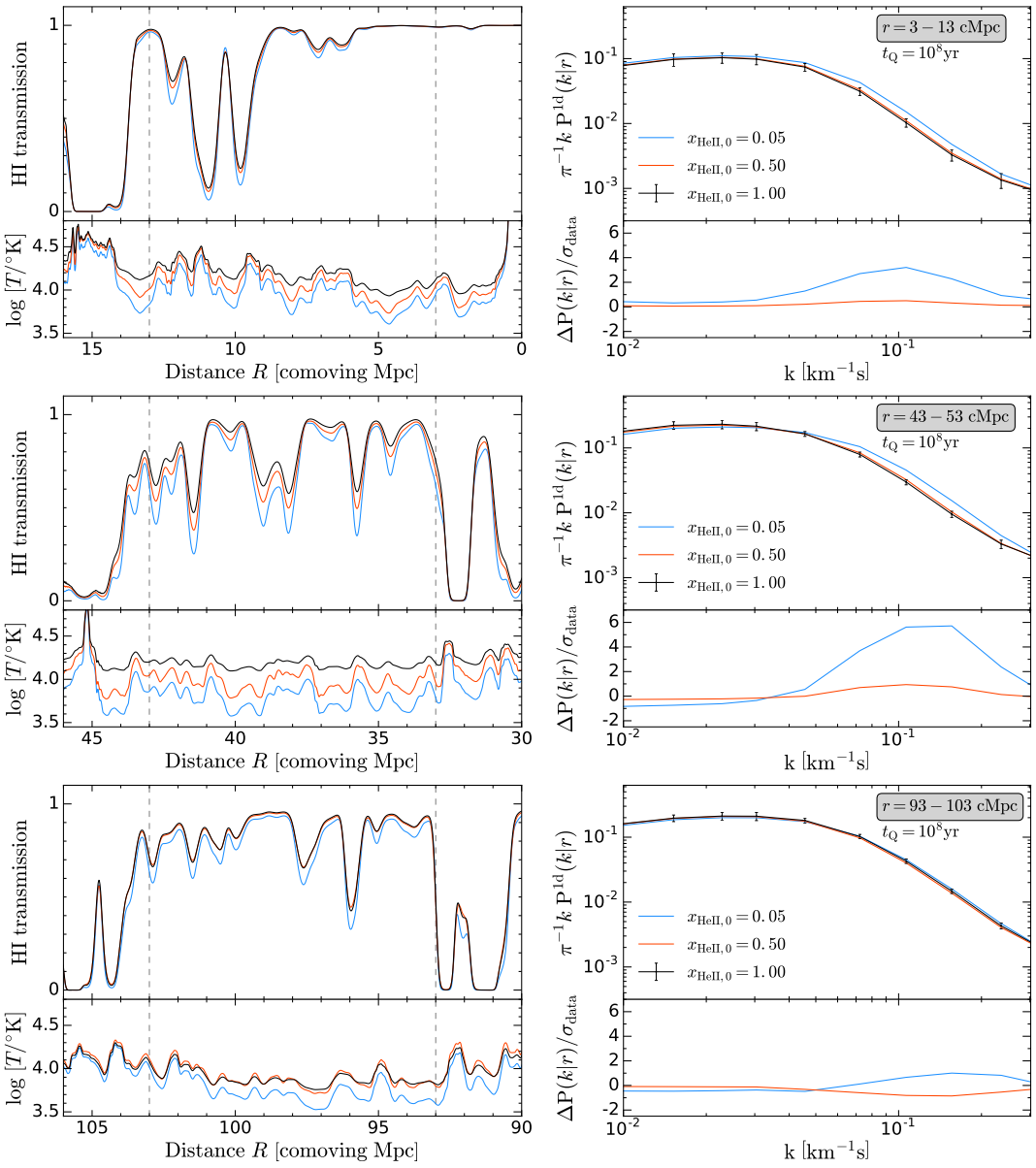

FIGURE 5.4: *Sensitivity of the H I Lyα forest power spectrum statistics to the value of initial He II fraction. Three models are plotted with initial He II fraction* $x_{\rm HeII,0} = 0.05$ *(blue),* $x_{\rm HeII,0} = 0.50$*, and* $x_{\rm HeII,0} = 1.00$*. The lifetime of quasar is fixed in all models to* $t_{\rm Q} = 10^8$ *yr. See Figure 5.3 for the description of the panels.*

power spectrum) in $x_{\rm HeII,0} = 0.05$ model stays constant at all radii. Consequently, the difference between the power spectra of these models increases with increasing distance from the quasar. However, recall that the radial evolution of the temper-

ature depends not only on the value of initial He II fraction, but also on the value of quasar lifetime. Since the quasar lifetime in all models considered here is fixed to $t_{\rm Q} = 10^8$ yr, the temperature of the IGM will be boosted only at distances R to which the quasar ionization front had enough time to travel. Subsequently, after this distance the temperature decreases and asymptotes to the level set before the quasar turned on (see Figure 5.1). Thus, at outer radii the amount of thermal broadening of H I Lyα forest decreases even in the hottest $x_{\rm HeII,0} = 1.00$ model and the difference between the power spectra of different models becomes less dramatic.

* * *

We have demonstrated the sensitivity of the average line-of-sight H I Lyα forest power spectrum to the parameters defining the radial extent and the amplitude of the thermal proximity effect: quasar lifetime $t_{\rm Q}$ and the initial fraction of singly ionized helium $x_{\rm HeII,0}$, which prevailed the IGM before the quasar turned on. We now proceed to the estimate of the accuracy with which we can constrain these parameters applying Bayesian MCMC formalism to the mock sample of high-redshift H I Lyα spectra of realistic size.

5.3 MCMC ANALYSIS: LIKELIHOOD ESTIMATION

We construct a grid of models (1000 skewers per model) with values of initial He II fraction in range $x_{\rm HeII,0} = [0.05 - 1.0]$ and logarithmically spaced quasar lifetimes in range $\log(t_{\rm Q}/{\rm Myr}) = [0.00 - 2.20]$. Further, we choose the *data* sample to be represented by $N = 50$ H I Lyα spectra, which we draw, in this case, from the model with quasar lifetime $t_{\rm Q} = 10^8$ yr and initial He II fraction $x_{\rm HeII,0} = 1.0$. Assuming the multi-variate Gaussian statistics, we can calculate the likelihood of each model on our grid by comparing their average power spectra of $N = 1000$ skewers $P_{\rm model}$ to the average power spectrum of the *data* sample $P_{\rm data}$ in each R-bin. This likelihood is then given by

$$\begin{aligned} \mathscr{L}^{\rm bin}\left(P\left(k\right)|x_{\rm HeII,0}, \log t_{\rm Q}, R\right) &= \left(2\pi\right)^{-{\rm N}/2} \det\left(\Sigma\right)^{-1/2} \\ &\times \exp\left[-\frac{1}{2}\left(P_{\rm data} - P_{\rm model}\right)^{\rm T} \Sigma^{-1} \left(P_{\rm data} - P_{\rm model}\right)\right] \end{aligned} \tag{5.9}$$

where Σ is the covariance matrix of the power spectrum measurement in the corresponding R-bin given by

$$\Sigma\left(k_1, k_2\right) = \langle [P_{\rm data}\left(k_1\right) - P_{\rm model}\left(k_1\right)] \times [P_{\rm data}\left(k_2\right) - P_{\rm model}\left(k_2\right)] \rangle \tag{5.10}$$

We then calculate the full likelihood of each model in the thermal proximity region by multiplying the likelihoods of the corresponding model in each R-bin, yielding

$$\mathscr{L}^{\rm full}\left(P\left(k\right)|x_{\rm HeII,0}, \log t_{\rm Q}\right) = \prod_{i=1}^{\rm M} \mathscr{L}_i^{\rm bin} \tag{5.11}$$

where M = 10 is the number of R-bins used. In order to explore the parameter space $\{\log t_{\rm Q},\ x_{\rm HeII,0}\}$ we then use a standard bivariate spline approximation to interpolate the $\mathscr{L}^{\rm full}$ for any combination of quasar lifetime and initial He II fraction values in our parameter space.

5.4 MCMC ANALYSIS: RESULTS

Having arrived to an expression for the likelihood of each model given by eqn. (5.9) and eqn. (5.11), and being able to evaluate the likelihood in any location of the $\{\log t_{\rm Q},\ x_{\rm HeII,0}\}$ parameter space, we now can explore this likelihood with MCMC calculations to estimate the accuracy with which we can measure the quasar lifetime $t_{\rm Q}$ and initial He II fraction $x_{\rm HeII,0}$ from the sample of $N = 50$ spectra, and examine any possible degeneracies between them. For these purposes we apply the publicly available MCMC algorithm *emcee* presented and described in Foreman-Mackey et al. (2013).

Figure 5.5 shows the constraints on quasar lifetime $t_{\rm Q}$ and initial He II fraction $x_{\rm HeII,0}$ obtained with MCMC calculations for our fiducial *data* sample with $\{t_{\rm Q} = 10^8$ yr, $x_{\rm HeII,0} = 1.0\}$. The contours illustrate the 95% (blue) and 68% (red) confidence levels, respectively. The marginalized posterior distributions of both parameters are plotted in top and right panels of the Figure 5.5. One can see that the recovered distributions of $t_{\rm Q}$ and $x_{\rm HeII,0}$ sharply peak around the fiducial values used in the *data* sample. We analyze each distribution of $t_{\rm Q}$ and $x_{\rm HeII,0}$ by computing the 16th, 50th and 84th percentiles and find that the uncertainties on each of the parameters are remarkably small. In particular, the results of MCMC for this *data* sample are $x_{\rm HeII,0} = 0.92^{+0.053}_{-0.069}$ and $\log\ (t_{\rm Q}/{\rm Myr}) = 1.97 \pm 0.028$, where the central value is the 50th percentile and the quoted uncertainties are the 16th and 84th percentiles of the samples, respectively.

However, this *data* sample is somewhat biased because it reflects, probably, the best

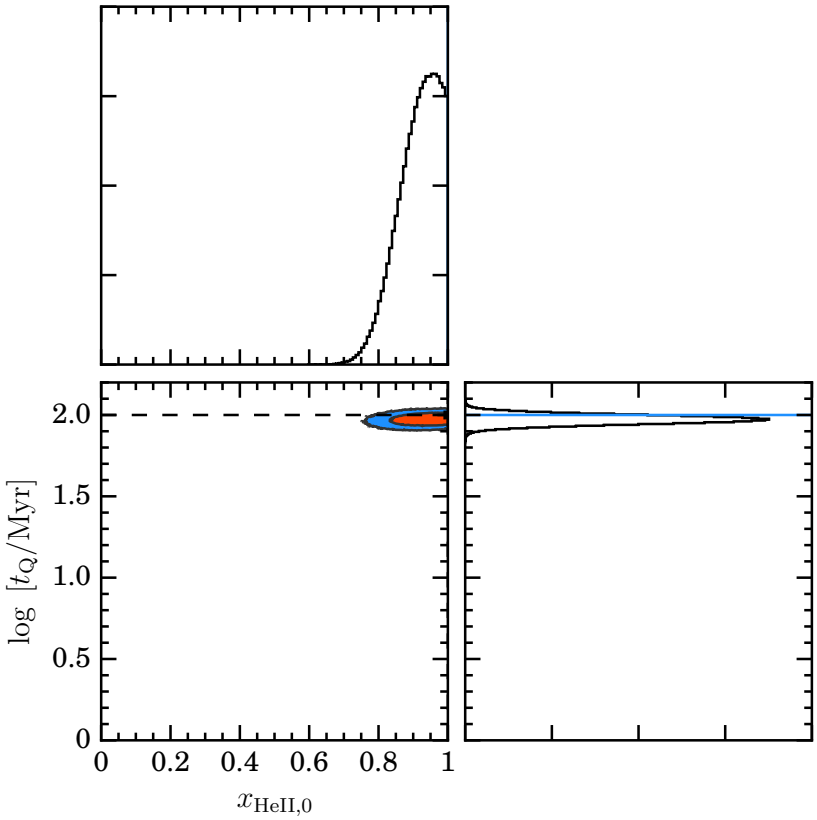

FIGURE 5.5: *Constraints on quasar lifetime and He II fraction from the MCMC analysis. The* 95% *(red) and* 68% *(blue) confidence levels from* 1*D H I Ly*α *power spectrum calculations are shown in the bottom left panel. The top and bottom right panels show the posterior distributions of inferred He II fraction and quasar lifetime, respectively. The dashed lines show the values of lifetime and He II fraction in the sample representing* data*.*

case scenario (among considered here), when the signal in the H I Lyα forest due to the thermal proximity effect is the most prominent, i.e., for initial He II fraction $x_{\rm HeII,0} = 1.0$ and quasar lifetime $t_{\rm Q} = 10^8$ yr the extent and the amplitude of temperature enhancement region are the largest. Thus, the difference between the power spectrum of this sample and the rest of the models will be the largest, helping MCMC calculations to recover the correct values.

We now want to investigate the sensitivity of the MCMC for other *data* samples. Following the algorithm described in § 5.3 we compute the likelihoods of our models given the *data* power spectra now drawn from different models. The results of the MCMC analysis are illustrated in Figure 5.6, where each panel shows the result of the MCMC calculations for a different *data* sample. Each column in Figure 5.6 indicates

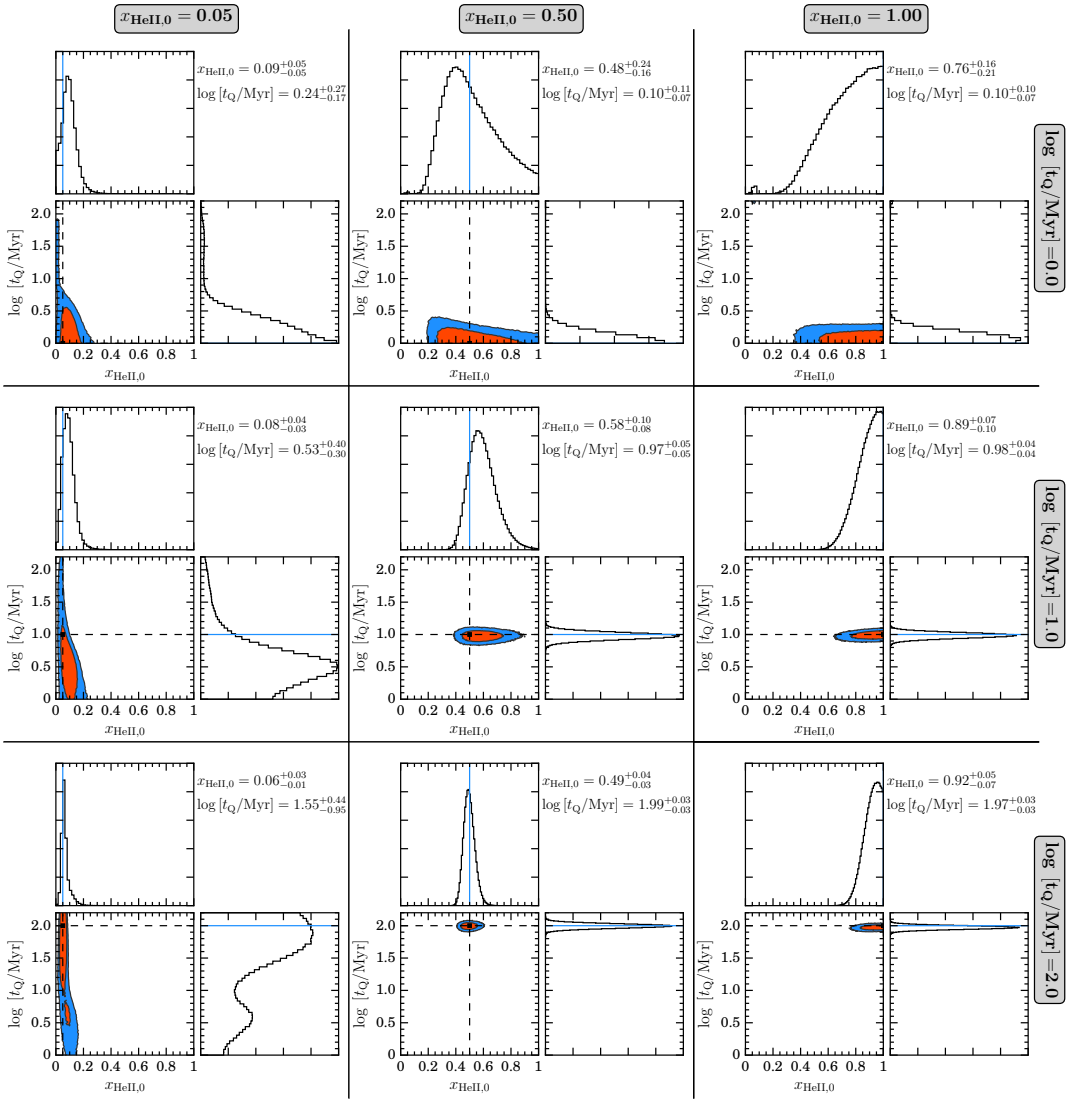

FIGURE 5.6: *Constraints on quasar lifetime and He II fraction from the MCMC analysis. The grey shaded labels on top of each column and on the right side of each row show the values of initial He II fraction and quasar lifetime in the sample of* $N = 50$ *skewers representing* data. *The* 95% *(red) and* 68% *(blue) confidence levels from* 1*D H I Ly*α *power spectrum calculations are shown in each panel. The dashed lines show the values of lifetime and He II fraction in the sample representing* data. *The quoted values of* $x_{\rm HeII,0}$ *and* $t_{\rm Q}$ *are the best fits based on the* 16*th,* 50*th and* 84*th percentiles of the corresponding distributions.*

a different initial He II fraction in the *data* sample, i.e., $x_{\rm HeII,0} = [0.05, 0.50, 1.00]$. Likewise, each row represents a different value of quasar lifetime in the *data* sample, i.e., $\log\ (t_{\rm Q}/{\rm Myr}) = [0.0, 1.0, 2.0]$.

First, recall the case when the initial He II fraction is low in the IGM, then according to Figure 5.1 there is no substantial heating of the gas due to the quasar turning on, independent of the quasar lifetime value. Consequently, as we showed in § 5.2 the power spectra of such models does not change significantly if one varies the value of quasar lifetime. Therefore, the MCMC calculations will result in the broad distribution of the quasar lifetime values, which one can see in the left-hand column of Figure 5.6. In these cases where *data* is represented by the sample of skewers with initial He II fraction $x_{\rm HeII,0} = 0.05$ the MCMC calculations allow, in general, for all possible lifetime values that we consider here. On the other hand, MCMC calculations have better sensitivity to the value of initial He II fraction, resulting in a reasonable accuracy of $\simeq 0.1$ dex from the *true* values.

In the intermediate case, when the initial He II fraction in the *data* sample is $x_{\rm HeII,0} = 0.50$, the results of MCMC calculations indicate a clear degeneracy between the distribution of quasar lifetime and initial He II fraction values (middle column in Figure 5.6). The ability of MCMC to retrieve the value of initial He II fraction in the *data* sample depends strongly on the size of the region of IGM, influenced by the changes in temperature. But, remember, that this size is set by the duration of quasar activity $t_{\rm Q}$. Hence, the best constraints on the initial He II fraction are obtained if the quasar was active for $t_{\rm Q} = 10^8$ yr, when the thermal proximity effect spans over $R \simeq 80$ cMpc (see Figure 5.1), yielding $x_{\rm HeII,0} = 0.49^{+0.042}_{-0.036}$. This can be seen in the bottom panel of the middle column in Figure 5.6, where the distribution of $x_{\rm HeII,0}$ values sharply pick around $x_{\rm HeII,0} \approx 0.50$ value. On the contrary, if the quasar lifetime is short, i.e., $t_{\rm Q} = 10^6$ yr, then the constraints on the He II fraction are modest, with big uncertainty $x_{\rm HeII,0} = 0.48^{+0.241}_{-0.160}$. The same general trends also apply to the right most column in Figure 5.6, illustrating the results of the MCMC calculations in cases when initial He II fraction in the *data* sample is $x_{\rm HeII,0} = 1.00$.

Surprisingly, our method is capable of recovering the *true* value of the quasar lifetime with a very good precision in all cases when there is a noticeable heating, i.e., initial He II fractions $x_{\rm HeII,0} = 0.50$ and $x_{\rm HeII,0} = 1.00$ (the middle and right columns of Figure 5.6). However, the results of MCMC shown in Figure 5.6 indicate that our method is more sensitive to the longer values of quasar lifetime, which comes from the fact that in this case the thermal proximity effect is larger and, thus, the H I Lyα forest is more affected by the thermal broadening.

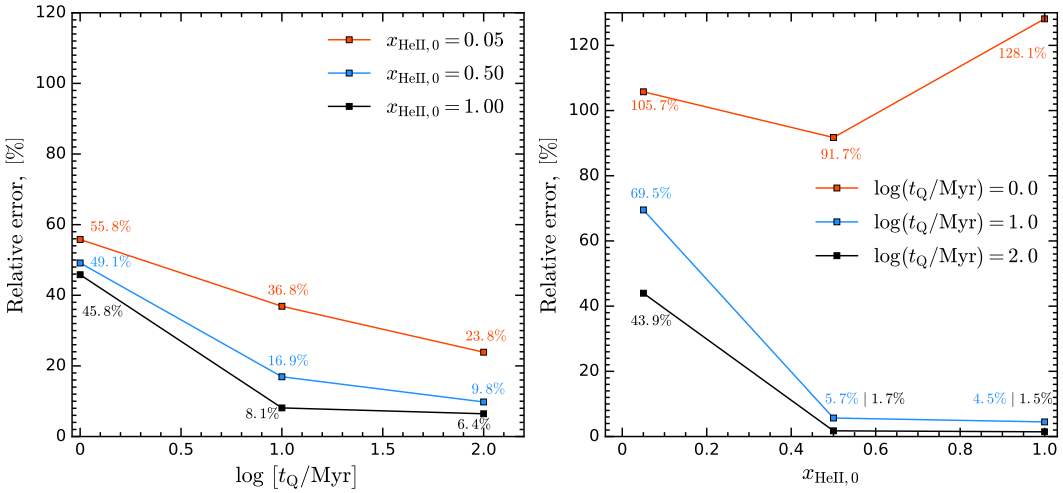

FIGURE 5.7: *Relative error on the initial He II fraction $x_{HeII,0}$ as a function of quasar lifetime (*upper panel*) and on the quasar lifetime t_Q as a function of initial He II fraction (*bottom panel*). Each marker indicates the true value of the parameter in the* data *sample. Relative errors are quoted in both panels.*

5.5 MCMC ANALYSIS: ACCURACY

Based on the results of MCMC calculations, we summarize the accuracy of our method by calculating the relative errors (or the *coefficient of variation*) on the estimated values quasar lifetime and initial He II fraction, which is given by

$$\text{Relative Error} = \frac{\sigma}{\mu} \tag{5.12}$$

where σ and μ are the standard deviation and the mean of the posterior distributions, respectively. This relative error is a good indicator of the degree of dispersion in the retrieved distributions of t_Q and $x_{HeII,0}$.

The left panel in Figure 5.7 illustrates the relative error on the recovered values of initial He II fraction as a function of quasar lifetime t_Q. Likewise, the right panel shows the analogous relative error but on the quasar lifetime values as a function of initial He II fraction $x_{HeII,0}$. It is apparent from Figure 5.7 that we obtain the best sensitivity to the value of initial He II fraction when the quasar lifetime is sufficiently long and, therefore, the thermal proximity effect is the most prominent. While the relative error on $x_{HeII,0}$ is large $\simeq 50 - 60\%$ when the quasar lifetime is short $t_Q = 10^6$ yr, it decreases to $\simeq 6 - 20\%$ when quasar is active for $t_Q = 10^8$ yr. We also note that the precision of our method on initial He II fraction is better if the IGM

still contains significant amounts of He II atoms, which increases the amplitude of the thermal proximity effect when quasar ionization front passes through the IGM. Otherwise, for low values of $x_{\rm HeII,0}$ the thermal proximity effect is negligible and the accuracy of MCMC calculations becomes moderate, which is shown in the left panel of Figure 5.7 by the different curves. However, our method still allows to put a meaningful upper limit on the amount of singly ionized helium even for the short lifetimes.

Likewise, the accuracy on the quasar lifetime is very poor when the initial fraction of singly ionized helium in the *data* sample is already low prior to the quasar activity. In this case the relative error is $\simeq 40 - 100\%$. However, the larger is the He II fraction, the more pronounced is the thermal proximity effect and its effect on the H I Lyα forest. Thus, for high values of $x_{\rm HeII,0}$ the precision of our method measuring the quasar lifetime increases to the fascinating $\simeq 1.5 - 5\%$, which is illustrated by the blue and black curves in the right panel of Figure 5.7. However, if the quasar is active only for the very short period of time, i.e., $t_{\rm Q} = 10^6$ yr, then the size of the thermal proximity effect is small (see Figure 5.1), regardless of the amount of He II in the IGM. Thus, our method is not able to constrain such short quasar lifetime with good precision, which is illustrated by the red curve in the right panel of Figure 5.7.

5.6 SUMMARY

We have illustrated that thermal evolution of the intergalactic medium around the quasar depends significantly on the initial He II fraction $x_{\rm HeII,0}$ and quasar lifetime $t_{\rm Q}$. We have shown that while the amount of the singly ionized helium that prevailed in the IGM prior to the quasar activity sets the amplitude of the temperature increase in the IGM, the value of quasar lifetime defines its spatial extent.

We have investigated the possibility of detecting this thermal proximity effect in the spectra of high-redshift quasars by the means of H I Lyα forest power spectrum statistics and illustrated the sensitivity of the small-scale cutoff of the power spectrum to the parameters $x_{\rm HeII,0}$ and $t_{\rm Q}$. Using MCMC algorithm we have explored the accuracy of the power spectrum measurements and found that with a realistic sample of 50 quasar spectra we can estimate quasar lifetime with accuracy up to $\approx 2 - 5\%$ and initial He II fraction with an accuracy of up to $\approx 5 - 10\%$.

Chapter 6

Conclusions and Future Work

"There is no real ending.
It is just the place where you stop the story."
Frank Herbert

The lifetime of quasars is a fundamentally critical timescale for understanding how the supermassive black holes formed in the Universe, how they co-evolved with their host galaxies and influenced their properties via powerful feedback mechanisms. Moreover, it is also an important parameter in the models of cosmic reionization, influencing the duration and morphology of reionization, as well as the fluctuations of the IGM opacity (McQuinn et al. 2009a; Compostella et al. 2013, 2014). However, despite a lot of effort in the recent years, the lifetime of quasars is still not well constrained. To date, the best estimates from various observational and theoretical techniques give only loose constraints: currently known only to within several orders of magnitude ($10^4 \lesssim t_{\rm Q} \lesssim 10^9$ yr; Martini 2004). The main goal of this thesis is to create a theoretical method to considerably improve these constraints using the structure of quasar proximity zones. For this we have used a combination of numerical hydrodynamical simulations and a 1D radiative transfer algorithm (see Chapter 2) to study the evolution of the He II proximity zones around quasars at $z \simeq 3$ and $z \simeq 4$. We have analyzed the effects of the quasar lifetime ($t_{\rm Q}$), the average He II ionizing background ($\Gamma^{\rm bkg}_{\rm HeII}$), and the photon production rate of the quasar ($Q_{\rm 4Ry}$) on the transmission profiles of He II proximity zones. The primary results of this work are listed in what follows.

6.1 MAIN RESULTS OF THE THESIS

Previous work analyzing the structure of He II proximity zones have assumed that the edge of the observed proximity zone can be identified with the radius of the quasar ionization front $R_{\rm IF}$ (Hogan et al. 1997; Anderson et al. 1999; Zheng et al. 2015). We showed that the He II proximity zones of quasars in an IGM with $x_{\rm HeII} \simeq 1$ and quasar lifetimes $t_{\rm Q} \simeq 30\,{\rm Myr}$, can look identical to those in an IGM with primarily doubly ionized helium $x_{\rm HeII} \simeq 0.03 - 0.05$ and shorter lifetimes $t_{\rm Q} \simeq 10\,{\rm Myr}$. Thus, analogous to the situation of H I proximity zones around $z \sim 6$ quasars (Bolton & Haehnelt 2007a; Lidz et al. 2007; Maselli et al. 2007), naively identifying the size of the proximity zone with the location of the ionization front can lead to erroneous conclusions about the parameters which govern them. Furthermore, whereas the majority of previous work (Hogan et al. 1997; Anderson et al. 1999; Zheng et al. 2015) has assumed that helium is completely singly ionized $x_{\rm HeII} \simeq 1$, we argued that observations of the effective optical depth at $z = 3.1$ suggest the characteristic $\Gamma^{\rm bkg}_{\rm HeII} = 10^{-14.9}{\rm s}^{-1}$ and hence helium is highly doubly ionized in He III regions $x_{\rm HeII} \simeq 0.02$. Thus He II proximity zones are more likely to in a regime where radiation from the quasar increases the ionization level of nearby material which was already highly ionized to begin with, making the location of the ionizaton front irrelevant.

In Chapter 3 we introduced a new and more appropriate way of thinking about proximity zones in terms of the time-evolution of the He II fraction and its approach to equilibrium, which governs both the case of a quasar turning on in an IGM for which helium is singly ionized, as well as case where the IGM is already highly doubly ionized. We presented a simple analytical formula describing this time evolution, and showed that it agrees with the results of detailed radiative transfer calculations. This model was used to understand how proximity zone properties reflect the quasar lifetime, He II-ionizing background, and the photon production rate, and the degeneracies between these parameters. The approach to ionization equilibrium in the proximity zone is set by the equilibration timescale, which is the inverse of the local photoionization rate $t_{\rm eq} \simeq \Gamma^{-1}_{\rm tot}$. It follows that for an IGM in which helium is already highly doubly ionized, which is likely to be the case at $z = 3.1$, the maximum value of the quasar lifetime that one can probe is $t^{\rm max}_{\rm Q} \simeq 1/\Gamma^{\rm bkg}_{\rm HeII} \simeq 2.5 \times 10^7\,{\rm yr}$, which is comparable to the Salpeter time.

In Chapter 4 we argued that IGM density fluctuations result in significant dispersion in the sizes and properties of the He II proximity zone, making it difficult to isolate parameter dependencies. In order to eliminate this source of variation, we investigated stacking proximity zones for ensembles of quasars. We presented the results of our radiative transfer simulations at $z \simeq 3.1$. We find that because the value of He II ionizing background is determined independently from the measurements of

the He II effective optical depth, the degeneracy which exists between quasar lifetime and He II background can be broken. Therefore the resulting stacked transmission profiles at $z \simeq 3.1$ can be used to determine the quasar lifetime. We also showed that the shape of the stacked transmission profiles is highly sensitive to the distribution of quasar lifetimes, which should be taken into account in any attempt of modeling the observational data. On the other hand, a broad distribution of He II backgrounds does not impact the stacked profiles significantly. Unfortunately, in contrast to the case of $z \simeq 3.1$, the He II ionizing background is poorly constrained at higher redshifts $z \simeq 4$, because the increase in the He II effective optical depth, implies the transmission is beyond the sensitivity limit of HST/COS. Combined with additional uncertainties in the quasar SED above 4 Ry, it will be extremely challenging to determine quasar lifetime or He II background independently using He II proximity zones of $z \simeq 4$ quasars.

In Chapter 5 we have introduced a novel technique to overcome these obstacles and probe the ionization state of intergalactic helium and quasar lifetime at $z \gtrsim 4$ via the thermal proximity effect. We have illustrated how the hard quasar radiation increases the average temperature of the surrounding IGM during the ionization of intergalactic helium. Moreover, we showed that the amplitude of the thermal proximity effect depends strongly on the amount of singly ionized helium in the IGM prior to the quasar activity, while the spatial extent of this IGM region with elevated temperatures depends on the value of quasar lifetime. We proposed a method to detect these temperature fluctuations and thus place constraints on $x_{\rm HeII,0}$ and $t_{\rm Q}$ by measuring the H I Lyα power spectrum, which is directly sensitive to the temperature of the IGM because thermal broadening smooths the absorption lines. Applying the Bayesian MCMC formalism to a mock dataset of 50 quasars at $z \simeq 4$, we predicted that we can measure quasar lifetime with an accuracy up to $\approx 2-5\%$, and initial fraction of singly ionized helium to an accuracy of up to $\approx 5-10\%$.

6.2 OUTLOOK

In what follows I briefly summarize several possible extensions of the work presented in this thesis, concentrating on the projection of this theoretical framework on to the real observational domain.

6.2.1 COMPARISON TO HST/COS DATA

The HST/COS archive now has 22 He II Lyα spectra of $z \simeq 3-4$ quasars with signatures of He II proximity zones (Worseck et al. 2011; Syphers et al. 2012; Worseck et al. 2014; Worseck in prep.). Therefore, it is straightforward to measure the average quasar lifetime t_Q by stacking the existing spectra of an ensemble of quasars and comparing the results to the radiative transfer simulations described in this thesis. A preliminary result of such analysis is illustrated in Figure 6.1, where we compare the average transmission profile of the subset of 10 quasar spectra observed with HST/COS at mean redshift $\langle z \rangle = 3.49$ to the stacked radiative transfer outputs of our simulations for different quasar lifetimes. These results favor the average quasar lifetime of $t_Q = 10-15$ Myr, comparable to the expected e-folding (or Salpeter) timescale.

Future analysis of all 22 He II Lyα transmission spectra will also benefit from the careful treatment of the expected uncertainties on quasar lifetime t_Q. Such uncertainties are induced by the limited S/N ratio and spectral resolution, degeneracies with the quasar luminosity and the metagalactic ionizing background field, and the underlying distribution of quasar lifetimes in the sample. It will be possible to marginalize

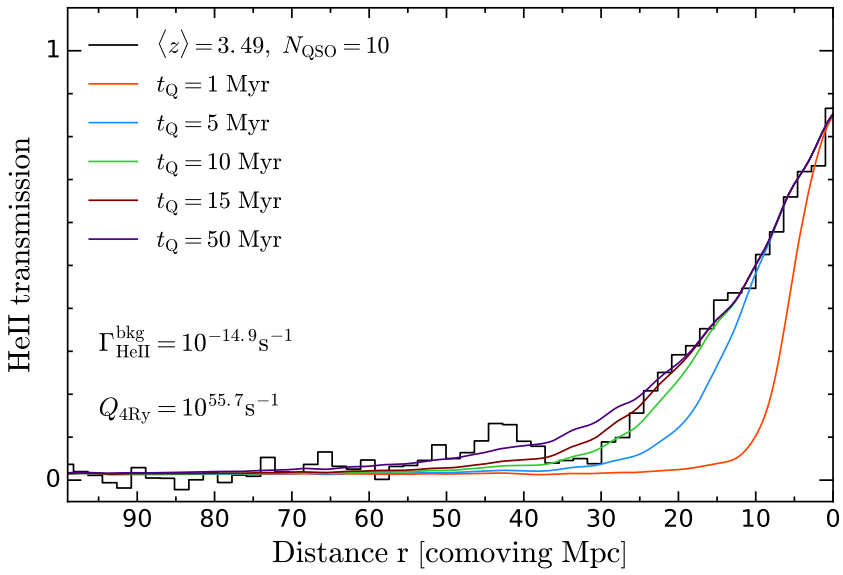

FIGURE 6.1: *Comparison between the observed He II proximity zones and the results of the radiative transfer algorithm. The black step line shows stacked He II Lyα transmission spectrum of 10 quasars observed with HST/COS with mean redshift $\langle z \rangle = 3.49$. The results of the radiative transfer algorithm are shown by colored curves for different quasar lifetime t_Q. Each curve is a stack of 100 sightlines smoothed to HST/COS resolution.*

out these effects using the approach described in this thesis (see Chapters 3&4).

In the context of the next generation of UV space missions (for example, "Spectr-UF" ("World Space Observatory-Ultraviolet") project; Shustov & Sachkov 2014), it would also be extremely interesting to acquire He II Lyα transmission spectra covering the proximity zones of $z \simeq 2-4$ quasars. Comparing these additional observations to the results of our radiative transfer simulations would allow one to improve our constraints on the quasar lifetime as a function of luminosity and redshift, as well as to characterize the ionization state of the IGM as a function of cosmic epoch.

6.2.2 CONSTRAINTS ON QUASAR LIFETIME FROM H I PROXIMITY ZONES AT $z \sim 6$

The general equilibration time picture explored in this work in the context of He II proximity zones is also applicable to study the properties of the analogous H I proximity zones around $z \simeq 6-7$ quasars. I, therefore, propose to use the same technique to study the H I proximity effect at $z \simeq 6$. These studies would also benefit from stacking of multiple sightlines, which would yield interesting insights into the evolution of quasars and the intergalactic medium. Ultimately this will lead to a one-to-one comparison between the physical properties of the H I and He II proximity zones at the very end of two reionization epochs. These results will be invaluable to describe and compare the properties of the ionized IGM and the constraints on quasar properties at two different epochs. Results of numerical simulations compared to the existing spectra of quasars at redshift $z \sim 6$ will give an independent measurement of hydrogen neutral fraction together with H I ionizing background enhanced in the quasar vicinity. This method will help to estimate the mean lifetime of the quasars at $\langle z \rangle \sim 6$ and show the presence/absence of the redshift evolution of the quasar lifetime. An additional motivation for this project is the upcoming launch of the James Webb Space Telescope mission (Gardner et al. 2006), for which Epoch of H I Reionization is one of the four primary science goals.

6.2.3 THERMAL PROXIMITY EFFECT

In Chapter 5 we described the full theoretical framework for detection and subsequent analysis of the thermal proximity effect in the spectra of high-redshift quasars. Given the uncertainties in the quasar SED at energies above He II ionization potential and possible variations in the SED of different quasars, our method will bene-

fit from including an additional parameter in our thermal proximity effect measurements, namely, the spectral slope of the quasar SED α_ν. This parameter is directly related to the number of hard ionizing photons that are produced by the quasar and, therefore, might have an effect on the amplitude of the thermal proximity effect. We thus will incorporate it in our power spectrum and MCMC pipeline in the future. The next logical step will be to apply this method to a set of real high-resolution quasar spectra. The high resolution and high S/N are required for the power spectrum analysis of the H I Lyα forest to resolve all small-scale structures in the forest and, thus, minimize uncertainties. We will apply our power spectrum and MCMC pipeline to all existing archival $z \gtrsim 4$ H I Lyα transmission quasar spectra (currently 85 archival spectra available at $z \gtrsim 4$, which is ~ 1.7 times larger than the number of mock spectra used in our theoretical analysis). The detailed analysis of these data based on the method described in Chapter 5 will for the *first time* achieve two goals: 1) definitively determine when He II was reionized, thus filling the gap in our understanding of the IGM evolution; and 2) constrain the average quasar lifetime at $z \gtrsim 4$, improving our understanding of the co-evolution of the SMBHs and galaxies at large cosmological lookback times.

* * *

In conclusion, there is no doubt that the future generation of ground- and space-based instruments will provide us with the wealth of information about the early stages of the evolution of the Universe. The discovery of the most distant quasars and extensive follow-up analysis of the absorption features in their spectra combined with accurate theoretical models will greatly improve our understanding of the physical mechanisms responsible for the evolution of the intergalactic medium, galaxies and supermassive black holes. The work presented in this thesis is only the beginning of the long, but very exciting journey through the *uncharted territories* of astrophysics.

Appendix A

Light Travel Effects

The radiative transfer algorithm we used in this study works under the assumption of the infinite speed of light. This assumption can result in the nonphysical ionization fronts traveling with speed greater than a speed of light. However, previous works have found that the infinite speed of light assumption describes exactly the ionization state of the gas along the light cone. Here we will show that this is indeed correct.

Let $X(r,t)$ be the gas property (ionization state of the gas influenced by the quasar radiation) at position r from the quasar and time t. It is influenced by the properties at position $r' > r$ if r' is located on the backward light cone. Time evolution of the property $X(r,t)$ is, thus, given by

$$X(r,t) = X(r', t - dt) + \int_r^\infty dr' f\left(r', t - \left[r' - r\right]/c\right) dt \tag{A.1}$$

where f is the function describing the ionization state of the gas at the position r' and the luminosity of the quasar at time $(r_{QSO} - r)/c$ in the past. The differential form of this equation is described by

$$\frac{dX(r, t - r/c)}{dt} = \int_r^\infty dr' f\left(r', t - r'/c\right) \tag{A.2}$$

Evaluating the property $X(r,t)$ on the light cone gives

$$\frac{dX(r, t_{LC})}{dt_{LC}} = \int_r^\infty dr' f\left(r', t_{LC}\right) \tag{A.3}$$

where time on the light cone $t_{LC} = t - r/c$

This solution is identical to the one given by the infinite speed of light approximation

$$\frac{dX(r,t)}{dt} = \int_r^\infty dr' f(r',t) \tag{A.4}$$

As long as the boundary conditions for the $X(r,t)$ are the same as the light cone time boundary conditions the infinite speed of light code provides the same solution for the state of gas as solving for this state on the light cone. The light cone solution is the solution relevant for the line-of-sight proximity region.

Appendix B

The Impact of Lyman-Limit Systems

For the expected values of the He II ionizing background (see § 3.1), clouds which have H I Lyα forest column densities of $N_{\rm HI} \gtrsim 10^{15}\,{\rm cm}^{-2}$ (McQuinn et al. 2009a) will be dense enough to self-shield against He II ionizing photons, making them much more abundant than the higher column density H I Lyman-limit systems ($N_{\rm HI} > 10^{17.3}\,{\rm cm}^{-2}$). For such self-shielding absorbers, the quasar photoionization rate $\Gamma_{\rm QSO}$ is always properly attenuated within the He II-LLS, experiencing the correct $e^{-\tau}$ attenuation in every pixel along the sightline, as determined by our radiative transfer algorithm. However, the photoionization rate due to the He II ionizing background, $\Gamma^{\rm bkg}_{\rm HeII}$, was introduced as a constant homogeneous quantity in every pixel, and this effectively treats these overdense self-shielded regions as being optically thin. Ignoring this attenuation will give He II fractions in the overdense He II-LLSs which are systematically too low, which then further manifests as errors in our radiative transfer from the quasar. An exact treatment of this problem is clearly impossible with a one-dimensional radiative transfer implementation, since the full solution requires attenuating the UV background coming from rays in all directions. In order to model the self-shielding of He II-LLSs from the UV background more accurately, we adapt an algorithm first introduced in McQuinn & Switzer (2010).

First, the algorithm identifies the locations of LLS along the skewer, defined as the pixels with overdensities above a threshold value of $1+\delta > 5$. Regions that have overdensities $1+\delta < 5$ experience an initial unattenuated background photoionization rate $\Gamma^{\rm bkg}_{\rm HeII}$. Whereas, the He II ionizing background is attenuated inside of each segment with $1+\delta > 5$ based on the optical depth to neighboring cells. Specifically, the algorithm assumes half of $\Gamma^{\rm bkg}_{\rm HeII}$ comes to the overdense region from each side. It then calculates the optical depth in one direction $\tau_{<i} = \sigma_{\rm HeII} \times N_{{\rm HeII},<i}$ for all pixels

inside the overdense segment, where i is the pixel number, $\sigma_{\rm HeII}$ is the He II cross-section at the ionizing edge, and $N_{\rm HeII,<i}$ is the He II column density to the pixel i from pixels $< i$ above the overdensity threshold. Similarly, the code computes the contribution to the optical depth $\tau_{>i}$ arising in the other direction from pixels $> i$. The He II ionizing background coming from each direction, $\Gamma^{\rm bkg}_{\rm HeII}/2$, is then attenuated inside the overdense segment by $e^{-\tau_{<i}}$ and $e^{-\tau_{>i}}$, respectively, and these two contributions are summed to give the final attenuated background photoionization rate in the cell. This procedure is performed at each time step of the radiative transfer evolution, and is iterated until convergence is achieved.

Without self-shielding in He II-LLSs, our procedure for initializing the $x_{\rm HeII}$ in the code is straightforward. With the quasar off, the only source of radiation is the background, and since this background is assumed to be present in each pixel, the initial He II fractions are set by simply imposing optically thin photoionization equilibrium. With self-shielding however, the value of the background is attenuated in the LLS pixels, and these pixels must be initialized with their correct equilibrium He II fraction. But because we compute the attenuation by integrating out to determine the optical depth in two directions, the level of attenuation depends on the He II fraction in other neighboring pixels. To ensure that the quasar radiative transfer begins with the correct initial He II fractions at $t = 0$, we adopt the following approach. Similar to the case without self-shielding, we first initialize each pixel assuming optically thin ionization equilibrium with the unattenuated UV background, which underestimates the He II fractions in LLS pixels. We start the calculation at time $t = -5 \times t_{\rm eq}$ with the quasar turned off, where $t_{\rm eq} = 1/\Gamma^{\rm bkg}_{\rm HeII}$ is the characteristic timescale for the He II fraction to reach its equilibrium value (see eqn. 2.7). This procedure ensures that photoionization equilibrium with the background is achieved at all pixels, including those self-shielding pixels for which the background is attenuated. The quasar is then turned on at time $t = 0$ and the photoionization rate becomes $\Gamma_{\rm tot} = \Gamma_{\rm QSO} + \Gamma^{\rm bkg}_{\rm HeII}$, and thus the radiative transfer is evolved with the appropriate initial conditions everywhere.

He II Lyman-limit systems are dense self-shielding absorbers that can act to stop the ionization front in its tracks. They will add variance to the profile of He II proximity zones. These systems are captured in simulations, but as we have mentioned our default radiative transfer algorithm makes their helium overly doubly ionized by the uniform ionizing background.

Figure B.1 shows an example skewer from our radiative transfer algorithm. We ran our algorithm for 10 Myr and use our fiducial value of He II ionizing background (see § 3.1) of $\Gamma^{\rm bkg}_{\rm HeII} = 10^{-14.9}{\rm s}^{-1}$ and $Q_{\rm 4Ry} = 10^{56.1}{\rm s}^{-1}$.

Note that ignoring LLSs can lead to inaccurate results for three different reasons: 1)

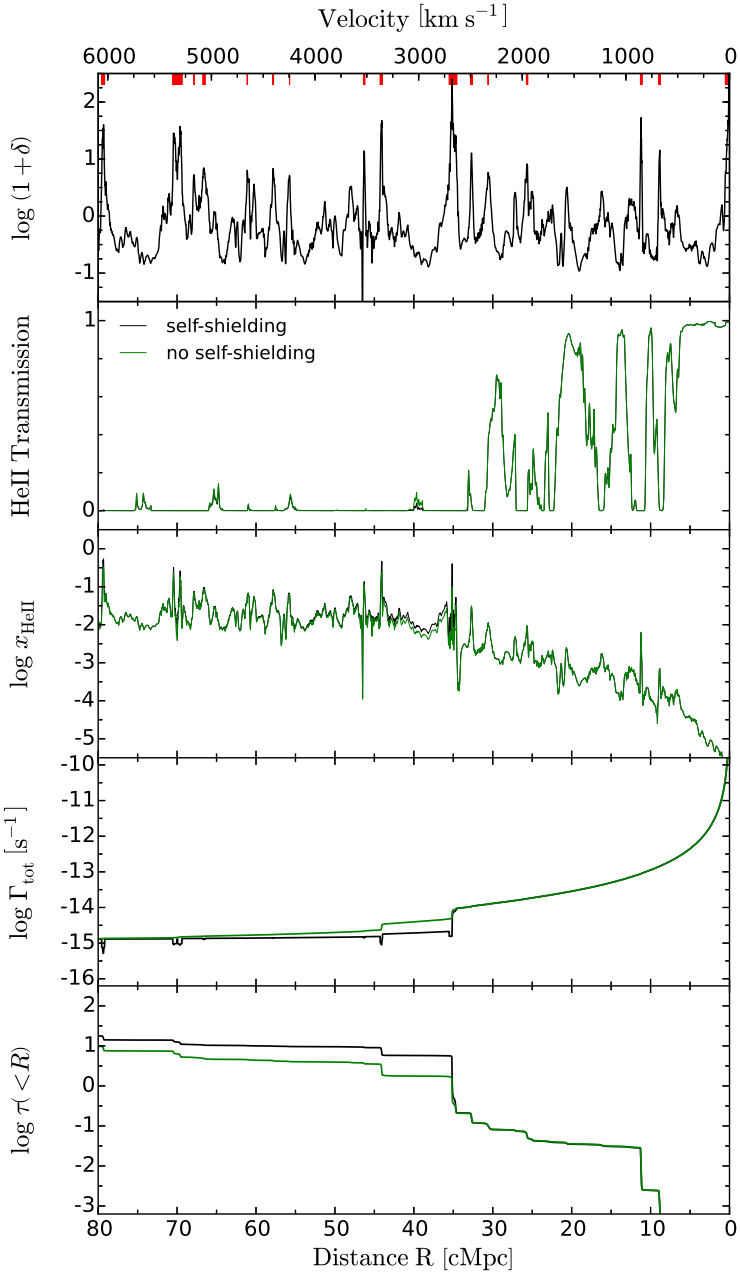

FIGURE B.1: *Impact of Lyman-Limit Systems on the proximity zone. From top to bottom panels show: distribution of the overdensities (all locations of He II-LLS are marked by the red ticks on top), transmission in He II, evolution of the He II fraction* $x_{\rm HeII}$*, total photoionization rate* $\Gamma_{\rm tot}$ *and the Lyman continuum optical depth* $\tau\,(< R)$*.*

the initial He II fractions are not correct in the LLS pixels because the pixels are initialized under the assumption that they are optically thin, and the initial He II

fractions in these pixels are thus set too low. These self-shielding pixels should have very high He II fractions, but instead they start out highly doubly ionized and thus reach their equilibrium ionization state too soon; 2) the total photoionization rate $\Gamma_{\rm tot}$ in the He II-LLS pixels is incorrect because the UVB is not attenuated, hence their $t_{\rm eq}$ are too short, and they thus evolve away from their (incorrect) initial state too fast; 3) these two effects result in incorrect He II fractions at various He II-LLS locations along the skewer, which then implies that the amount of attenuation between any location and the quasar is incorrectly modeled, the photoionization rate $\Gamma_{\rm tot}$ is overestimated everywhere, and thus evolution of the He II fractions in the proximity zone will proceed too quickly.

Now first consider locations very close to the quasar, i.e., $R \ll R_{\rm bkg}$, such that the quasar dominates over the background. For these locations the presence of He II-LLSs make no difference. Referring to the three reasons described above, we can see that this is true because: 1) very near the quasar $t_{\rm eq}(R) \sim 10^4 - 10^5$ yr and thus for the typical quasar lifetimes we consider $t_{\rm eq} \ll t_{\rm Q}$ and the He II fraction has already reached its equilibrium value and has no memory of the incorrect LLS initial conditions; 2) the quasar completely dominates over the UVB, so incorrectly attenuating the UVB changes $t_{\rm eq} = \Gamma_{\rm tot}^{-1}$ negligibly; 3) given that 1) and 2) will be even more true closer to the quasar, the attenuation is correctly modeled, and the He II fractions with and without He II-LLSs are essentially the same. Examining Figure B.1, we see that for $R < 30\,$cMpc, where the quasar radiation completely dominates over the He II ionizing background, all parameters are indistinguishable with and without self-shielding.

At distances $R > 30$ cMpc one reaches the regime where the He II background becomes comparable to the photoionization rate of the quasar and LLSs become important. According to the three criteria we used before this happens because: 1) for typical values of quasar lifetimes that we consider $t_{\rm eq} \geq t_{\rm Q}$ and thus $x_{\rm HeII}$ can still be out of equilibrium at $t \sim t_{\rm Q}$. Consequently, setting the initial He II fraction correctly based on the attenuated background radiation field $\Gamma_{\rm HeII}^{\rm bkg}$ is important. If LLS attenuation is ignored, the initial $x_{\rm HeII}$ are too low and are underestimated at the end of each time-step; 2) because at these radii $\Gamma_{\rm HeII}^{\rm bkg} \sim \Gamma_{\rm QSO}$ the equilibration time becomes strongly dependent on $\Gamma_{\rm HeII}^{\rm bkg}$ and it will be too short if the UVB is not attenuated properly, thus the rate of the gas evolution will be incorrect; 3) the result is the lack of attenuation in the overdense pixels, which leads to the too quick evolution of a proximity zone. One can see this effect in Figure B.1 at $R > 30$ cMpc. The photoionization rate in the no self-shielding case (green) is clearly overestimated in the He II-LLSs, where $x_{\rm HeII}$ is lower than in the self-shielding case (black).

Finally, at distances $R > 60$ cMpc, the total photoionization rate $\Gamma_{\rm tot}$ is totally dominated by the UV background and the quasar radiation $\Gamma_{\rm QSO}$ has a very weak effect on

the IGM. But at this point the treatment of He II-LLSs is unimportant for predicting the transmitted flux because essentially all of the transmission in the He II Lyα forest comes from the underdense regions and the He II-LLSs are always line black.

Ultimately, He II-LLSs do not change the results dramatically neither in the inner part of the proximity zone, nor at larger distances ($R > 30$ cMpc) where they have the biggest effect on the photoionization rate and thus He II fraction. The reason is that in both models the optical depth $\tau\,(< R)$ becomes larger than unity at $R \sim 30$ cMpc and the resulting attenuation $e^{-\tau}$ is effectively the same with or without self-shielding. Therefore, despite some differences at large distances, inside the proximity zone of the quasar, where the ionizations are dominated by the quasar, the effect of self-shielding in LLSs on the ionizing background radiation field is negligible.

Appendix C

He II ionizing radiation from recombinations

The recombinations to the ground state of He II produce additional He II ionizing radiation, that can affect the evolution of the He II fraction and subsequently change the transmission profile in the He II proximity zone. In reality calculation of this radiation is a 3D problem that can not be simply addressed with our 1D radiative transfer algorithm. In addition, introducing this radiation in our radiative transfer algorithm would effectively make each cell also a source of ionizing radiation and, therefore, would complicate the calculations. In what follows, we estimate the importance of recombination radiation using a simple analytical toy model and argue that it can be safely neglected.

Consider a spherically symmetric region around the quasar of size equal to the radius of the ionization front $R_{\rm IF}$ (see eqn. 3.2). For the purpose of this calculations let us assume that He II ionizing photons are produced only from the recombinations of helium ions and free electrons inside this region. We assume further that the distribution of the gas density and temperature ($T = 10^4$ K) are homogeneous inside the region with an average He II fraction $x_{\rm HeII} = 0.02$, and that all recombination radiation is emitted only at a single frequency $\nu_{\rm th}$ corresponding to the He II ionization threshold of 4 Ryd. A remote observer tracks the evolution of the radiation field inside the region only along a 1D line-of-sight towards the center of the region.

Using the equation of radiative transfer we can estimate the monochromatic intensity I_ν of the recombination radiation at any location R along the line-of-sight coming from the location R' inside the spherical region as

$$I_\nu = \int_0^{s(R'-R)} j_\nu e^{-\tau_s} \mathrm{d}s \tag{C.1}$$

where $\tau_s = \int_0^{s(R'-R)} N_{\rm HeII}\sigma_\nu \mathrm{d}s$ is the optical depth in the IGM along the direction $s(R'-R)$ connecting points R' and R. This distance $s(R'-R)$ can be expressed through the viewing angle θ ($0 < \theta < \pi$) between the radial direction to R' and the line-of-sight as

$$s(R'-R)^2 = R^2 + R'^2 - 2RR'\cos(\theta) \tag{C.2}$$

We choose to align our z-axis with the direction of R and hence θ is the usual polar angle in spherical coordinates. The free-bound emissivity j_ν is given by

$$j_\nu = \frac{h^4\nu^3}{(2\pi m_e kT)^{3/2}c^2} e^{\frac{-h(\nu-\nu_{\rm th})}{k_B T}} n_e n_{\rm HeII}\sigma_\nu(\nu) \tag{C.3}$$

where n_e and $n_{\rm HeII}$ are the densities of electrons and ions, respectively.

Combining eqn. (C.1) and eqn. (C.3) the instensity of the recombination radiation can be written as

$$I_\nu(\theta) = \int_0^{s(R'-R)} \frac{h^4\nu^3\sigma_\nu(\nu)\, n_e n_{\rm HeII}}{(2\pi m_e k_B T)^{3/2}c^2} e^{\frac{-h(\nu-\nu_{\rm th})}{k_B T}} e^{-\tau_s}\mathrm{d}s \tag{C.4}$$

Integrating over the solid angle Ω we obtain the mean azimuthally symmetric intensity of the recombination radiation $4\pi J_\nu$ at location R along the line-of-sight

$$4\pi J_\nu = \int I_\nu \mathrm{d}\Omega = 2\pi \int_0^\pi I_\nu(\theta)\sin\theta \mathrm{d}\theta \tag{C.5}$$

Lastly, given eqn. (C.5) for the mean intensity $4\pi J_\nu$ we calculate the He II photoionization rate due to recombinations $\Gamma_{\rm rec}$ as

$$\Gamma_{\rm rec} = \int_{\nu_{\rm th}}^{2\nu_{\rm th}} \frac{4\pi J_\nu}{h_P\nu}\sigma_\nu(\nu)\,\mathrm{d}\nu \tag{C.6}$$

Recall, that we approximated the recombination radiation as being propagated with a single frequency corresponding to 4 Ryd. However, this will make it impossible to calculate the frequency-averaged photoionization rate and we, therefore, assume a narrow finite frequency interval $\nu_{\rm th} \leq \nu \leq 2\nu_{\rm th}$ in order to calculate the integral in eqn. (C.6).

We compare $\Gamma_{\rm rec}$ to the values of quasar photoionization rate $\Gamma_{\rm QSO}$ and He II ionizing background $\Gamma^{\rm bkg}_{\rm HeII} = 10^{-14.9}\mathrm{s}^{-1}$ taken from our fiducial model with quasar lifetime $t_Q = 10$ Myr and quasar photon production rate $Q_{\rm 4Ry} = 10^{56.1}\mathrm{s}^{-1}$. The location of

the ionization front is this model is approximately $R_{\rm IF} \simeq 67$ cMpc, we thus use this value as a boarder of the region where the recombination radiation is calculated. The results are shown in Figure C.1. The blue curve shows the ratio of the He II photoionization rates due to recombinations $\Gamma_{\rm rec}$ and the He II background $\Gamma^{\rm bkg}_{\rm HeII}$. This ratio stays nearly constant throughout the region we consider, with $\Gamma_{\rm rec}$ being $\simeq 10-30\%$ of the $\Gamma^{\rm bkg}_{\rm HeII}$. Not only do recombinations constitute a minor correction to the background, but because $\Gamma_{\rm rec}$ does not vary significantly with distance R, it could also be effectively absorbed into the background and thought of as a small correction to it. At the same time, the red curve shows the ratio between $\Gamma_{\rm rec}$ and quasar photoionization rate $\Gamma_{\rm QSO}$. It is clear that the quasar photoionization rate dominants at all distances R from the quasar, making the contribution of recombination radiation to the total radiation field in the He II proximity region essentially negligible.

Although our analtyical estimate of $\Gamma_{\rm rec}$ is admittedly rather crude, according to Figure C.1 including recombination radiation in our calculation will not significantly change the results of our 1D radiative transfer.

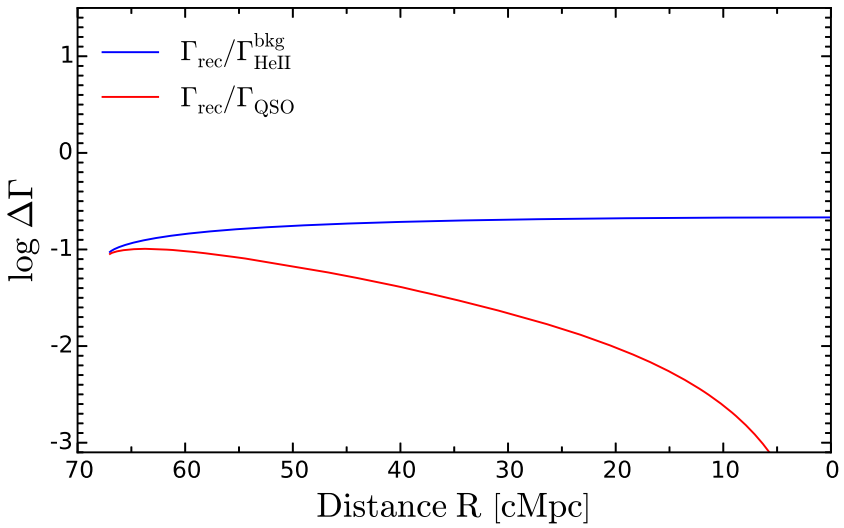

FIGURE C.1: *Comparison between He II recombination radiation photoionization rate* $\Gamma_{\rm rec}$ *and quasar photoionization rate* $\Gamma_{\rm QSO}$ (red curve) *and He II ionizing background* $\Gamma^{\rm bkg}_{\rm HeII} = 10^{-14.9}{\rm s}^{-1}$ (blue curve) *for mean He II fraction* $\langle x_{\rm HeII}\rangle = 0.02$.

Appendix D

Generating He II Lyα absorption spectra

We calculate He II spectra along each of the skewers drawn from the SPH simulations following the procedure described in Theuns et al. (1998). We use densities and velocities of the SPH particles at each pixel, combined with the He II fraction and temperature resulting from our radiative transfer calculation to compute the observed flux $F(v) = e^{-\tau_{\rm HeII}(v)}$, with the He II optical depth $\tau_{\rm HeII}(v)$ of the pixel given by

$$\tau_{\rm HeII}(v) = \frac{\sigma_\alpha c}{\sqrt{\pi} V} n_{\rm He} x_{\rm HeII} (1+\delta) \frac{\Delta R}{1+z} \exp\left(-\left[\frac{v - v_H}{V}\right]^2\right) \tag{D.1}$$

where $V^2 = 2k_{\rm B}T/m_{\rm He}$ is the Doppler width of helium with mass $m_{\rm He}$, c is the speed of light, T is the temperature inside the cell, $n_{\rm He}x_{\rm HeII}$ is the density of He II, ΔR is the pixel width, $\sigma_{\rm HeII}$ is He II Lyα cross-section, and the term $v_{\rm H}$ describes the combination of Hubble and peculiar velocities.

We similarly compute the H I Lyα optical depth. Hydrogen gas is also considered optically thin to the ionizing radiation and analogously to helium, we introduce an H I ionizing background photoionization rate $\Gamma_{\rm HI}^{\rm bkg}$ to mimic the influence of other sources in the Universe, with a value of $\Gamma_{\rm HI}^{\rm bkg} = 1 \times 10^{-12}{\rm s}^{-1}$ chosen to match the mean transmitted flux at $z \simeq 3.1$ in agreement with recent measurements by Becker et al. (2013).

List of Figures

1.1 Ultraviolet He II absorption spectra of quasars Q 0302−003 and HE 2347−4342 13

2.1 Example sightline at $z = 3.1$ from radiative transfer simulations . . . 25

3.1 He II effective optical depth as a function of He II ionizing background 29

3.2 Time-evolution of the He II fraction 32

3.3 Partial degeneracy between the He II ionizing background and the quasar lifetime 36

4.1 Fluctuations of the density field in the He II quasar proximity zones 40

4.2 Evolution and structure of stacked He II proximity zones as a function of quasar lifetime 41

4.3 Time-evolution of the He II fraction in three different locations inside the He II proximity zone 43

4.4 Spacial evolution of the He II photoionization rate and equlibration time in He II proximity zone 44

4.5 Evolution and structure of stacked He II proximity zones as a function of He II ionizing background 46

4.6 Evolution and structure of stacked He II proximity zones as a function of quasar photon production rate 48

4.7 Effect of the distributions of quasar lifetime and He II backgrounds on the stacked transmission profiles in He II proximity zones 50

4.8 Sensitivity of the He II proximity zones at $z \simeq 4$ to the values of quasar lifetime and He II ionizing background 53

4.9 Distribution of the He II proximity zone sizes measured from radiative transfer calculations at $z \simeq 4$ 55

5.1 Thermal evolution of the intergalactic medium around the quasar . . 61

5.2 Radial evolution of the parameters of the temperature-density relation 63

5.3 Sensitivity of the H I Lyα forest power spectrum statistics to the value of quasar lifetime 67

5.4 Sensitivity of the H I Lyα forest power spectrum statistics to the value of initial He II fraction 69

5.5 MCMC analysis (1 model): constraints on $t_{\rm Q}$ and $x_{\rm HeII,0}$ 72

5.6 MCMC analysis (9 models): constraints on $t_{\rm Q}$ and $x_{\rm HeII,0}$ 73

5.7 Relative error on the thermal proximity effect parameters 75

6.1 Comparison between the observed He II proximity zones and the results of the radiative transfer algorithm. 80

B.1 Impact of Lyman-Limit Systems on the proximity zone 87

C.1 He II ionizing radiation from the recombinations 93

Acronyms

ΛCDM	Cold dark matter model with a cosmological constant (Λ)
AGN	Active Galactic Nuclei
CDM	Cold dark matter
CMB	Cosmic microwave background
COBE	Cosmic Background Explorer
COS	Cosmic Origins Spectrograph
EoR	Epoch of Reionization
EW	Equivalent Width
HST	Hubble Space Telescope
IGM	Intergalactic medium
JWST	James Webb Space Telescope
LAE	Lyα Emitter
LOFAR	Low Frequency Array
LLS	Lyman-limit system
MCMC	Markov Chain Monte Carlo
MWA	Murchison Widefield Array
PAPER	Precision Array for Probing the Epoch of Reionizaion
QSO	Quasi-stellar object
Quasar	Quasi-stellar radio source
SED	Spectral energy distribution
SKA	Square Kilometer Array
SMBH	Super-Massive Black Hole
SPH	Smooth Particle Hydrodynamics
UV	Ultraviolet
WIMP	Waekly interacting massive particle
WMAP	Wilkinson microwave anisotropy probe
pMpc	proper Megaparsec
cMpc	comoving Megaparsec

BIBLIOGRAPHY

Abel, T., & Haehnelt, M. G. 1999, ApJ, 520, L13
Adelberger, K. L., & Steidel, C. C. 2005, ApJ, 630, 50
Albrecht, A., & Steinhardt, P. J. 1982, Physical Review Letters, 48, 1220
Alpher, R. A., & Herman, R. C. 1949, Physical Review, 75, 1089
Anderson, S. F., Hogan, C. J., Williams, B. F., & Carswell, R. F. 1999, AJ, 117, 56
Bajtlik, S., Duncan, R. C., & Ostriker, J. P. 1988, ApJ, 327, 570
Balmer, J. J. 1885, Annalen der Physik, 261, 80
Barkana, R., & Loeb, A. 2001, Phys. Rep., 349, 125
Bauer, A., Springel, V., Vogelsberger, M., et al. 2015, MNRAS, 453, 3593
Becker, G. D., & Bolton, J. S. 2013, MNRAS, 436, 1023
Becker, G. D., Bolton, J. S., Haehnelt, M. G., & Sargent, W. L. W. 2011, MNRAS, 410, 1096
Becker, G. D., Bolton, J. S., Madau, P., et al. 2015, MNRAS, 447, 3402
Becker, G. D., Hewett, P. C., Worseck, G., & Prochaska, J. X. 2013, MNRAS, 430, 2067
Becker, R. H., Fan, X., White, R. L., et al. 2001, AJ, 122, 2850
Bennett, C. L., Banday, A. J., Gorski, K. M., et al. 1996, ApJ, 464, L1
Bennett, C. L., Bay, M., Halpern, M., et al. 2003, ApJ, 583, 1
Blumenthal, G. R., Faber, S. M., Primack, J. R., & Rees, M. J. 1984, Nature, 311, 517
Boera, E., Murphy, M. T., Becker, G. D., & Bolton, J. S. 2014, MNRAS, 441, 1916
—. 2015, ArXiv e-prints
Boggess, N. W., Mather, J. C., Weiss, R., et al. 1992, ApJ, 397, 420
Bolton, J. S., Becker, G. D., Haehnelt, M. G., & Viel, M. 2014, MNRAS, 438, 2499
Bolton, J. S., Becker, G. D., Raskutti, S., et al. 2012, MNRAS, 419, 2880
Bolton, J. S., & Haehnelt, M. G. 2007a, MNRAS, 374, 493
—. 2007b, MNRAS, 381, L35
Bolton, J. S., Oh, S. P., & Furlanetto, S. R. 2009, MNRAS, 395, 736

Bolton, J. S., Viel, M., Kim, T.-S., Haehnelt, M. G., & Carswell, R. F. 2008, MNRAS, 386, 1131

Bond, J. R., & Efstathiou, G. 1984, ApJ, 285, L45

Bond, J. R., Kofman, L., & Pogosyan, D. 1996, Nature, 380, 603

Borisova, E., Lilly, S. J., Cantalupo, S., et al. 2015, ArXiv e-prints

Bromm, V., & Yoshida, N. 2011, ARA&A, 49, 373

Cantalupo, S., Arrigoni-Battaia, F., Prochaska, J. X., Hennawi, J. F., & Madau, P. 2014, Nature, 506, 63

Carilli, C. L., Wang, R., Fan, X., et al. 2010, ApJ, 714, 834

Carswell, R. F., Whelan, J. A. J., Smith, M. G., Boksenberg, A., & Tytler, D. 1982, MNRAS, 198, 91

Cen, R., & Haiman, Z. 2000, ApJ, 542, L75

Cole, S., & Kaiser, N. 1989, MNRAS, 237, 1127

Compostella, M., Cantalupo, S., & Porciani, C. 2013, MNRAS, 435, 3169

—. 2014, MNRAS, 445, 4186

Conroy, C., & White, M. 2013, ApJ, 762, 70

Croft, R. A. C., Weinberg, D. H., Bolte, M., et al. 2002, ApJ, 581, 20

Croom, S. M., Boyle, B. J., Shanks, T., et al. 2005, MNRAS, 356, 415

Croom, S. M., Richards, G. T., Shanks, T., et al. 2009, MNRAS, 399, 1755

Davies, F. B., & Furlanetto, S. R. 2014, MNRAS, 437, 1141

Davies, F. B., Furlanetto, S. R., & McQuinn, M. 2014, ArXiv e-prints

Davis, M., Efstathiou, G., Frenk, C. S., & White, S. D. M. 1985, ApJ, 292, 371

Dicke, R. H., Peebles, P. J. E., Roll, P. G., & Wilkinson, D. T. 1965, ApJ, 142, 414

Djorgovski, S. G., Castro, S., Stern, D., & Mahabal, A. A. 2001, ApJ, 560, L5

Efstathiou, G., & Silk, J. 1983, Fund. Cosmic Phys., 9, 1

Fan, X., Carilli, C. L., & Keating, B. 2006a, ARA&A, 44, 415

Fan, X., Narayanan, V. K., Strauss, M. A., et al. 2002, in Lighthouses of the Universe: The Most Luminous Celestial Objects and Their Use for Cosmology, ed. M. Gilfanov, R. Sunyeav, & E. Churazov, 309

Fan, X., Strauss, M. A., Schneider, D. P., et al. 2001, AJ, 121, 54

Fan, X., Strauss, M. A., Becker, R. H., et al. 2006b, AJ, 132, 117

Faucher-Giguère, C.-A., Lidz, A., Hernquist, L., & Zaldarriaga, M. 2008a, ApJ, 688, 85

Faucher-Giguère, C.-A., Lidz, A., Zaldarriaga, M., & Hernquist, L. 2008b, ApJ, 673, 39

Fechner, C., Baade, R., & Reimers, D. 2004, A&A, 418, 857

Feoli, A., & Mele, D. 2005, International Journal of Modern Physics D, 14, 1861

—. 2007, International Journal of Modern Physics D, 16, 1261

Ferrarese, L., & Merritt, D. 2000, ApJ, 539, L9

Finkelstein, S. L., Papovich, C., Ryan, R. E., et al. 2012, ApJ, 758, 93

Finkelstein, S. L., Ryan, Jr., R. E., Papovich, C., et al. 2015, ApJ, 810, 71

Foreman-Mackey, D., Hogg, D. W., Lang, D., & Goodman, J. 2013, PASP, 125, 306

Furlanetto, S. R. 2009, ApJ, 703, 702
Furlanetto, S. R., & Lidz, A. 2011, ApJ, 735, 117
Furlanetto, S. R., & Oh, S. P. 2008, ApJ, 681, 1
Gallerani, S., Ferrara, A., Fan, X., & Choudhury, T. R. 2008, MNRAS, 386, 359
Gamow, G. 1952, The creation of the universe. (New York, Viking Press, 1952.)
Gardner, J. P., Mather, J. C., Clampin, M., et al. 2006, Space Sci. Rev., 123, 485
Gebhardt, K., Bender, R., Bower, G., et al. 2000, ApJ, 539, L13
George, E. M., Reichardt, C. L., Aird, K. A., et al. 2015, ApJ, 799, 177
Giallongo, E., Grazian, A., Fiore, F., et al. 2015, A&A, 578, A83
Gnedin, N. Y. 2000, ApJ, 535, 530
Gnedin, N. Y., & Kaurov, A. A. 2014, ApJ, 793, 30
Gonçalves, T. S., Steidel, C. C., & Pettini, M. 2008, ApJ, 676, 816
Goodman, J. 2003, MNRAS, 339, 937
Graham, A. W., & Driver, S. P. 2007, ApJ, 655, 77
Graham, A. W., Erwin, P., Caon, N., & Trujillo, I. 2001, ApJ, 563, L11
Gunn, J. E., & Peterson, B. A. 1965, ApJ, 142, 1633
Guth, A. H. 1981, Phys. Rev. D, 23, 347
Haardt, F., & Madau, P. 2012, ApJ, 746, 125
Haiman, Z., & Cen, R. 2001, in Astronomical Society of the Pacific Conference Series, Vol. 222, The Physics of Galaxy Formation, ed. M. Umemura & H. Susa, 101
Haiman, Z., & Hui, L. 2001, ApJ, 547, 27
Häring, N., & Rix, H.-W. 2004, ApJ, 604, L89
Hazard, C., Mackey, M. B., & Shimmins, A. J. 1963, Nature, 197, 1037
Heap, S. R., Williger, G. M., Smette, A., et al. 2000, ApJ, 534, 69
Heisenberg, W. 1927, Zeitschrift fur Physik, 43, 172
Hennawi, J. F., & Prochaska, J. X. 2007, ApJ, 655, 735
—. 2013, ApJ, 766, 58
Hennawi, J. F., Prochaska, J. X., Cantalupo, S., & Arrigoni-Battaia, F. 2015, Science, 348, 779
Hennawi, J. F., Prochaska, J. X., Burles, S., et al. 2006, ApJ, 651, 61
Hogan, C. J., Anderson, S. F., & Rugers, M. H. 1997, AJ, 113, 1495
Hopkins, P. F., Bundy, K., Hernquist, L., & Ellis, R. S. 2007b, ApJ, 659, 976
Hopkins, P. F., Hernquist, L., Cox, T. J., & Kereš, D. 2008, ApJS, 175, 356
Hopkins, P. F., Hernquist, L., Cox, T. J., Robertson, B., & Springel, V. 2006, ApJS, 163, 50
Hopkins, P. F., Hernquist, L., Martini, P., et al. 2005, ApJ, 625, L71
Hopkins, P. F., Lidz, A., Hernquist, L., et al. 2007c, ApJ, 662, 110
Hopkins, P. F., & Quataert, E. 2010, MNRAS, 407, 1529
Hopkins, P. F., Richards, G. T., & Hernquist, L. 2007a, ApJ, 654, 731
Hubble, E. P. 1926, ApJ, 64
Hui, L., & Gnedin, N. Y. 1997, MNRAS, 292, 27

Hui, L., & Haiman, Z. 2003, ApJ, 596, 9
Jakobsen, P., Jansen, R. A., Wagner, S., & Reimers, D. 2003, A&A, 397, 891
Jeans, J. H. 1902, Philosophical Transactions of the Royal Society of London Series A, 199, 1
Jiang, L., Fan, X., Vestergaard, M., et al. 2007, AJ, 134, 1150
Kapteyn, J. C. 1922, Contributions from the Mount Wilson Observatory / Carnegie Institution of Washington, 230, 1
Khrykin, I. S., Hennawi, J. F., McQuinn, M., & Worseck, G. 2015, ArXiv e-prints
Kim, T.-S., Bolton, J. S., Viel, M., Haehnelt, M. G., & Carswell, R. F. 2007, MNRAS, 382, 1657
Kirkman, D., & Tytler, D. 2008, MNRAS, 391, 1457
Kormendy, J., & Ho, L. C. 2013, ARA&A, 51, 511
Kormendy, J., & Richstone, D. 1995, ARA&A, 33, 581
Kurk, J. D., Walter, F., Fan, X., et al. 2007, ApJ, 669, 32
Lacey, C., & Cole, S. 1993, MNRAS, 262, 627
Lahav, O., Lilje, P. B., Primack, J. R., & Rees, M. J. 1991, MNRAS, 251, 128
Larson, D., Dunkley, J., Hinshaw, G., et al. 2011, ApJS, 192, 16
Lee, K.-G., Hennawi, J. F., Spergel, D. N., et al. 2015, ApJ, 799, 196
Lidz, A., Faucher-Giguère, C.-A., Dall'Aglio, A., et al. 2010, ApJ, 718, 199
Lidz, A., McQuinn, M., Zaldarriaga, M., Hernquist, L., & Dutta, S. 2007, ApJ, 670, 39
Lifshitz, E. M. 1946, Zhurnal Eksperimentalnoi i Teoreticheskoi Fiziki, 16, 587
Linde, A. D. 1982, Physics Letters B, 108, 389
Lukić, Z., Stark, C. W., Nugent, P., et al. 2015, MNRAS, 446, 3697
Lusso, E., Worseck, G., Hennawi, J. F., et al. 2015, ArXiv e-prints
Lynden-Bell, D. 1969, Nature, 223, 690
Madau, P., & Haardt, F. 2015, ApJ, 813, L8
Madau, P., & Meiksin, A. 1994, ApJ, 433, L53
Madau, P., & Rees, M. J. 2000, ApJ, 542, L69
Madau, P., Rees, M. J., Volonteri, M., Haardt, F., & Oh, S. P. 2004, ApJ, 604, 484
Magorrian, J., Tremaine, S., Richstone, D., et al. 1998, AJ, 115, 2285
Martini, P. 2004, Coevolution of Black Holes and Galaxies, 169
Martini, P., & Weinberg, D. H. 2001, ApJ, 547, 12
Marulli, F., Bonoli, S., Branchini, E., Moscardini, L., & Springel, V. 2008, MNRAS, 385, 1846
Maselli, A., Gallerani, S., Ferrara, A., & Choudhury, T. R. 2007, MNRAS, 376, L34
McConnell, N. J., & Ma, C.-P. 2013, ApJ, 764, 184
McDonald, P., Miralda-Escudé, J., Rauch, M., et al. 2001, ApJ, 562, 52
—. 2000, ApJ, 543, 1
McQuinn, M. 2009b, ApJ, 704, L89
—. 2012, MNRAS, 426, 1349

—. 2015, ArXiv e-prints
McQuinn, M., Lidz, A., Zahn, O., et al. 2007, MNRAS, 377, 1043
McQuinn, M., Lidz, A., Zaldarriaga, M., et al. 2009a, ApJ, 694, 842
McQuinn, M., & Switzer, E. R. 2010, MNRAS, 408, 1945
McQuinn, M., & Worseck, G. 2014, MNRAS, 440, 2406
Meiksin, A., & Tittley, E. R. 2012, MNRAS, 423, 7
Meiksin, A., Tittley, E. R., & Brown, C. K. 2010, MNRAS, 401, 77
Meiksin, A. A. 2009, Reviews of Modern Physics, 81, 1405
Mellema, G., Iliev, I. T., Alvarez, M. A., & Shapiro, P. R. 2006, NA, 11, 374
Mesinger, A., ed. 2016, Astrophysics and Space Science Library, Vol. 423, Understanding the Epoch of Cosmic Reionization
Mesinger, A., & Haiman, Z. 2004, ApJ, 611, L69
Miniati, F., Ferrara, A., White, S. D. M., & Bianchi, S. 2004, MNRAS, 348, 964
Miralda-Escudé, J., Haehnelt, M., & Rees, M. J. 2000, ApJ, 530, 1
Miralda-Escudé, J., & Rees, M. J. 1994, MNRAS, 266, 343
Naoz, S., Noter, S., & Barkana, R. 2006, MNRAS, 373, L98
Oke, J. B. 1963, Nature, 197, 1040
Oort, J. H. 1932, Bull. Astron. Inst. Netherlands, 6, 249
Peebles, P. J. E. 1982, ApJ, 263, L1
Penzias, A. A., & Wilson, R. W. 1965, ApJ, 142, 419
Planck Collaboration, Adam, R., Ade, P. A. R., et al. 2015, ArXiv e-prints
Planck Collaboration, Ade, P. A. R., Aghanim, N., et al. 2015b, ArXiv e-prints
Power, C., Wynn, G. A., Combet, C., & Wilkinson, M. I. 2009, MNRAS, 395, 1146
Press, W. H., & Schechter, P. 1974, ApJ, 187, 425
Primack, J. R., & Blumenthal, G. R. 1984, in NATO Advanced Science Institutes (ASI) Series C, Vol. 117, NATO Advanced Science Institutes (ASI) Series C, ed. J. Audouze & J. Tran Thanh Van, 163–183
Prochaska, J. X., Hennawi, J. F., Lee, K.-G., et al. 2013, ApJ, 776, 136
Puchwein, E., Bolton, J. S., Haehnelt, M. G., et al. 2015, MNRAS, 450, 4081
Richards, G. T., Myers, A. D., Gray, A. G., et al. 2009, ApJS, 180, 67
Ricotti, M., Gnedin, N. Y., & Shull, J. M. 2000, ApJ, 534, 41
Ricotti, M., & Ostriker, J. P. 2004, MNRAS, 352, 547
Robertson, B. E., Ellis, R. S., Dunlop, J. S., McLure, R. J., & Stark, D. P. 2010, Nature, 468, 49
Rubin, V. C., & Ford, Jr., W. K. 1970, ApJ, 159, 379
Ryle, M., & Sandage, A. 1964, ApJ, 139, 419
Salpeter, E. E. 1964, ApJ, 140, 796
Sandage, A. 1965, ApJ, 141, 1560
Sanders, D. B., Soifer, B. T., Elias, J. H., et al. 1988, ApJ, 325, 74
Scannapieco, C., White, S. D. M., Springel, V., & Tissera, P. B. 2009, MNRAS, 396, 696

Schawinski, K., Koss, M., Berney, S., & Sartori, L. F. 2015, MNRAS, 451, 2517
Schawinski, K., Evans, D. A., Virani, S., et al. 2010, ApJ, 724, L30
Schaye, J., Theuns, T., Rauch, M., Efstathiou, G., & Sargent, W. L. W. 2000, MNRAS, 318, 817
Schmidt, M. 1963, Nature, 197, 1040
Shakura, N. I., & Sunyaev, R. A. 1973, A&A, 24, 337
Shen, Y., Strauss, M. A., Ross, N. P., et al. 2009, ApJ, 697, 1656
Shull, J. M., France, K., Danforth, C. W., Smith, B., & Tumlinson, J. 2010, ApJ, 722, 1312
Shull, J. M., Stevans, M., & Danforth, C. W. 2012, ApJ, 752, 162
Shustov, B. M., & Sachkov, M. E. 2014, Solar System Research, 48, 467
Silk, J., & Rees, M. J. 1998, A&A, 331, L1
Soltan, A. 1982, MNRAS, 200, 115
Songaila, A. 2004, AJ, 127, 2598
Springel, V. 2005c, MNRAS, 364, 1105
Springel, V., Di Matteo, T., & Hernquist, L. 2005a, ApJ, 620, L79
—. 2005b, MNRAS, 361, 776
Springel, V., Frenk, C. S., & White, S. D. M. 2006, Nature, 440, 1137
Starobinsky, A. A. 1982, Physics Letters B, 117, 175
Strukov, I. A., Brukhanov, A. A., Skulachev, D. P., & Sazhin, M. V. 1992, Soviet Astronomy Letters, 18, 153
Sunyaev, R. A., & Zeldovich, I. B. 1980, MNRAS, 190, 413
Syphers, D., Anderson, S. F., Zheng, W., et al. 2012, AJ, 143, 100
Syphers, D., & Shull, J. M. 2013, ApJ, 765, 119
—. 2014, ApJ, 784, 42
Tauber, J. A., Mandolesi, N., Puget, J.-L., et al. 2010, A&A, 520, A1
Telfer, R. C., Zheng, W., Kriss, G. A., & Davidsen, A. F. 2002, ApJ, 565, 773
Theuns, T., Leonard, A., Efstathiou, G., Pearce, F. R., & Thomas, P. A. 1998, MNRAS, 301, 478
Theuns, T., Zaroubi, S., Kim, T.-S., Tzanavaris, P., & Carswell, R. F. 2002, MNRAS, 332, 367
Trainor, R., & Steidel, C. C. 2013, ApJ, 775, L3
Upton Sanderbeck, P. R., D'Aloisio, A., & McQuinn, M. J. 2015, ArXiv e-prints
Viel, M., Bolton, J. S., & Haehnelt, M. G. 2009, MNRAS, 399, L39
White, M., Myers, A. D., Ross, N. P., et al. 2012, MNRAS, 424, 933
White, R. L., Becker, R. H., Fan, X., & Strauss, M. A. 2003, AJ, 126, 1
White, S. D. M., & Rees, M. J. 1978, MNRAS, 183, 341
Willott, C. J., McLure, R. J., & Jarvis, M. J. 2003, ApJ, 587, L15
Willott, C. J., Delorme, P., Reylé, C., et al. 2010, AJ, 139, 906
Worseck, G. in prep.
Worseck, G., Fechner, C., Wisotzki, L., & Dall'Aglio, A. 2007, A&A, 473, 805

Worseck, G., Prochaska, J. X., Hennawi, J. F., & McQuinn, M. 2014, ArXiv e-prints
Worseck, G., & Wisotzki, L. 2006, A&A, 450, 495
Worseck, G., Prochaska, J. X., McQuinn, M., et al. 2011, ApJ, 733, L24
Wyithe, J. S. B., Bolton, J. S., & Haehnelt, M. G. 2008, MNRAS, 383, 691
Wyithe, J. S. B., & Loeb, A. 2003, ApJ, 595, 614
Yu, Q., & Lu, Y. 2004, ApJ, 602, 603
Yu, Q., & Tremaine, S. 2002, MNRAS, 335, 965
Zaldarriaga, M., Hui, L., & Tegmark, M. 2001, ApJ, 557, 519
Zel'dovich, Y. B., & Novikov, I. D. 1964, Soviet Physics Doklady, 9, 246
Zheng, W., Syphers, D., Meiksin, A., et al. 2015, ApJ, 806, 142
Zwicky, F. 1933, Helvetica Physica Acta, 6, 110

ACKNOWLEDGEMENTS

I would like to express my sincere gratitude to my adviser Joseph F. Hennawi for giving me the opportunity to join the MPIA ENIGMA group and work on the forefront of astrophysics. His continuous support of my Ph.D study and related research, his endless patience, motivation, and immense knowledge have helped me to develop necessary skills and proper attitude for science. I would also like to thank my collaborator Matthew McQuinn, without whom this project would not be possible at all. His insightful suggestions, comments, and stimulating discussions have always helped to improve my work.

I am grateful to all the past and current members of the ENIGMA group for the inspiring discussions, support and friendly working environment. It was my pleasure to work with you, folks!

I am particularly grateful to Amelia Stutz, Gabor Worseck, Frederick Davies, Sasa Tsatsi, Richard Teague and Michael Maseda, whose valuable comments on different parts of my thesis have greatly improved the quality of this work.

All these years spent in Heidelberg would be impossible to imagine without people, whom I am privileged to call friends: my 'cu-cu' gang Michael, Paolo and Sasa; Amy, Taisiya, Eduardo, Miguel, Emer, Anders, Michael, Anna-Christina, Richard, Jakob, Simon, Ben, Aiara,.. There is no way I can mention everybody, but all of you guys made these years unforgettable, for which I will always be thankful.

I would like to thank my bachelor and master supervisors Yuri A. Shchekinov and Vladimir I. Korchagin, who helped me to make my first steps in science. I am deeply thankful to Evgenii Vasiliev and Anastasia Ponomareva for always being there for me despite actually being far away.

Last but not the least, I would like to thank my family: my parents, my sister, and my wife for always supporting and believing in me.